Stony Brook University

Endoscopic Optical Coherence Tomography for Bladder Cancer Diagnosis

A Dissertation Presented by

Zhenguo Wang

to

The Graduate School

in Partial Fulfillment of the

Requirements

for the Degree of

Doctor of Philosophy

in

Biomedical Engineering

Stony Brook University

December 2007

Stony Brook University

The Graduate School

Zhenguo Wang

We, the dissertation committee for the above candidate for the

Doctor of Philosophy degree, hereby recommend

acceptance of this dissertation.

Yingtian Pan, Ph.D.
Dissertation Advisor
Associate Professor, Biomedical Engineering Department

Ki H. Chon, Ph.D.
Chairperson of Defense
Associate Professor, Biomedical Engineering Department

Emilia Entcheva , Ph.D.
Committee Member
Associate Professor, Biomedical Engineering Department

Christopher S. D. Lee, M.D.
Committee Member
Assistant Professor, Department of Urology,
Stony Brook University Hospital

This dissertation is accepted by the Graduate School

Lawrence Martin
Dean of the Graduate School

Abstract of the Dissertation

Endoscopic Optical Coherence Tomography for

Bladder Cancer Diagnosis

by

Zhenguo Wang

Doctor of Philosophy

in

Biomedical Engineering

Stony Brook University

2007

This dissertation presents the development of MEMS-based endoscopic OCT systems and the application for bladder cancer diagnosis at high resolution, noninvasively, and instantaneously. To enhance the image fidelity (e.g., SNR, dynamic range, and frame rate) critical to bladder cancer diagnosis, we proposed to utilize differential acousto-optic modulation technique (AOM) in combination with grating based rapid scanning optical delay (RSOD) to provide ultra-stable rapid axial scan of the reference mirror in time-domain OCT (TDOCT) system. In addition, we developed a spectral domain endoscopic OCT (SDOCT) system at 1.3 μm to enable higher imaging rate with improved dynamic range, and we proposed interpixel shift technique to enhance the effective field of view and dynamic range. Recent incorporation of Doppler OCT endoscopy to detect abnormal angiogenesis induced by carcinogenesis permits enhanced

differentiation between malignant lesions and benign bladder lesions. To overcome the limitation of a relatively small field of view of endoscopic OCT (e.g., <5mm laterally per scan), we proposed fluorescence image guided OCT (FG-OCT) to enhance the diagnostic efficacy in bladder. Results based on an ex vivo rat bladder carcinogenesis model showed enhanced diagnosis of bladder TCCs with sensitivity and specificity of 100% and 93%, respectively. Following successful ex vivo studies, we initiated in vivo clinical study. The experimental results based on 40 human cases have shown significantly improved diagnostic efficacy (91% sensitivity, 80% specificity) with no reported adverse effect, suggesting that OCT endoscopy is a very promising technique for bladder cancer diagnosis.

Table of Contents

List of Figures

Acknowledgements

This project would not have been possible without the support of many people. Many thanks to my adviser, Professor Yingtian Pan, who continually encouraged me to finish projects, attend conferences, and write scientific publications. I especially thank him for his patience and trust in me and the research experience I enjoyed in his group.

I am grateful for the privilege of many discussions with Professor Thomas C. Weinacht on topics of dispersion analysis and spectral domain Doppler OCT. I thank Professor Michael Hadjiargyrou for his help on cell culturing and his generous support through my graduate study. I thank Dr. Tuqiang Xie, Dr. Zilu Wu, and Dr. Bai Chen on for many insightful discussions on various topics of optics and OCT. Especially, I am indebted to Zhijia Yuan's help on software development and the fruitful discussions with him on signal-processing problems in OCT. I wish him best of luck in his project.

I would like to thank Professor Huikai Xie in University of Florida for providing MEMS mirrors. I would like to thank Professor Wayne C. Waltzer for his gracious help on our first clinical case, and many thanks to all the people in the Department of Urology and operation room who provided their kind help and support for our human study. I would also like to thank Professor Jingxuan Liu of Pathology Department for his help in reading histology slides for both ex vivo and in vivo studies.

I thank Dr. Kaustabh Ghosh for his encouragement and sharing his enthusiasm for research. I would also like to thank all the OCT group members, my friends and colleagues at the Stony Brook University for helping make my graduate life enjoyable.

I am also indebted to Professor Ki H. Chon, Emilia Entcheva, Christopher S. D. Lee and Chris Jacobson for serving on my proposal and dissertation committee and for their constructive criticism and comments on the research.

I also want to thank Journal of Urology, Optics Express, Applied Optics and Journal of Biomedical Optics for their generous permissions to include my previously published materials in this dissertation.

Lastly, I thank my family, Mom, Dad and my lovely wife Zhi Pan, for everything.

Chapter I

Introduction

Bladder cancer is among the most frequent types of malignancy and one of the leading causes of death in the United States, with estimated 67,160 new cases diagnosed and 13,750 deaths in the year of 2007[1]. Most bladder cancers are superficial carcinomas and originate in the basal cell layer of the epithelium. Thus early diagnosis is crucial for appropriate treatment and enables enhancement of the cure rate and survival of patients. Yet this still remains a clinical challenge. For instance, screening techniques such as cytology[2], fluorescence in situ hybridization[3], and BTA[4], are very sensitive for clinical detection of carcinoma in situ (CIS) and high-grade transitional cell carcinomas (TCCs); however, these techniques are much less sensitive for the early diagnosis of low-grade TCCs and unable to locate the cancerous lesions, which compromises their ultimate effectiveness. On the other hand, conventional medical imaging methods such as x-ray, CT, and MRI fail to detect early bladder malignancies because of their resolution limitation. As a result, cystoscopy remains the clinical standard for early bladder cancer detection. However, as cystoscopy is an *en face* imaging modality and only provides surface imaging without displaying any morphological details below the bladder surface, it often misses flat early bladder cancers such as CIS that may be visually normal or unspecific; thus, random biopsy is necessary for conclusive diagnosis and staging of malignancy for patients with positive

findings in urine cytology. However, this invasive procedure may still miss approximately 50% of early flat bladder cancers[5, 6]. Therefore, a noninvasive and high-resolution imaging technique would be highly desirable to improve the diagnostic sensitivity and specificity and critical to the therapeutic benefits of early bladder cancer patients.

Recent advances in optical imaging have demonstrated a number of potential modalities for early epithelial cancer detection. For instance, fluorescence cystoscopy following photosensitizer administration has significantly enhanced diagnostic sensitivity by detecting photochemical changes pertinent to TCCs[7, 8]. Another example is confocal endoscopy, which can provide subcellular imaging of the epithelium, but its penetration depth is limited to 300 μm and thus may not be suitable for staging tumors[9].

OCT, on the other hand, is a fiber-optic imaging technique that can provide high-resolution cross-sectional images of tissue morphology at a depth of 1-2 mm, which is advantageous for detection of various types of superficial lesions[10-12]. Studies from several groups have demonstrated the potential of OCT cystoscopy to diagnose various bladder diseases[11, 13] with miniaturized probes[13-15].

Since the first introduction of MEMS technology to OCT endoscopy in our group in 2001[13], it has attracted more and more attention due to its superior imaging performance, such as better lateral resolution, larger imaging range and potential faster imaging speed. However, there are several

challenges to be addressed to design a MEMS-based endoscopic OCT system suitable for *in vivo* clinical diagnosis with high-fidelity cross-sectional image.

1. For *in vivo* study, fast frame rate and high sensitivity are required to provide dependable and repeatable image quality for solid diagnosis. This has been addressed with two technological developments: high-speed TDOCT using fiberoptic acousto-optic phase modulation[16] (AOM-OCT) and recent incorporation of spectral domain OCT (SDOCT) technique into our MEMS based[17] endoscopic system. Although AOM-OCT system has been demonstrated to increase the frame rate by 4 times, the dispersion effect introduced by acoustic crystal must be correctly compensated, otherwise the axial resolution and imaging contrast will be degraded. With theoretical analysis, it is found that while group velocity dispersion can be compensated with the RSOD employed in the reference arm, higher order dispersion due to the acoustic crystal must be corrected by interting like AOM crystal in the sample arm. Additionally, dispersion compensation is of particular interest in ultrahigh resolution OCT system, when the light source employed has a much broader bandwidth and therefore is more suspectible to dispersion effect.

On the other hand, although the SDOCT system has increased the frame rate by 4~8 times with comparable dynamic range to TDOCT, it is found in our in vivo study that the SNR degrades along the depth due to limited spectral resolution. This degradation compromises the effective field of view in the axial direction and may induce artifacts to complicate diagnostic sensitivity and specificity. To tackle this problem, the pixel shift technique[18] is proposed

to increase the imaging depth and SNR of SDOCT. The results show that interpixel shifted SDOCT can not only double the depth of field of SDOCT image but also eliminate the artifacts induced by aliasing effect, thus improving image contrast in areas with large depths.

2. The efficiency of OCT examination for urinary bladder is compromised by the limited lateral field view for endoscopic OCT, since the typical human bladder size is ~10 cm, while endoscopic OCT lateral scanning range ~4 mm. Without proper surface guidance, it would take excessive time for whole bladder diagnosis. To tackle the problem of limited field of view, fluorescence image guided endoscopic OCT (FG-OCT) technique has been proposed[17] and its capability for bladder cancer diagnosis has been systematically evaluated in *ex vivo* animal study[19]. By combining the advantage of the high sensitivity of fluorescence in detecting cancer-specific biochemical changes and the high resolution of OCT in diagnosing morphological changes induced by carcinogenesis, FG-OCT has shown improved diagnostic ability with 100% sensitivity and 93% specificity.

Encouraged by the exciting ex vivo study, we have initiated our human in vivo study since 2005 to evaluate the capability of endoscopic OCT for bladder cancer diagnosis in clinical scenario. In contrast to ex vivo animal study, it is found that human cases are much more complicated. For instance, a substantial portion of malignant lesions demonstrate decreased scattering in vivo while almost all such lesions enhance scattering in our ex vivo study. On

the other hand, more features are noticed for in vivo imaging, such as ‘nest’ structures within bladder tumors.

To characterize the new features and enhance OCT diagnostic efficacy, Doppler flow measurement has been introduced into current endoscopic SDOCT. Several techniques have been developed to improve the flow measurement sensitivity which is partially attributed to the random vibration of the optical components, such as optical fibers and optical coupler. One of the most effective techniques is to minimize phase noise with armored cable to reduce optical fiber motion. Further improvements include a more sensitive Kasai velocity estimator [20] and a thicker glass window to circumvent mirror image artifacts.

In summary, the first part of this dissertation emphasizes on system development, including: Chapter II brief summary of OCT technique development and the contrast mechanism of OCT for bladder cancer diagnosis; Chapter III high-speed time domain OCT using acousto-optic modulation with dispersion compensation; and Chapter IV development of spectral-domain based OCT (SDOCT) with inter-pixel shift technique for bladder cancer diagnosis to enhance imaging field of view, imaging efficacy and imaging speed. The second part of the dissertation focuses on systematic experiments of OCT endoscopy for *ex vivo* and *in vivo* bladder cancer diagnosis, including: Chapter V systematic evaluation of FG-OCT technique for bladder cancer diagnosis in a standard rat cancer model compared with 5-ALA induced fluorescence imaging; Chapter VI design of MEMS mirror based miniaturized

endoscopic probe for *in vivo* study and evaluation its imaging capability in an animal model and human in vivo study; Chapter VII spectral domain OCT endoscopy at 1.3 μm for in vivo bladder cancer diagnosis and Chapter VIII Doppler OCT endoscopy for angiogenesis detection to enhance diagnostic specificity for bladder cancer. Last part of the dissertation (Chapter IX) is the summary and future work of OCT endoscopy for bladder cancer diagnosis.

Chapter II

Optical Coherence Tomography

Optical coherence tomography (OCT) operates in a similar way to ultrasound imaging. An ultrasound B-mode image is reconstructed by sequentially acquiring time-gated ultrasonic echoes whereas OCT detects coherence-gated backscattered light. Because of its high axial resolution (1~20μm) and intermediate penetration depth (1~2mm in tissue), OCT has been

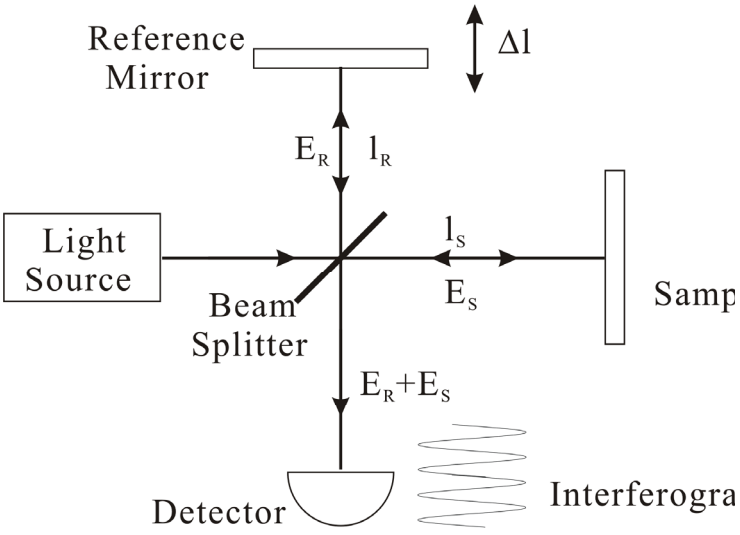

Fig.2. 1 Schematic diagram of OCT based on a Michelson interferometer.

becoming an enabling noninvasive imaging technique since it was first introduced in 1991[21].

2.1 Low coherence interferometry

The core technology of OCT is based on low coherence interferometry to detect the depth-dependent profile of reflectivity. As shown schematically in

Fig.2.1, Michelson interferometer is most commonly employed in the OCT development. The light from the laser source is divided by a beam splitter into the reference arm and the sample arm. The reflected light beams from these two arms are recombined in the detection arm and detected by a photodiode.

In case of monochromatic light illumination, the light fields in the reference and sample arms can be mathematically expressed as[22],

$$E_R(t) = A_R \exp\{-i[2kl_R - \omega t]\}$$
$$E_S(t) = A_S \exp\{-i[2kl_S - \omega t]\} \quad (2.1)$$

where A, ω, *and* k are the amplitude, angular frequency and wave number of light, respectively. $2l_R$ and $2l_S$ are the round-trip pathlengths in the reference and sample arms. Then the interference signal is derived as,

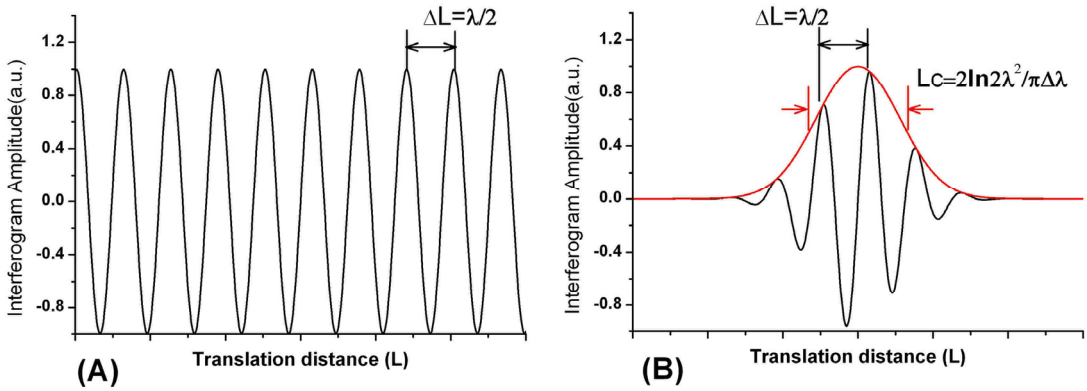

Fig.2. 2 Two simulated Interferograms under A) monochromic illumination and B) broadband illumination. L_C is the coherence length that defines the axial resolution of coherence-domain reflectometry upon which OCT is based.

$$I = I_R + I_S + 2\sqrt{I_R I_S}\cos[2k\Delta L] \quad (2.2)$$

where I_R=<A_R*A_R>, I_S=<A_S*A_S> are the intensities ($< f(x) >= \lim_{T\to\infty} \frac{1}{2T}\int_{-T}^{T} f(x)dt$)

and ΔL=l_R-l_S. If the pathlength difference ΔL is changed, e.g., by translating the

reference mirror axially, an interferogram (A scan) is generated as shown in Fig.2.2, which is a sinusoid signal with ΔL.

In case of low-coherence interference under broadband light illumination, the electrical fields can be approximated as quasi-monochromatic for mathematical simplicity and Eq.(2.1) can be rewritten as

$$\begin{aligned} E_R(\omega,t) &= A_R(\omega)\exp\{-i[2k_R(\omega)l_R-\omega t]\} \\ E_S(\omega,t) &= A_S(\omega)\exp\{-i[2k_S(\omega)l_S-\omega t]\} \end{aligned} \tag{2.3}$$

This gives the interference signal as,

$$I = I_S + I_R + 2\sqrt{I_R I_S}\,\mathrm{Re}\left[\frac{1}{2\pi}\int_{-\infty}^{\infty} S(\omega)e^{-i\Delta\varphi(\omega)}d\omega\right] \tag{2.4}$$

where $I_R=\langle\int A^*_R(\omega)A_R(\omega)d\omega\rangle$ and $I_S=\langle\int A^*_S(\omega)A_S(\omega)d\omega\rangle$ are the intensities in the reference and sample arms. $S_{cs}(\omega)=A^*_R(\omega)A_S(\omega)/\sqrt{I_R I_S}$ is spectral cross correlation function and $\Delta\varphi(\omega)=k_R(\omega)l_R-k_S(\omega)l_S$ is the phase difference. If we assume no spectral alternation in the sample and reference arms, then $S_{cs}(\omega)$ is equivalent to the source power spectrum $S(\omega)$. The phase term in Eq.(2.4) is rather complicated and can be approximated by Taylor expansion as,

$$\Delta\varphi(\omega) = k(\omega_0)\Delta L + k'(\omega_0)(\omega-\omega_0)\Delta L + \frac{k''(\omega_0)}{2}(\omega-\omega_0)^2\Delta L + \frac{k'''(\omega_0)}{6}(\omega-\omega_0)^3\Delta L + \ldots \tag{2.5}$$

where first four terms are phase delay, group delay, group-delay dispersion (GDD) and third order dispersion (TOD), respectively. In a dispersion-free system,

$k^{(n)}(\omega_0) = \partial^n \Delta\varphi(\omega) / \partial\omega^n \,|_{\omega=\omega_0} = 0$ for $n \geq 2$. By applying Eq.(2.5), Eq.(2.4) can be simplified as[22],

$$I = I_R + I_S + 2\sqrt{I_R I_S}\,\mathrm{Re}\left[\frac{e^{-i\omega_0 \Delta L/\upsilon_p}}{2\pi}\int_{-\infty}^{\infty} S(\Delta\omega) e^{-i\Delta\omega\Delta L/\upsilon_g} d\Delta\omega\right] \tag{2.6}$$

where $\upsilon_p = \omega_0/k(\omega_0$, $\upsilon_g = 1/k'(\omega_0)$ are the phase and group velocities respectively. Assume that the laser source has a Gaussian power spectrum,

$$S(\omega - \omega_0) = \left(\frac{4\sqrt{\pi \ln 2}}{\delta\omega}\right)^2 \exp\left[-\frac{4\ln 2(\omega - \omega_0)^2}{\delta\omega^2}\right] \tag{2.7}$$

where $\delta\omega$ is the full-width-half-maximum (FWHM) bandwidth. Then Eq.(2.6) gives,

$$\mathrm{I} = I_R + I_S + 2\sqrt{I_R I_S} e^{\left(-\frac{4\ln 2 \Delta L^2}{\upsilon_g^2 t_C^{\,2}}\right)} \cos[k_0 \Delta L] \tag{2.8}$$

where $t_C = 8\ln 2/\delta\omega$ is the FWHM pulse width. In free space, $\upsilon_g = c$, the corresponding round-trip FWHM pathlength difference, termed as the coherence length, is given as,

$$L_C = \frac{\upsilon_g t_C}{2} = \frac{4c\ln 2}{\delta\omega} = \frac{2\ln 2 \lambda_0^{\,2}}{\pi\Delta\lambda} \approx 0.44\frac{\lambda_0^{\,2}}{\Delta\lambda} \tag{2.9}$$

where λ_0 is the central wavelength and $\Delta\lambda$ is the FWHM spectral bandwidth. Apparently, L_C defines the ultimate axial resolution of OCT.

As shown in Fig.2.2 are the simulation results of the inteferograms of ideal coherence (e.g., from a coherent laser) in panel A) and low coherence (e.g., white-light source) in panel B), respectively. A comparison between curve A) and curve B) clearly indicates that low coherence reflectrometry upon which OCT is based provides pathlength-dependent reflectivity at a resolution close to the coherence length L_C. According to Eq.(2.9), L_C decreases with the

increase of $\Delta\lambda$. For instance, for a superluminescent diode (SLD) with λ_0=*1320nm* and $\Delta\lambda$=78nm, the measured coherence length in Fig.2.3 is approximately equal to the theoretical result of L_C=9.8μm using Eq.(2.9). In other words, ultrahigh resolution OCT (uOCT) can be achieved by employing an ultra-broadband laser. For example, an OCT system using a femtosecond laser with λ_0=*800nm* and $\Delta\lambda$=140nm can result in a coherence length of $L_C \approx$2.0μm. Such a high axial resolution may facilitate sub-cellular imaging of biological tissue noninvasively.

2.2 Dispersion effect

Theoretically, higher axial resolution OCT imaging can be achieved by using a broader band laser source. However, uOCT (L_C=1~2.0μm) remains a technical challenge because of dispersion effect induced by either material dispersion, or modal or polarization dispersions in the single mode fiber that

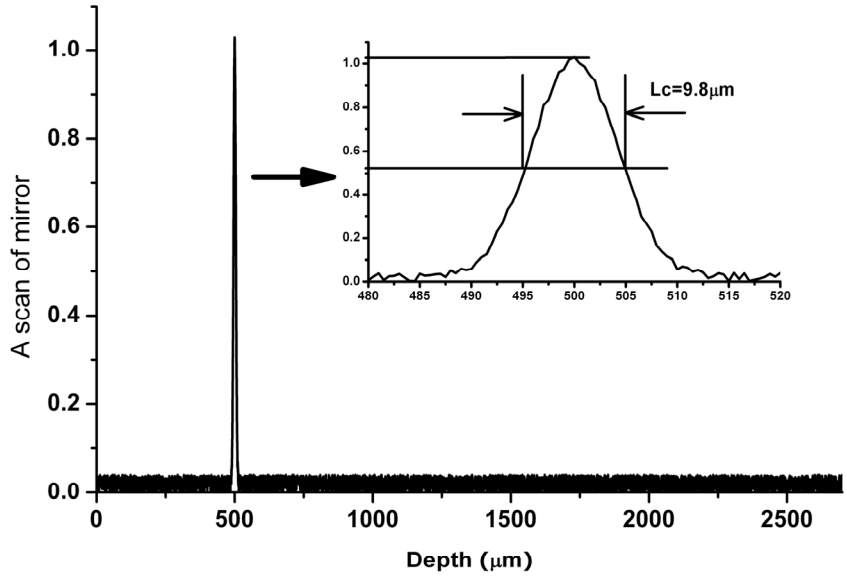

Fig.2. 3 A scan from mirror. Inset in upper panel shows the amplified mirror pulse.

may substantially broaden the apparent coherence length L_C' ($L_C'>L_C$). Obviously, L_C is L_C' under the transform limit, i.e., when dispersion is fully compensated.

Dispersion refers to an optical phenomenon that a wave is separated into spectral components with different frequency due to the dependence of the wave's speed on its frequency, which can be induced by propagation through an optical medium whose index of refraction is wavelength dependent, i.e., $n=n(\lambda)$. To demonstrate the influence of GVD (2nd order dispersion) on L_C' of OCT imaging, we assume that the laser source has a Gaussian power spectral density as given by Eq.(2.7) and the TOD and higher order dispersions in Eq.(2.5) are ignored, the corresponding phase difference in Eq.(2.5) can be rewritten as,

$$\Delta\varphi(\omega) = k(\omega_0)\Delta L + k'(\omega_0)(\omega-\omega_0)\Delta L + \frac{k''(\omega_0)}{2}(\omega-\omega_0)^2\Delta L \qquad (2.10)$$

The resultant L_c' can be derived based on Eq.(2.8) and Eq.(2.9) as [22],

$$L_C' = L_C\sqrt{1+\left(\frac{L_D}{L_C}\right)^4} \qquad (2.11)$$

where $L_D = c\sqrt{k''(\omega_0)\Delta L}$. Here ΔL refers to the pathlength of unmatched dispersive material between sample and reference arms. It is clearly indicated in Eq.(2.11) that L_C' can be severely broadened than L_C if $L_D >> L_C$. Therefore dispersion compensation is crucial in ultrahigh resolution OCT to maintain the high axial resolution, i.e., $L_C'=L_C$. However, it must be noted that the broadening induced by GVD (linear dispersion) can be fully compensated with

an optical delay (e.g., RSOD) as will be discussed in section 3. Material dispersion usually involves TOD and higher-order dispersion, which is very difficult to compensate and thus still remains a major technical challenge in uOCT instrumentation.

2.3 Optical delay line and frame rate of OCT

In time-domain OCT (TDOCT), the axial scan of reference mirror determines the image size in the axial direction and the frame rate of 2D cross-sectional OCT imaging. It is obvious that increasing the axial scan rate will proportionally increase the frame rate of 2D OCT imaging. Yet, it is less obvious to know that to maintain constant-velocity axial scan is crucial to OCT image quality (e.g. SNR, dynamic range). Assume that the reference mirror is translated at a line speed of υ, then, $\Delta L=l_R-l_S=(l_{R0}-l_S)+\upsilon t$, where the initial pathlength difference $(l_{R0}-l_S)$ is a constant and can be set to zero for simplicity. Applying it to Eq.(2.8) gives:

$$\mathrm{I} = I_R + I_S + 2\sqrt{I_R I_S}\, e^{\left(-\frac{4\ln 2\, t^2}{\tau^2}\right)} \cos[2\pi f_0 t] \qquad (2.12)$$

where $f_0=k_0\upsilon/2\pi=\upsilon/\lambda_0$ is carrier frequency (i.e., Doppler frequency shift) and $\Delta f=1/\tau=\upsilon\delta\omega/8\upsilon_g ln2\approx\upsilon\Delta\lambda/\lambda_0^2$ is the bandwidth of the envelop. The detected interferometric signal is modulated at f_0, and the function of signal processing in TDOCT is amplitude demodulation to recover the depth-dependent reflectivity (i.e., envelop). Because the detected backscattering signal from biological tissue is very weak (e.g., $\leq 10^{-4}$), signal processing such as bandpass filtering centered at $f=f_0$ is required to eliminate background noise (e.g., shot

noise) beyond the bandwidth. Therefore, a stable-velocity axial scan (u) is critical to permit a narrow bandpass filtering ($f_0 \pm \Delta f$) to achieve high SNR in OCT imaging. Because mechanical scan is involved, high-speed and constant-speed axial scan has remained a major challenge in the development of high-speed and high-fidelity TDOCT.

A number of optical delay lines have been proposed for high-speed OCT[22-25]. Each technique has its advantages and drawbacks. For instance, linear translators are very slow (<30 Hz); spinning cube can rotate up to a few 10 kHz, but the duty cycle is less than 70%; fiberoptic PZT stretcher can go up to a few kHz, but suffer from scanning nonlinearity and dynamic birefringence in the single mode fiber coil. Spinning disk mirror array is an intriguing approach that allows high speed (>10kHz) linear scan with >90% duty cycle, but the resultant Doppler shift at high speed is too high to achieve high dynamic range.

The recently introduced Fourier domain rapid scanning optical delay (RSOD) line[26] has revolutionized the axial scanning technique to permit high speed TDOCT. Its unique advantages include high repetition rate up to 1-2 kHz, sufficient scanning range (>3mm) and most importantly, independent control over group and phase delays. Detailed discussions on RSOD for high speed TDOCT will be presented in section 3, including our innovative work using acousto-optical modulation (AOM).

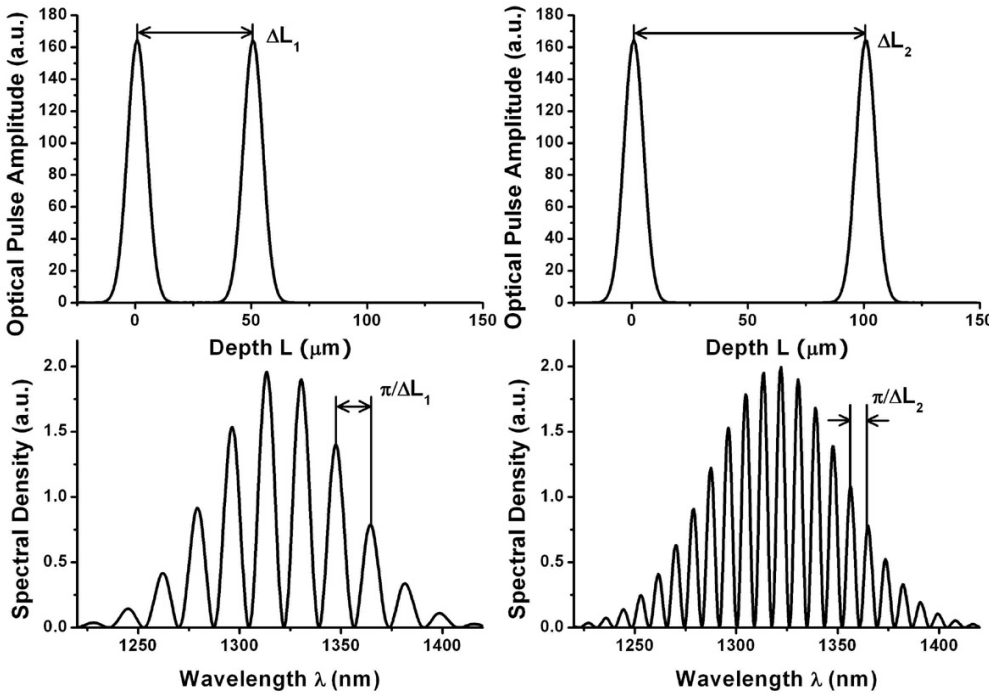

Fig.2. 4 Simulated A scan spectrum for SDOCT. Spectra resulted from distance of 50um (left) and 100um (right) are presented.

2.4 Spectral domain OCT (SDOCT)

SDOCT is based on the principle of spectral radar to detect pathlength dependent reflectivity, i.e., A-scan[27]. This is implemented by replacing the photodiode in Fig.2.1 with a 1D spectral imager to detect the spectral distribution *I(k)* including spectral interference modulation. Eq.(2.4) can be rewritten as

$$I = I_S(k) + I_R(k) + 2\sqrt{R_R R_S}\,S(k)\cos(2k\Delta L) \tag{2.13}$$

where $I_S(k)=R_S S(k)$, $I_R(k)=R_R S(k)$. R_S, R_R are the coupling ratios in the sample and reference arms ($R_S+R_R=100\%$). Assume $R_S=R_R=50\%$, Eq.(2.13) can be simplified as,

$$I = S(k) + S(k)\cos(2k\Delta L) \tag{2.14}$$

The first term *S(k)* is the 'DC' background, i.e., source power spectrum; the 2nd term contributes to the spectral interference modulation with period of $\delta k=\pi/\Delta L$ (see bottom panels) or frequency of $\delta k^{-1}=\Delta L/\pi$. In other words, the spectral graph is modulated by the pathlength difference and the modulation frequency δk^{-1} increases with ΔL. For instance, the simulation results in Fig.2.4 clearly show the difference in modulation frequency of the spectral graphs between $\Delta L=50\mu m$ (left) and $100\mu m$ (right). Because of the relation shown in Eq.(2.14), the measured spectral interference graph *I(k)* can be converted to the pathlength domain *I(ΔL)* (i.e., A-scan) by an inverse Fourier transform *iFFT[S(k)].*

According to the Fourier transform theorem, the spectral bandwidth Δk (e.g., $\Delta\lambda=-(2\pi/k^2)\Delta k$) of $S(k)$ determines the coherence length L_C *in* the $I(\Delta L)$ domain, and the spectral modulation frequency δk^{-1} determines ΔL, as shown in Fig.2.4. This implies that the field of view of SDOCT in the axial direction ΔL_m is eventually limited by the spectral resolution δk_m of the spectral radar. Applying Nyquist sampling theorem to the Fourier pair δk and $\cdot 2\Delta L$ (i.e., $\delta k \cdot 2\Delta L=2\pi$) gives,

$$\Delta L_m = \frac{\pi}{2\delta k_m} = \frac{\lambda_0^{\,2}}{4\delta\lambda_m} \tag{2.15}$$

For example, $\Delta L_m \approx 4.4mm$ (in free space) for a 1320nm SDOCT system that uses spectral radar with spectral resolution of $\delta\lambda_m$=0.1nm according to Eq.(2.15).

Fig.2.5 shows an experimental example of SDOCT to illustrate the FFT relation between spectral domain and pathlength domain (i.e., A-scan) for a pathlength difference of $\Delta L \approx 250\mu m$ between sample and reference mirrors.

The reconstructed central curve (with L_C=*9.8μm*) corresponds to the background power spectrum *S(k)* and the side peak at *ΔL≈247μm* (L_c*'=10μm*) corresponds to the spectral interference term. A mirror curve at *ΔL≈-247μm* is introduced due to phase ambiguity in *iFFT*. A minor broadening *Δ*=L_c*'-* L_c*=0.2μm* is likely induced by uncompensated dispersion between the arms according to Eq.(2.11).

SDOCT can drastically improve SNR and imaging rate to permit real-time 3D OCT, however, drawbacks of this technique include image contrast degradation with depth and mirror image that limits axial FOV. SNR degradation is caused by limited spectral resolution that diminishes the

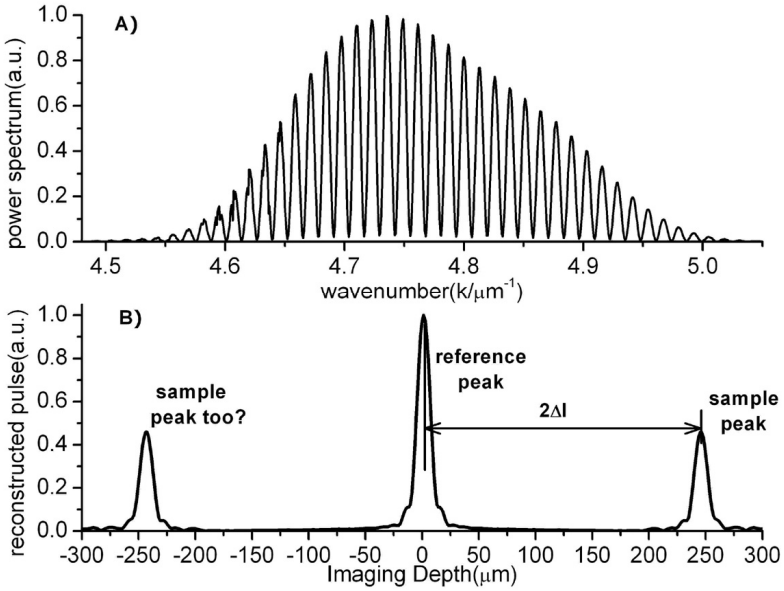

Fig.2. 5 A-scan reconstruction for SDOCT. Upper: experimental spectrum; bottom: reconstructed interferogram with inverse Fourier transform.

spectral modulation depth for higher frequency components that contribute to the image contrast at deeper region. Mirror image is resulted from phase ambiguity, because FFT of Eq.(2.14) only preserves the amplitude term. Thus,

additional spectral detection has to be performed to restore the imagery term *S(k)sin(2kΔL)* to eliminate mirror image.

On the other hand, SNR degradation is caused by the convolution effect of the finite size of the camera pixel. The final digitized spectrum is the 'true' spectrum convoluted with an averaging window determined by the pixel size. The higher frequency signals (resulted from deeper positions) are more susceptible and diminish more quickly, causing degraded SNR. Detailed discussions are presented in section 4.

2.5 OCT resolution mechanism and image contrast

The axial resolution Δz of OCT—either TDOCT or SDOCT—is defined by the coherence length L_C (under transform limit), as given by Eq.(2.9) in free space. In biological tissue with refractive index of n, $\Delta z = L_C/n$.

As a laser scanning optical imaging technique, the lateral resolution Δr of OCT is determined by the focusing spot size in the sample arm, which is given as[28],

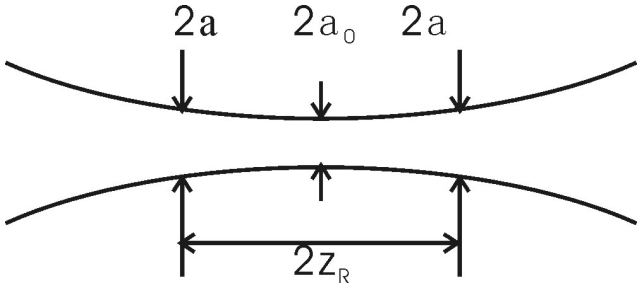

Fig.2. 6 Gaussian beam propagation. a_0 is the focused beam waist, z_R is the Rayleigh range.

$$\Delta r = a_0 = \frac{2\lambda f}{\pi\phi} = \frac{\lambda}{\pi NA} \tag{2.16}$$

where *f* is the focal length of the objective lens, ϕ is the beam size of the incident light exiting the fiberoptic collimator, and $NA = \phi / 2f$ is numerical aperture. The Rayleigh range z_R, that defines the depth at which the focal spot expands to $a = \sqrt{2}a_0$ on either side, is given as,

$$2z_R = \frac{2\pi a_0^{\,2}}{\lambda} = \frac{\pi \Delta x^2}{2\lambda} = \frac{2\lambda}{\pi N.A.^2} \tag{2.17}$$

Unlike microscopy, the axial resolution of OCT is solely determined by the source bandwidth. Therefore, high-resolution imaging can be achieved without using a high NA objective, which makes OCT uniquely attractive to *in vivo* biological imaging. However, the lateral resolution is affected by NA;

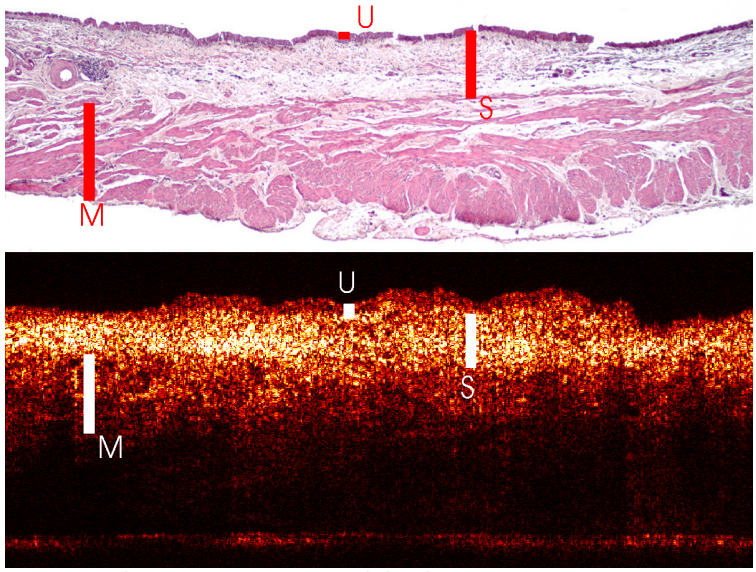

Fig.2. 7 Contrast mechanism for HE staining and OCT for rat bladder. In upper panel, cells are stained with hematoxylin followed by a counter stain of red eosin so that the nuclei stain a deep blue-black and the cytoplasm stains pink. Bottom panel is the OCT image at the same position. By comparison, three basic layers of the bladder are clearly delineated: U: urothelium, S: submucosa, M: muscularis layer.

higher NA is required for improved resolution which will in turn compromise the field of depth unless focus tracking has to be implemented such as in optical coherence microscopy (OCM).

Interpretation of OCT contrast mechanism has remained the major challenge in OCT study. Conventional histopathology uses H&E staining to enhance the contrast in visualizing cellular and morphological details of biological tissue; whereas OCT uses tissue backscattering as natural 'biomarker' to identify and characterize different types of tissue and their alternations (e.g., carcinogenesis). Fig.2.7 shows an example to compare the

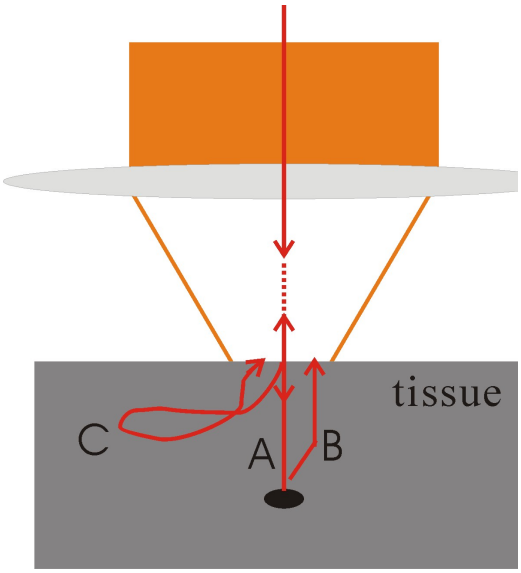

Fig.2. 8 Light interaction with tissue. A and B: least-back-scattering; C: multiple scattering.

corresponding 2D cross sectional OCT image and histology (with a 4X objective) of a normal rat bladder wall. Both images can delineate bladder morphology, e.g., urothelium (U), lamina propria (S), and muscularis (M). Histology provides superior image contrast details to OCT; however, OCT is

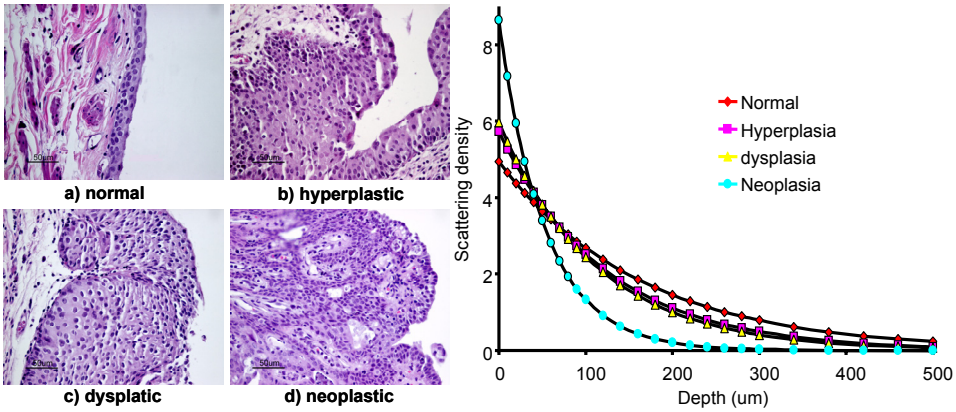

Fig.2. 9 Theoretical analysis for OCT signal for bladder cancer lesions at different stages. Left panel: histology images; Right panel: simulated scattering density. [12]

noninvasive that does not require tissue dissection, fixation, and chemical dye staining. The result demonstrates the unique advantages and potential of OCT a promising candidate for optical biopsy to image biological tissue microstructures noninvasively, in vivo, in real time, and at high resolution.

However, because of complex light tissue interactions, OCT suffers from a major problem caused by multiple scattering. As shown in Fig.2.8, in a turbid media such as biological tissue, the backscattered light detected by OCT can be divided into two categories[29]: 1) least-backscattered light which undergoes only very few scattering whose pathlength $L_s \approx 2d_z$ (d_z refers to depth), and 2) multiple scattering light with $L_s > 2d_z$. Least-backscattered light contributes to OCT image contrast, whereas multiple scattering induces coherent noise and degrades OCT image contrast and reduce resolution.

For instance, multiple scattered light C from a shallower region in Fig.2.8 will be included as noise into the least-backscattered light A or B from a deeper place as long as their pathlengths are equal. As a consequence, the effective OCT imaging depth is limited to a certain range beyond which

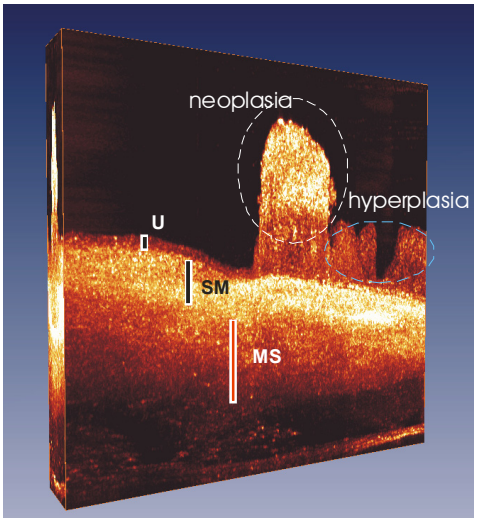

Fig.2.10 Experimental OCT images of bladder cancer lesions at different stages.

multiple scattering dominates and thus destroys the image contrast. It has been known that for biological tissue, this range is limited to ~1-2 mm depending on the type of tissue. Despite this limitation on imaging depth, OCT has found wide applications such as in ophthalmology to diagnose retinal disease and in diagnoses of various epithelial cancers originated from the superficial layers.

2.6 Contrast mechanism for OCT diagnosis of bladder cancer

As most bladder cancers originate within the basal cell layer of the urothelium, therefore, optical modeling of urothelium is critical to the contrast mechanism of OCT diagnosis of the bladder cancers. This was studied in our lab by performing histomorphometry of bladder specimens including normal bladder, benign lesions and bladder cancers at different grades to simulate the optical properties of these lesions and the resultant OCT contrast changes [12].

In this modeling study, it was assumed that nuclei were the primary scattering contributors of urothelial scattering and all the other components within cells were negligible. Then the bladder urothelium tissue was simplified as a uniform matrix of 3D nuclei with size and density acquired from histomorphometric measurements, and the scattering properties were calculated according Mie's theory of scattering. The simulation results are summarized in Fig.2.9 together with the histological images for different types of rat bladder lesions, which predict a major enhancement (~40%) in urothelial backscattering or OCT signal level in cancerous urothelium. The results suggest that by imaging of bladder morphology, urothelial thickening, and backscattering enhancement, OCT can differentiate normal bladder, LP inflammation, hyperplasia (benign bladder lesion), and TCC.

The diagnostic criteria are exemplified by the experimental results in Fig.2.10 which shows 3D OCT of a rat bladder following induction of MNU, a rat bladder carcinogen. Morphological details are clearly delineated, including normal urothelium (U), hyperplasic lesions (thickened U but without major increase in backscattering), and a neoplastic lesion or TCC with >70% increase in backscattering[12]. It must be noted that analysis of OCT image contrast for cancer diagnosis in scattering biological tissue is extremely complex. Changes can be cause by cell type, geometry (thickness, surface topography), absorption (H_2O, blood), scattering (scarring and calcification can drastically alter scattering), and tissue homogeneity (e.g, honey-nest like change in papillary TCCs).

Chapter III

High-speed time domain optical coherence tomography using acousto-optic modulation for bladder imaging

High imaging performance with optimized axial resolution, imaging contrast and imaging rate is of great importance for bladder imaging and reliable bladder cancer diagnosis *in vivo*. For a time domain optical coherence tomography (TDOCT) system, the imaging performance is mainly determined by the optical delay line employed in the reference arm, which has been attracted considerable research interest, as discussed in Chapter II.

Among various optical delay designs, diffraction grating based rapid scanning optical delay line (RSOD) has been widely used to achieve high-speed linear axial scan and independent control of the phase and group delay rates[26, 30]. Although it has been reported to provide linear scanning range of 3 mm at up to 2 kHz, the imaging fidelity is compromised at high imaging rate because the relatively low phase velocity results in incomplete demodulation of the interferograms. With dispersion compensation for acoustic crystals, incorporation of acousto-optic (AO) modulation into RSOD has been reported to improve the performance of high-speed reference scan[16, 31, 32] and OCT image fidelity.

This chapter discusses the detailed theoretical analysis for diffraction grating based RSOD and theoretical analyses to characterize the dispersion in the acousto-optic modulation (AOM)-mediated OCT system. Experimental results are also presented to demonstrate the ability to eliminate group dispersion and

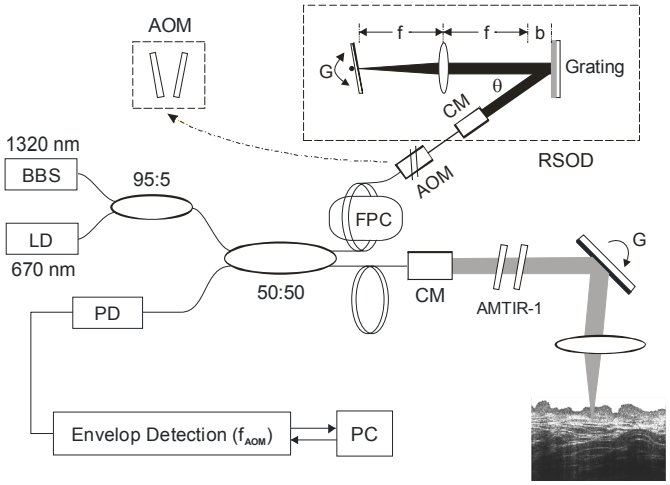

Fig.3. 1 A sketch of an OCT imaging system using an acousto-optic modulator (AOM). A fiberoptic AOM is inserted in the reference arm to provide a stable f_{AOM}=2MHz (tunable) frequency modulation. In combination with a RSOD, it allows for rapid reference scanning for fast and high-fidelity OCT imaging. BBS: broadband source; LD: aiming laser; PD: photo diode; CM: fiberoptic collimator, G: servo scanner. A pair of AO crystals is included in the sample arm for dispersion compensation.

enhance axial resolution to transform limit (i.e., source L_C) by adding like AOM crystals in the sample arm of the OCT system. The results show that the AOM-based OCT system can provide high-fidelity bladder tissue images at an A-scan rate of 4 kHz by using a simple resonant scanner. This part of study has been published in Applied Optics in 2005[33]; the discussion that follows is drawn from the content of that paper.

3.1 Experimental Setup

The schematic of our high-speed AOM-based OCT system with dispersion compensation is shown in Fig.3.1, which is based on a fiber-optic Michelson interferometer. A broadband light source (BBS) was used to illuminate the interferometer whose pigtailed output power is 13mW. The central wavelength λ_0 and FWHM spectral bandwidth $\Delta\lambda$ of BBS are 1320nm and 78nm, respectively,

thus the corresponding coherence length L_C is 9.8 μm. The light from the source was split equally into the reference (R) and the sample (S) arms of the fiberoptic Michelson interferometer and recombined in the detection fiber (B).

In the reference arm, a grating-lens-based rapid-scanning optical delay is used to vary the optical pathlength, i.e., to provide axial scan. As has been reported previously[16, 34, 35], this technique allows separation of the phase and the group delays, permitting an independent control over Doppler frequency shift f_D and bandwidth Δf of the OCT signal. To provide a stable and appropriately elevated Doppler frequency shift f_D over Δf for high-performance OCT imaging, a fiberoptic AOM is inserted into the reference arm prior to RSOD.

The optical frequency of light passing through the AOM will be modulated from ν_0 to $\nu_0 \pm f_{AOM}$ according to Bragg diffraction theory, where f_{AOM} is the frequency of the modulating signal applied to the AOM crystal and frequency upshift (+) or downshift (-) depends on the propagation angel between the light wave and the acoustic wave. In this AOM device, two AMTIR1 crystals are configured with one upshifted to f_{AOM1}=56MHz and one downshifted to f_{AOM2}=55MHz to frequency modulate the light to $f_{AOM}=2(f_{AOM1}- f_{AOM2})$= 2MHz for heterodyne detection.

3.2 Diffraction grating based rapid scanning optical delay line (RSOD)

The RSOD consists of a grating-lens pair configuration (Fig.3.2). It operates based on shift property of Fourier transform: a phase ramp introduced in frequency domain by the rotary mirror can produce a group delay in time domain[36].

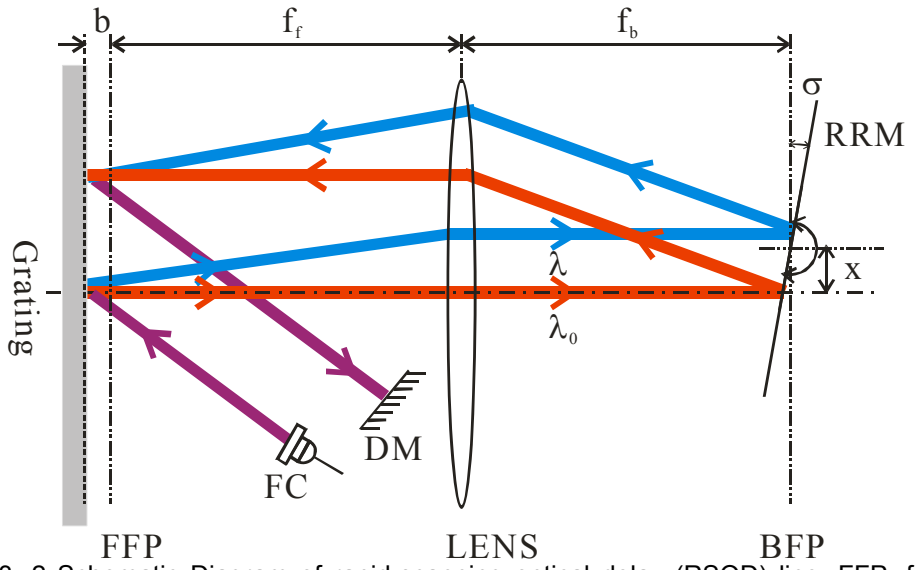

Fig.3. 2 Schematic Diagram of rapid-scanning optical delay (RSOD) line. FFP: front focal plane; FC: fiber collimator; DM: double pass reflection mirror; BFP: back focal plane; x: rotary reference mirror offset from optical axis; RRM: rotary reference mirror; f_f: front focal length; f_b: back focal length; b: grating offset from front focal plane.

For the optical setup shown in Fig.3.2, the phase delay (Δl_ϕ) and group delay (Δl_g) are calculated as[36],

$$\begin{aligned} \Delta l_\phi &= 4x\sigma \\ \Delta l_g &= 4x\sigma - \frac{4\sigma(l_f + b)\lambda_0}{p} \end{aligned} \tag{3.1}$$

where the p is the pitch of the grating, σ and x are the servo mirror rotation angle and offset from the optical axis respectively, l_f is the front focal length, b is the grating offset from front focal plane and λ_0 is the central wavelength. For typical configuration with $\sigma = 4^\circ$, $x = 2mm$, $l_f = 80mm$, $p = 1/400mm^{-1}$, $b = 0\ mm$ and $\lambda_0 = 1.32\mu m$,

$$\frac{4\sigma(l_f + b)\lambda_0}{4\sigma xp} = \frac{(l_f + b)\lambda_0}{xp} = \frac{80 \times 1.32 \times 10^{-3}}{2 \times 1/400} = 20.8 >> 1 \tag{3.2}$$

Therefore group delay (Δl_g) can be simplified as,

$$\Delta l_g = -\frac{4\sigma l_f' \lambda_0}{p} \tag{3.3}$$

where $l_f'=l_f+b$. Combined with Eq.(2.12), the carrier frequency and signal bandwidth are,

$$\begin{aligned} f_0 &= 4x\omega_m / \lambda_0 \\ \Delta f &= -4l_f' \omega_m \Delta\lambda / p\lambda_0 \end{aligned} \tag{3.4}$$

where $\omega_m = d\sigma / dt$ is the angular frequency of the mirror. Therefore, the quality factor for following electronics signal processing is,

$$\frac{f_0}{\Delta f} = \frac{px}{-l_f' \Delta\lambda} = \frac{4\sigma_{\max} x\lambda_0}{(\Delta l_g)_{\max} \Delta\lambda} \tag{3.5}$$

Based on Eq.(3.5), the quality factor is determined by the light source, the scanning range $(\Delta l_g)_{max}$ and the rotation amplitude σ_{max} and offset x from the optical axis of the reference mirror. The scanning range $(\Delta l_g)_{max}$ for bladder imaging is ~3mm at σ_{max}~5˚ limited by mechanical stability. With certain light source (e.g., λ_0=1320nm, $\Delta\lambda$=78nm), it requires x as large as possible to have a decent SNR and demodulation, which in turn requires larger (and thus heavier) mirror to accommodate a certain spectral bandwidth and would result in lower scanning frequency due to larger inertia. Therefore, the system SNR will be compromised when RSOD is used for high speed OCT imaging.

A fiberoptic AOM is inserted into the reference arm to provide a stable and appropriately enhanced Doppler frequency shift f_D for high performance OCT imaging in combination with RSOD[16]. The custom-made AOM consists of two AO modulators in series, which are for upshift and downshift respectively. The adjustable roundtrip beat frequency is $f_{AOM}=2(f_{AOM1}-f_{AOM2})$. Thus, with the insertion

of AOM the effective Doppler frequency f_D of the detected interferometric signal becomes,

$$f_D = 4x\omega / \lambda_0 + f_{AOM} \tag{3.6}$$

To achieve best stability and scanning speed, x should be set to 0 and therefore $f_D=f_{AOM}$. Because direct frequency modulation (f_{AOM}) is implemented in the reference arm of a fiberoptic interferometer[29] by using a pair of differential AO modulators (e.g., one upshifted to 56MHz and one downshifted to 55MHz)[31], this technique allows for generation of an ultra-stable interference fringe carrier frequency ($\Delta f_{AOM} \leq 0.1\%$) for real-time OCT imaging. More importantly, f_{AOM} can be easily tuned to a proper frequency range, e.g., 2MHz compared to the group delay (e.g., bandwidth) so that the optically heterodyned OCT signal can be completely demodulated at an enhanced signal-to-noise ratio. As no pivot offset ($x=0$) is needed to induce phase shift, the servo mirror size can be reduced to decrease mechanic inertia and thus to increase OCT frame rate. Also because of direct frequency modulation, a resonant servo mirror can be used for group delay without changing the carrier frequency. This offers a great potential to drastically improve OCT and DOCT frame rate without compromising the signal-to-noise performance.

However, in the AOM-mediated OCT system, group dispersions were resulted not only from unmatched optical fiber leads between the sample and the reference arms but also from the insertion of the AOM device (AMTIR-1 crystals) in the reference arm, resulting in group delay dispersion (GVD), third-order dispersion (TOD) and higher-order dispersions. Dispersion compensation can be

implemented by shifting the grating off the focal plane in RSOD, which has been used to balance the dispersion mismatch between the reference and the sample arms of the fiberoptic interferometer to achieve the highest possible fringe visibility and axial resolution in OCT. Although the previous study showed promising results[16], attempts to completely compensate the dispersions by only moving the grating in RSOD were unsuccessful possibly because of high-order dispersions.

3.3 Dispersion Compensation

In this OCT system, almost all optical components may induce dispersion, which includes focusing lens, collimators, unmatched SM fiber leads between sample and reference arms, diffraction grating, and AOM crystals. However, our analysis below reveals that the contribution of most of these components to dispersion is negligible except the major dispersive components such as the AOM device, the grating and the unmatched fiber leads. For a non AOM-based OCT system, it has been found that the 2nd-order dispersion or group-velocity dispersion (GVD) induced by mismatched fiber leads can be compensated by shifting the grating along the back focal plane in the RSOD[37]. The group dispersion GVD_G produced by RSOD (grating) can be analyzed by Treacy grating pair as[38]

$$GVD_G = \frac{b\lambda}{cd^2[1-(\lambda/d-\sin\theta)^2]^{3/2}} \tag{3.7}$$

where b is the grating displacement from the focal plane (dispersion-free position) as shown in Fig.3.1, λ, c are the wavelength and speed of light, respectively; d is

grating constant. $\theta=\theta_i$ is the incident angle to the normal of grating (θ_d=0). According to grating equation ($\sin\theta = \lambda/d$), Eq.(3.14) can be simplified as

$$GVD_G = \frac{b\lambda}{cd^2} \tag{3.8}$$

Eq.(3.8) indicates that GVD_G can be linearly adjusted by shifting the axial position b of the grating in RSOD so that the total GVD induced in the OCT system, as will be discussed below, can be compensated. It must be noted that because θ_d=0, the 3rd-order dispersion induced by the grating $TOD_G << GVD_G$ and is thus neglected.

With the inclusion of AOM, dispersion can be caused by both material dispersion and acousto-optic interaction. As shown in Fig.3.1, the paired AO crystals under acoustic fields are analogous to a pair of diffraction gratings; therefore, the dispersion induced by AO interaction can be analyzed as Treacy grating pair, which is given as

$$GVD_{AO} = (\frac{4\pi c f_{AOM}^2}{V^2\omega^3} - \frac{\alpha f_{AOM}}{\omega^2 V})D \tag{3.9}$$

where f_{AOM} ($f_{AOM}\approx f_{AOM1}\approx f_{AOM2}$) is the ultrasonic frequency. V is the ultrasonic speed, ω is the angular frequency of light, α is the Bragg angle, and D is the thickness of the AO crystals. Compared with Eq.(3.8), the equivalent grating constant in Eq.(3.9) can be written as $d'=\Lambda/2=V/2F$ (Λ is ultrasonic wavelength) and thus Eq.(3.9) can be approximated as $GVD_{AO} = (\frac{\pi c}{d'^2\omega^3} - \frac{\alpha}{2\omega^2 d'})D$. For our AOM-based OCT setup, d'^{-1}=44lines/mm, D= 10mm, and d^{-1}=400lines/mm,

GVD_{AO} is negligible and can be easily compensated by slightly shifting the grating in RSOD (b≈0.1mm).

On the other hand, material induced group dispersion must be taken into account and is mainly contributed by the mismatched optical fiber and the AOM crystals, which can be calculated by the dispersion equation,

$$GVD_M = \frac{\partial^2 \phi}{d\omega^2} = \frac{\partial}{\partial \omega}(L / v_g) \tag{3.10}$$

where ϕ is the phase difference, L is material path length, and v_g is group velocity,

$$v_g = \frac{c}{(n - \lambda \frac{dn}{d\lambda})} \tag{3.11}$$

Furthermore, the relationship between the refractive index and wavelength, $n(\lambda)$, can be given by Sellmeicer equation as,

$$n^2(\lambda) = 1 + \sum_{i=1}^{3} \frac{B_i \lambda^2}{\lambda^2 - C_i} \tag{3.12}$$

where B_i and C_i are Sellmeicer coefficients which can be determined by experiments. According to Eq.(3.8), the material GVD_M induced in the OCT system can be compensated by adjusting b in the RSOD, and from Eq.(3.10) we can predict b, i.e., how far the grating in the RSOD needs to be shifted for the best compensation of the GVD_M induced by AOM and unmatched optical fiber leads between the sample and the reference arms.

It must be noted that only the 2nd–order dispersion is considered in Eq.(3.12), which has been found sufficient for many OCT applications. However, with the increase of bandwidth (e.g., uOCT) and the use of highly dispersive components (e.g., AOM), the complex TOD and higher-order dispersions can no

longer be neglected and must be compensated. In general, the phase shift $\phi(\omega)$ of a broadband light can be represented by a Taylor series as

$$\phi(\omega) = \phi(\omega_0) + \phi'(\omega_0)d\omega + \phi''(\omega_0)\frac{(d\omega)^2}{2!} + \phi'''(\omega_0)\frac{(d\omega)^3}{3!} + \cdots\cdots \qquad (3.13)$$

where $\phi(\omega_0)$ is the phase delay, $\phi'(\omega_0)$ is the group delay, $\phi''(\omega_0)$ is the group delay dispersion GVD which is given in Eqs.(3.7-9), and $\phi'''(\omega_0)$ is the third-order dispersion (TOD). Thus, the broadening of L_C induced by total dispersion in the time domain can be given by the inverse Fourier transform,

$$I(t) = F^{-1}\left[I_i(\omega)e^{i\phi(\omega)}\right] \qquad (3.14)$$

where I(t) and $I_i(\omega)$ represent the spectral distribution of the output and incident light propagation through dispersive materials, e.g., AOM and mismatched fibers in the OCT system. In Eq.(3.21), I(t) and $I_i(\omega)$ can be measured, and the phase term $\phi(\omega)$ is given by Eq.(3.13). In the calculation, $\phi''(\omega_0)=GVD_M$ and $TOD_M=\phi'''(\omega_0)=\partial^2(L/v_g)/\partial\omega^2$ can be calculated by applying Eqs.(3.10-12) with measured dispersion data $n(\lambda)$ for both fused silica and AMTIR-1, thus allowing us to analyze the influence of the material dispersion induced by each components on L_C broadening and to determine the optimal compensation by the grating shift b in RSOD and other techniques. Experiments were performed on the OCT setup as illustrated in Fig.3.1, in which the effects of dispersion compensation on the axial resolution of OCT were evaluated by measuring the transient I(t) (both shape and the width of the autocorrelation function) as the grating position b was proceeded and other components such as fused silica and AMTIR-1 plates were inserted. The autocorrelation function was measured in

broadband condition, i.e., the interferometric signal was detected by a broadband (10MHz) trans-impedance preamplifier, processed by a band-pass filter (2MHz ± 200KHz) and linearly demodulated with an output bandwidth of Δf=400kHz to avoid potential broadening induced by signal-to-noise enhancement. This was confirmed by the fact that further increasing Δf did not affect the OCT signal transient and the measured L_C. The optimum positions of b_{opt} and the measured L_C for the setups without AOM and with AOM inserted in the reference arm and with one or paired matching AMTIR-1 plates placed in the sample arm were recorded and compared with the results of theoretical analyses.

3.4 Resonant Scanning

In addition to dispersion compensation to improve axial resolution, a resonant servo mirror was used to replace the linear servo mirror in the RSOD to increase OCT imaging rate. Unlike previous report[2] in which the carrier (Doppler) frequency f_D of OCT signal varied with the angular position of the resonant mirror and therefore required a broader Δf for envelop demodulation (Fig.3.3) resulting in a reduced SNR, the carrier frequency f_{AOM} is independent of resonant scanning; therefore Δf broadening is avoided, which offers the potential for AOM-based OCT to achieve high-speed imaging (e.g., 4kHz A-scan) without compromise of reducing SNR. However, nonlinear imaging processing is required to correct image distortion induced by nonlinear A-scan of the resonant servo mirror. This was performed by rearranging each A-scan dataset using Spline interpolation

$$I_i(4f\lambda\omega\cos\omega t/d) \rightarrow I_i(4f\lambda\omega/d) \tag{3.15}$$

where i=1,…,1000 and ω is the angular frequency of the resonant (linear) servo mirror. Although Eq.(3.15) can reduce nonlinear distortion, it was anticipated that the useful duty cycle for OCT imaging would be reduced by using a resonant scanner.

3.5 Results

For the AMTIR-1 crystals used in the AOM device, the dispersion function $n(\lambda)$ can be acquired by fitting Eq.(3.12) to the experimental data. Although shifting grating b may also produce TOD_G and higher-order dispersions to compensate those induced by other optical components in the systems, because $TOD_G << GVD_G$ in our current RSOD setup ($\theta_d=0$), both theoretical modeling and experiments revealed that it was unable to independently control TOD_G and GVD_G and failed to fully compensate material dispersions induced by a dispersive element with a high TOD_M such as AMTIR-1. However, the theoretical model based on Eq.(3.7)-Eq.(3.14) permitted evaluation of the grating shift b_{opt} for optimal GVD_M compensation and analyses of the influence of unmatched TOD_M on L_C broadening. The following four cases were analyzed: 1) the system dispersion induced by mismatched fiber leads and compensation to determine the baseline b_0 for grating shift; 2) the varied system dispersion induced by the inclusion of AOM in the reference arm and the optimal compensation with grating shift b_1; 3) the varied system dispersion induced by adding 1 AOM crystal in the sample arm and the optimal compensation with grating shift b_2; and 4) the varied system dispersion induced by adding paired AOM crystals in the sample arm and the optimal compensation with grating shift b_3, i.e., b_{opt}. In all 4 cases, the cross-

correlation function I(t) was measured while b was shifted until the lowest L_C was reached at which the measured grating shift b was compared with that of the corresponding theoretical prediction.

Fig.3.3 shows the results of theoretical modeling in which BBS was assumed to have a quasi-Gaussian spectral distribution with λ_0=1320nm and $\Delta\lambda$=78nm. The results indicate that their coherence lengths (i.e., FWHM bandwidth of the cross-correlation functions) are L_C*=15.39μm, 13.02μm and 9.72μm, corresponding to 0, 1 and 2 AMTIR-1 crystals inserted into the sample arm of the fiberoptic interferometer. The theoretical source coherence length is L_C=9.8μm. It was found that as GVD induced by the mismatched fiber leads is negligible at 1.3μm with a grating shift of b_0<0.5mm. As shown in Fig.3.4(A), the asymmetry of the cross-correlation function is noticeable with a right shoulder over 15% peak value because shifting grating b only compensates GVD according to Eq.(3.8) and therefore cannot completely compensate TOD and higher-order dispersions induced by AOM. The calculated grating shift of $b_{opt/0}$=11.73mm is substantial. In the case that 1 AMTIR-1 crystal was inserted into the sample arm to compensate 50% thickness of the AOM crystals in the reference arm, the grating shift is decreased to $b_{opt/1}$= 5.9mm and the right shoulder in the cross-correlation function is reduced to less than 5% as shown Fig.3.3(B). When both AMTIR-1 crystals are inserted in the sample arm to fully compensate the AOM crystals in the reference arm, Fig.3.3(C) shows that the asymmetric effect of the cross-correlation is eliminated and the grating shift is restored to $b_{opt/2}$=b_0=0.5mm.

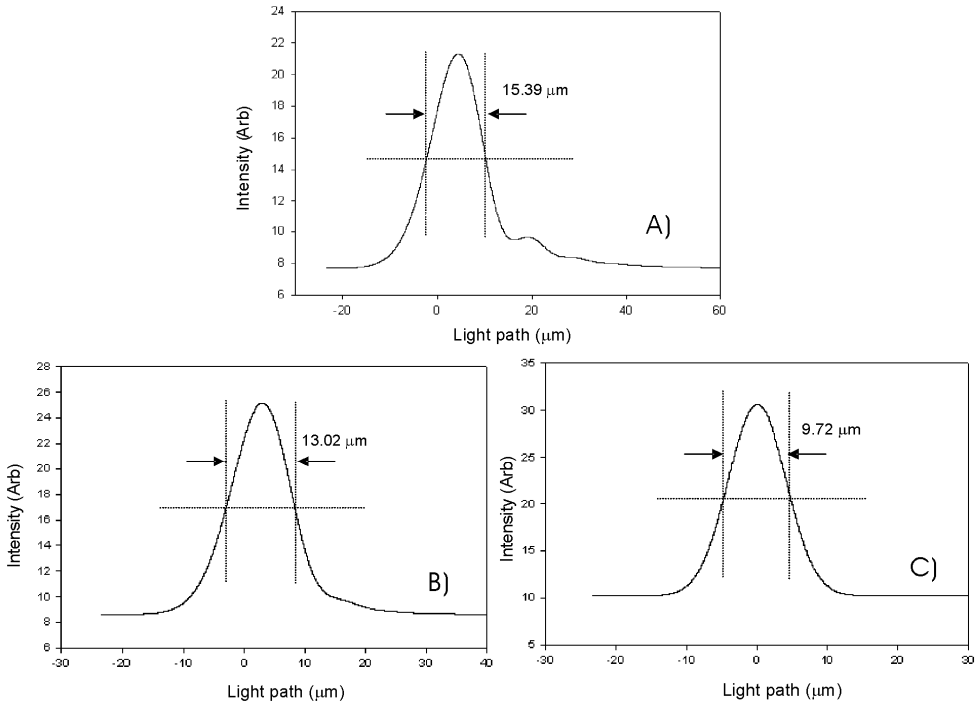

Fig.3. 3 Theoretical autocorrelations after dispersion compensation for OCT system with AOM in the reference arm: Grating shift b to compensate 0 (A), 1 (B) and 2 (C) AMTIR-1 crystals placed in the sample arm. BBS: λ_c=1320 nm, $\Delta\lambda$=78 nm.

To verify the theoretical analyses, measurements were performed on the experimental setup shown in Fig. 3.1 with respect to the configurations that 0, 1 and 2 AMTIR-1 crystals were inserted into the sample arm of the fiber-optic Michelson interferometer. In the experiments, a microscopic cover glass slide was used for cross-correlation measurement. The measured grating shifts for dispersion compensation in these three configurations were $b_{m/0}$=12.15mm, $b_{m/1}$=6.32mm, and $b_{m/2}$=0.54mm, respectively. These results correlate well with the corresponding theoretical analyses. The measured cross-correlation functions shown in Fig.3.4 are in fair agreement with the theoretical analyses shown in Fig.3.3. Due to incomplete compensation of TOD and higher-order AMTIR1 dispersion, a right shoulder is observed in Fig.3.4(A) and the curve is broadened to LC*=15.44μm, leading to reduced axial resolution even at optimal

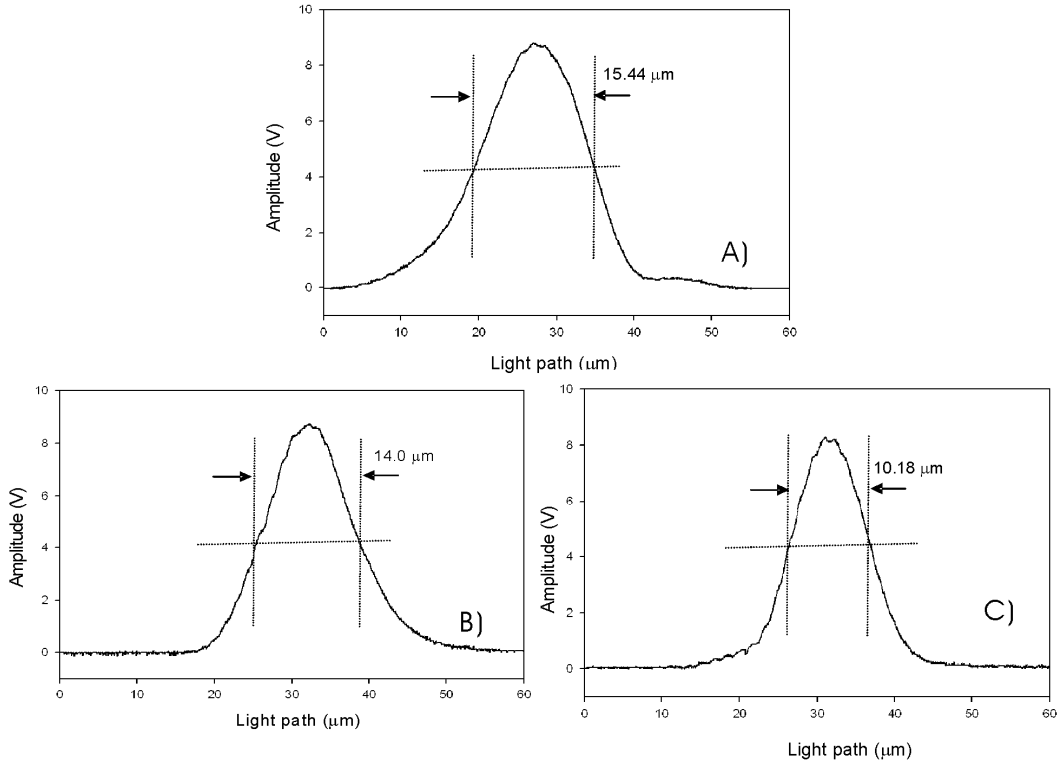

Fig.3. 4 Measured cross-correlation functions after dispersion compensation for AOM-based OCT system: grating shift b to compensate 0 (A), 1 (B), and 2 (C) AMTIR-1 crystals placed in the sample arm.

grating compensation. The amplitude of the measured shoulder (<10%) is slightly smaller than the theoretical prediction.

In Fig.3.4(B), the reduced right shoulder is not as clear as that in the theoretical curve although the elevation is visible. Small ripples are visible over the cross-correlation curve, which was induced by linear demodulation and increased with Δf. The measured coherence length is LC*=14μm. When 2 AMTIR-1 crystals were included in the sample arm to fully compensate the dispersion including the high-order dispersions of the AOM device, the cross-correlation curve in Fig.3.4(C) becomes symmetric and narrow. The measured grating shift was reduced to bm/2=b0=0.54mm and the coherence length was

minimized to LC*=10.18μm, which is slightly higher than the theoretical result of 9.72μm and source LC=9.8μm. The result confirms the theoretical analysis that GVDAO induced by AO interaction is negligible, thus the dispersion of the AOM device including TOD and higher-order dispersions which cannot be compensated by grating shift in the RSOD (mainly compensating GVD only) can be fully compensated by adding like AO crystals in the sample arm.

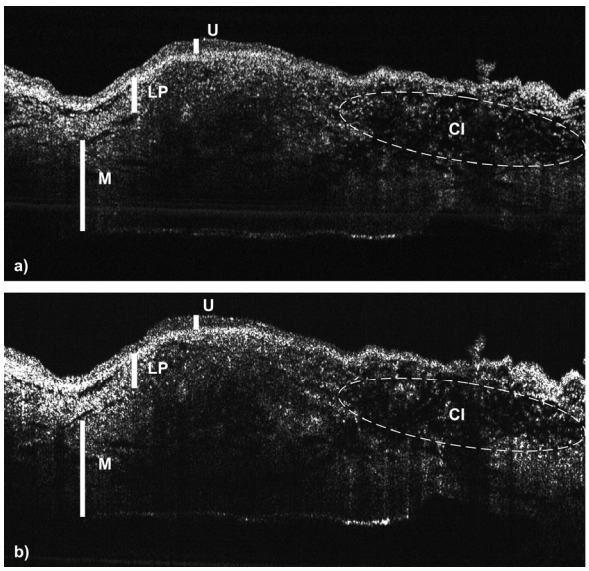

Fig.3. 5 2D OCT images of a porcine bladder imaged by OCT system with regular RSOD (a) and with AOM-mediated RSOD (b). Image size: 2mm lateral × 6mm vertical. U: urothelium, LP: lamina propria; M: muscularis, CI: area in LP with cystitis and denuded urothelium. Because of inflammation, the bladder morphology was less clear than that of a normal porcine bladder.

One of the major advantages of AOM-mediated OCT technique is that because the group and phase delays are decoupled and phase delay is provided by ultra-stable AOM, the need for high-speed linear scan, e.g., a servo mirror driven by a triangular waveform to generate stable Doppler frequency shift for optical heterodyne detection, is circumvented. Thus, high-speed resonant depth or group delay can be implemented without compromising detection SNR. To demonstrate the advantage, experiments were performed on the OCT system

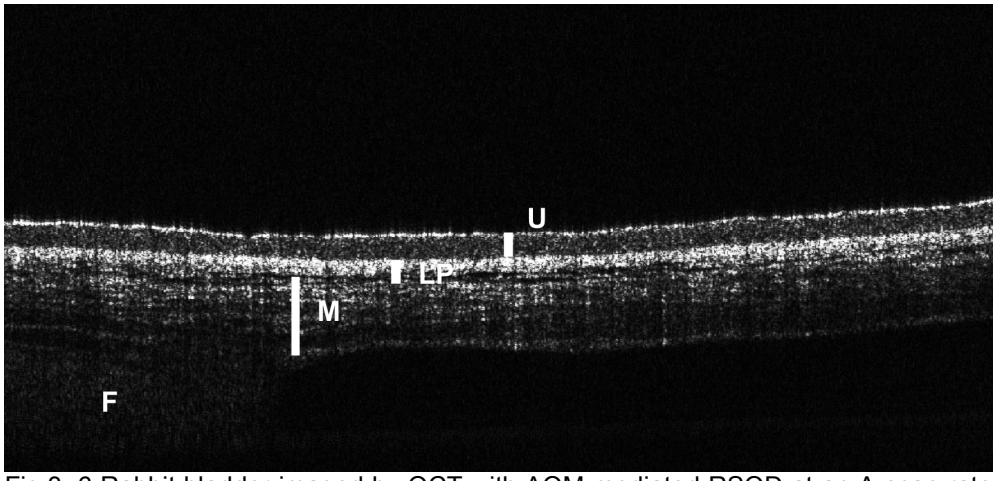

Fig.3. 6 Rabbit bladder imaged by OCT with AOM-mediated RSOD at an A-scan rate of 4 kHz. U: urothelium, LP: lamina propria, M: muscularis, F: attached fatty tissue. The 2D-OCT image size is 2×6 mm^2 displayed in pseudo color (linear demodulation). Signal level ranged from -40dB (bright) to -100dB (dark).

with regular RSOD and with AOM-mediated RSOD for high-speed depth scanning. In the experiments, the identical section on a porcine bladder with cystitis was imaged.

Fig.3.5 shows the results imaged with a servo mirror in the RSOD driven by a modified triangle waveform (i.e., broadband linear scan) and a resonant (i.e., sinusoidal) waveform at 500Hz, respectively. Except a slight decrease of the axial size in Fig.3.5(b), the results are fairly comparable, supporting our design strategy that AOM-mediated OCT permits resonant depth scanning without compromising the detection SNR. The micro morphology of the porcine bladder such as the urothelium (U), the lamina propria (LP), the muscularis (M), and the area with cystitis can be clearly delineated owing to their different backscattering signatures and patterns in both images[12, 17].

To further demonstrate the advantage of the AOM-mediated RSOD for higher-speed OCT, a 2 kHz resonant galvo mirror was used to provide 4kHz A-scans. The scanning mirror was carefully centered to null pivot offset so that only group delay was provided. The interference signal which was ultra-stably Doppler shifted at f_{AOM}=2MHz by the AOM could be completely demodulated at a high SNR regardless of nonlinear resonant group delay. The demodulated OCT signal sequence (A-scan) was digitized by a 12-bit 5MHz A/D and processed by a nonlinear correction according to Eq.(3.15) to minimize distortion in the axial direction induced by the resonant scanning. An example of high-speed OCT is shown in Fig.3.6 which was imaged in near real time, e.g., 8-16 fps depending on lateral pixel numbers. The morphological details of the rabbit bladder, e.g., U, SM and M, are clearly delineated although the SNR is slightly reduced due to increased frame rate which required increased system bandwidth Δf. Therefore, early cancerous changes in the bladder can be detected in real-time at up to 8-16 fps based on their morphological alternations, e.g., urothelial thickening and backscattering increase based on our previous studies[12].

3.6 Discussion

In an OCT system, dispersion balance between reference and sample arms in the interferometer is necessary to achieve the highest possible axial resolution, i.e., transform limited axial resolution of the light source L_C. To increase axial resolution requires a larger source bandwidth, and the direct result is that the dispersion increases as the source bandwidth increases if not properly compensated. As the result, it broadens the cross-correlation function as well as

asymmetry and reduces the axial resolution. In conventional OCT with RSOD for reference scan, dispersion comes from mismatched fiber leads between sample and reference arms, the lenses, the grating, and the sample medium.

The diffraction grating in RSOD can be used to compensate dispersion by shifting the grating off the front focal plane b[37] and has been used in many OCT systems. However, the grating shift b mainly compensates for GVD and can hardly independently compensate for TOD and higher-order dispersions such as those induced in high-speed AOM-mediated OCT system. It must also be noted that to compensate for high-dispersive materials such as AMTIR-1 used in AOM, a large grating shift b off the focal plane is needed which may lead to unwanted beam deviation and dispersion variation and degrade the fidelity of OCT image. Both theoretical and experimental results in Fig.3.3 and Fig.3.4 demonstrate that the coherence length L_C* of the cross-correlation function broadened 50% if TOD and higher-order dispersions were ignored although GVD was compensated by the grating shaft b in AOM-mediated RSOD. It was found that when 1 AMTIR-1 crystal which has identical dispersion characteristics with those used in AOM was inserted into sample arm to partially balance TOD or higher-order dispersions, the broadening of L_C* was drastically reduced to around 10%. However, when 2 AMTIR1 crystals were inserted into sample arm to completely balance the dispersion produced by AOM in the reference arm, both GVD and higher-order dispersions were completely balanced and thus the highest possible axial resolution with L_C*=10.18μm was measured. The measured value is only slightly higher than our model prediction of L_C*=9.7 μm and theoretical limit of

L_C=9.72μm, suggesting that highly dispersive material dispersions such as those induced by AOM, which cannot be compensated by grating in RSOD only can be completely compensated by combining grating shift in the reference arm and adding like components in the sample arm. The minor difference between theoretical and experimental results might be caused by experimental errors or dispersions of other optical components such as lenses and collimators which were ignored. Although the AOM in the reference arm is active, the two inactive AMTIR-1 crystals in the sample arm can fully compensate the dispersion based on our theoretical analysis in Eq.(3.9) and experimental results in Fig.3.4.

All the theoretical analyses and experimental studies were conducted based on our current BBS specs (λ_0=1310nm, $\Delta\lambda$=78nm). As a matter of fact, dispersion compensation will be critical and more challenging in uOCT when $\Delta\lambda$ increases. Because of the obvious advantages of AOM-mediated RSOD to ease the difficulty in fast reference scan by allowing using a resonant scanner without compromising system SNR in high-speed time-domain OCT, it is definitely

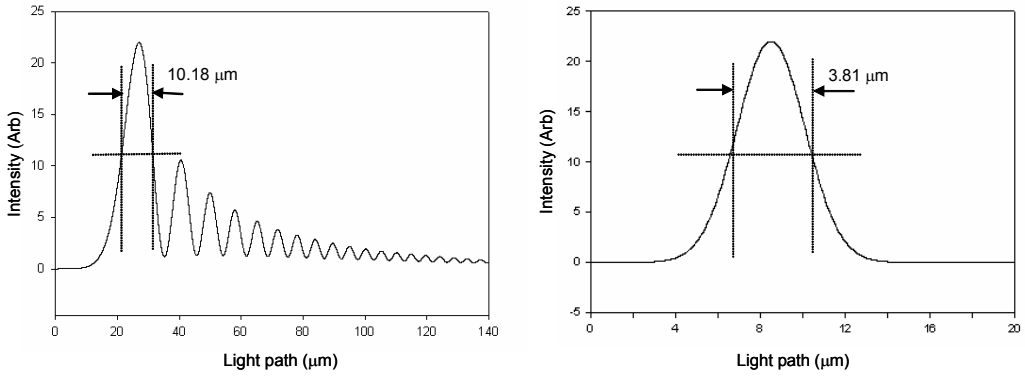

Fig.3. 7 Results of theoretical modeling of cross-correlation function of ultra broadband OCT using AOM-mediated RSOD for high-speed imaging after dispersion compensation: grating shift to compensate 0 (A) and 2 (B) AMTIR-2 crystals in the sample arm. Light source: λ_c=1320 nm, $\Delta\lambda$=200 nm.

interesting to examine the utility and limitation of this technique in real-time uOCT. To investigate the importance, the same AOM-mediated OCT system was modeled but using a broader band light source with λ_0=1310nm and $\Delta\lambda$=200nm. Fig.3.7 shows the results of theoretical modeling. The results indicate that their coherence lengths are L_C*=10.18μm and 3.81 μm, corresponding to 0 and 2 AMTIR-1 crystals inserted into the sample arm of the fiberoptic interferometer. Again, GVD and TOD and higher-order dispersions are completely compensated in Fig.3.7(B) whereas severe oscillating effect induced by TOD and high-order dispersions cannot be compensated by shifting the grating in RSOD alone as shown in Fig.3.7(A). L_C*=3.81μm in Fig.3.7(B) is very close to the theoretical source coherence length of L_C=3.78μm. However, the cross-correlation function in Fig.3.7(A) suffers from severe asymmetry with a secondary oscillating shoulder over 45% of peak value and more than 3 times broadening. These results demonstrate the importance of higher-order dispersion compensation for a broader band OCT system to achieve ultrahigh-resolution OCT imaging.

During the experiments, it was found that the OCT images, e.g., Fig.3.7, obtained by AOM-mediated OCT system with a 2kHz resonant scanner showed slightly reduced resolution contrast and larger speckles than those acquired with a 500Hz resonant scanner even after nonlinear image processing using Eq.(3.15). It might be possibly caused by inaccuracy servo scanner at high speed, insufficient sampling rate in areas away from the center of each A-scan, and increased Δf at higher scanning speed.

3.7 Conclusions

In summary, we report a new method to analyze and compensate the group dispersion in a high-speed optical coherence tomography with an acousto-optic modulator and improve the axial resolution. The results of theoretical modeling and experiments reveal that the high-order group dispersion induced by the AO crystals (AMTIR-1) largely broadens the coherence length (L_C*) and thus degrades the axial resolution of OCT and the image fidelity. The theoretical modeling methods can be used to analyze the dispersion of AOM device as well as both time-domain and frequency-domain OCT systems. Therefore, we can effectively compensate the GVD and TOD and other higher-order dispersions in the OCT system. According to our experimental results, the dispersion can be substantially compensated to less than 50% L_C broadening by RSOD in the reference arm and can be eliminated by inserting like AO crystals in the sample arm of the AOM-mediated OCT system. These results demonstrate that AOM-mediated OCT system permits high-performance OCT imaging at an A-scan rate up to 4kHz using a resonant scanner without compromising system SNR. Test images of bladder tissue show that the OCT system can clearly delineate the micro morphology, thus demonstrating the potential of this new technique to detect early bladder cancers in real time. We also anticipate that because of its ultra-stable direct frequency modulation, this AOM-mediated OCT system can potentially improve the performance of real-time Doppler OCT techniques.

Chapter IV

Spectral domain OCT for bladder imaging with interpixel shift technique

As discussed in Chapter II, recent advances in the development of spectral-domain OCT (SDOCT) has dramatically improved the dynamic range and imaging rate of OCT techniques[39, 40], taking advantage of parallel detection and signal processing of spectral radar. Compared with conventional time-domain OCT (TDOCT), the need for high-speed mechanical axial scan in reference arm is circumvented, thus enabling up to 100-fold imaging speed enhancement and near real-time 3-D imaging[41-44] of living biological tissue. Recent interesting work include removal of 'complex conjugate ambiguity'[45-48] to enhance signal to noise ratio and echo-free imaging range, Doppler FDOCT to image blood flow[35, 49] in real-time, ultrahigh-resolution SDOCT[50, 51] for 2D and 3D retinal imaging, polarization sensitive SDOCT[52, 53] and spectral second harmonic generation[54] OCT to provide more specific image contrast of biological tissue. In addition to technological advances, clinical applications of SDOCT have been performed on various types of tissue such as eye[41], esophagus[55] and urinary bladder[56], showing drastic improvement on image fidelity and imaging rate.

Despite substantive technological advances in SDOCT, some technical issues remain to be addressed for future clinical uses. For instance, the degradation in signal to noise ratio (SNR) along the depth due to limited spectral resolution compromises the effective field of view in the axial direction and may

induce artifacts (e.g., decay of OCT image contrast) to complicate diagnostic sensitivity and specificity. It was found in our *in vivo* clinical study of bladder cancer diagnosis that because of SNR degradation with depth, SDOCT diagnosis was more prone to distance change between scope and bladder surface or bladder surface asperities than TDOCT diagnosis.

To tackle this problem, we proposed to apply the pixel shift technique to increase the imaging depth and SNR of SDOCT. Pixel shift is widely used in advanced digital cameras to improve spatial resolution and image contrast. Because of limited pixel numbers (e.g., 512- or 1024- pixels) of current InGaAs diode arrays, this technique can be of great interest to enhance pixel resolution and image fidelity of SDOCT in the 1.3um wavelength range, in particular, ultrahigh-resolution SCOCT.

I will describe the system design and experimental setup for interpixel shifted SDOCT at 1320nm, and present results that demonstrate the potential of interpixel shifted SDOCT to enhance system SNR and to visualize image features beyond the depth of field of conventional SDOCT with no pixel shift. This part of study has been published in Optics Express in 2006[18]; the discussion that follows is drawn from the content of that paper.

4.1 Experimental setup

Fig.4.1 depicts the schematic diagram of the SDOCT setup. The fiberoptic interferometer is illuminated by a high power broadband source (BBS) with pigtailed output power of 13mW, central wavelength at λ_0=1320nm and full-width-half-maximum spectral bandwidth $\Delta\lambda_{FWHM}$=78nm (yielding a coherence length of

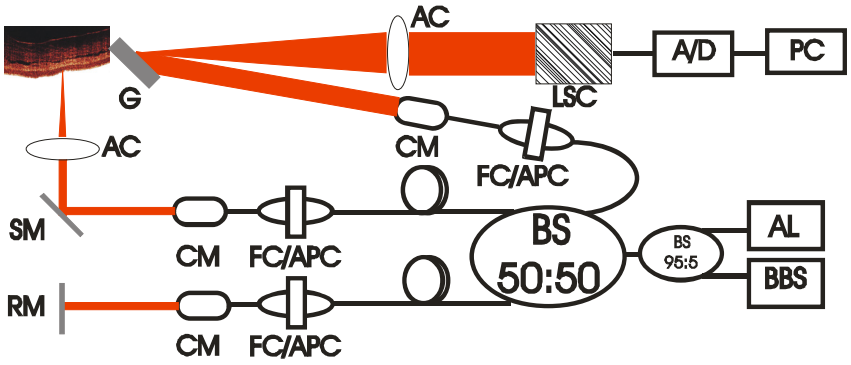

Fig.4. 1 Experimental setup for Spectral-domain optical coherence tomography (SDOCT) BBS: broadband light source; AL: aiming laser; BS: beam splitter; FC/APC: angled polished fiber connector; CM: collimator; RM: reference mirror; SM: sample scanning mirror; AC: achromatic lens; LSC: line scan camera; G: grating; A/D: analog to digital converter; PC: personal computer.

$L_C \approx 10\mu m$). The 1320nm light from BBS is equally divided in the fiberoptic interferometer, and the red light from a 670nm light from aiming laser is coupled in the source fiber via a 95%:5% coupler for visual guidance. In the reference arm, instead of a grating-lens-based optical delay line for axial scanning in TDOCT, a stationary mirror is used to match the optical pathlengths between the sample and the reference arms of the fiberoptic interferometer.

The sample arm is connected to a bench-top stereoscope in which light exiting the fiber is collimated to ϕ4.2mm, scanned laterally by a servo mirror, and focused by an f=40mm achromatic lens onto biological tissue under examination. The sample arm can also be connected to a MEMS-based endoscopic OCT catheter for *in vivo* imaging study. The light beams returning from the sample and reference arms are recombined in the detection fiber and connected to a spectral radar in which light is collimated by a fiberoptic achromatic lens collimator (CM, f=55mm), diffracted by a holographic grating(G, d=1200mm^{-1}) and focused by an achromatic lens (AC, f=120mm) onto a line InGaAs photodiode array line scan

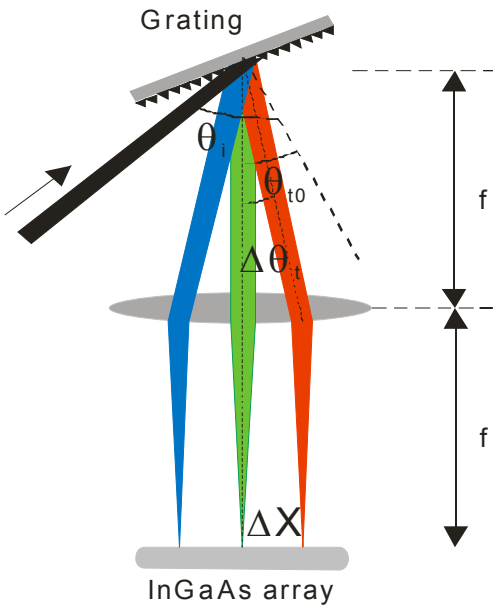

Fig.4. 2 Line scan camera based spectrometer.

camera (LSC, Sensors Unlimited, NJ) mounted on a small PZT-actuated stage for interpixel shift or stepping in the lateral direction.

The detected spectral graph, including spectrally encoded interference fringes from different depth within the biological sample, is digitized and streamlined to hard disk of a personal computer (Precision 670, Dell) via a multi-channel 12bit data acquisition board (DAQ6111E, NI) at 5MHz to permit 2D imaging at nearly 8fps. Simultaneous image processing and display is updated at 4 fps due to complex FFT computation. Stepping of line InGaAs array and the lateral servo mirror in the sample arm for 2D imaging is triggered following detection of each spectral graph (i.e. A-scan). Based on the above parameters used in our SDOCT setup, the axial resolution, i.e., $L_c \approx 10\mu m$, the lateral resolution is ~12μm, and the system dynamic range is ~110dB at 8fps. For pixel shifted SDOCT, stepping the bulky camera is currently limited to 10ms per step.

4.2 System design for spectral domain OCT

The fast line scan camera based spectrometer employed in the detection arm determines the imaging depth and the frame speed. Therefore, the spectrometer design is critical for SDOCT and worthy being discussed in details. The spectrometer employed in our system is based on diffraction grating, and can be analyzed by grating equation,

$$d^{-1}(\sin\theta_i + \sin\theta_t) = m\lambda \tag{4.1}$$

where d is pitch of the grating, θ_i, θ_t are incident and refractive angles, respectively. In practice, several factors should be taken into consideration:

1. Although in principle $\Delta\theta = \theta_i - \theta_t$ should be as small as possible to fulfill Littrow condition for best diffraction efficiency, $\Delta\theta$ has to be 25^0 or higher to achieve optical components accessibility in optical alignment. In current design, we adopt $\Delta\theta_t = 26^0$;
2. Refracted central beam θ_{t0} with $\lambda = \lambda_0$ should be the optical axis of the detection system to facilitate optical alignment;
3. The efficiency of the diffraction grating should be as high as possible, and the groove density should provide sufficient spectral resolving power. A grating with d^{-1}=1200 l/mm is used, which is the best option commercially available.

4.2.1 Spectral resolution of diffraction grating

Based on grating equation (4.1), we can get

$$d^{-1}(\sin\theta_i + \sin\theta_{t0}) = \overline{\lambda} \tag{4.2}$$

Because $\Delta\lambda << \overline{\lambda}$, the angular spreading $\Delta\theta(\lambda)$ << θ_{t0}, then we can get

$$d^{-1} \cdot \cos\theta_{t0} \cdot \Delta\theta_t = \Delta\lambda \tag{4.3}$$

where $\Delta\theta = \theta_t - \theta_{t0}$ is the spreading of the diffraction.

The linear distribution of the spectral components projected on the focal plane of a doublet with focal length f is $\Delta x = f \cdot tg\Delta\theta_t \approx f \cdot \Delta\theta_t$, and then we can get the relation by applying Eq.(4.3) as

$$\Delta x = \frac{\Delta\lambda \cdot f}{d^{-1} \cdot \cos\theta_t} \tag{4.4}$$

4.2.2 Optical layout of the grating

Based on grating equation (4.1), we can get

$$2d^{-1} \sin\left(\frac{\theta_i + \theta_{t0}}{2}\right) \cos\left(\frac{\theta_i - \theta_{t0}}{2}\right) = \overline{\lambda} \tag{4.5}$$

As we adopt $\Delta\theta = \theta_i - \theta_{t0} = 26^0$, and for $\overline{\lambda} = 1320nm$ and d^{-1}=1200 l/mm, we can get from Eq.(4.5) the relation of $(\theta_i + \theta_{t0})/2 = 54.37^0$. This will give us the angular relations of $\theta_i = 67.37^0$ and $\theta_{t0} = 41.37^0$. It must be noted that the grating will be tilted at 41.37^0.

4.2.3 Spatial resolution at the detector array

If we assume that the focal spot size is the lateral resolution at the local plane, then

$$\Lambda = 4f\overline{\lambda}/\pi\phi \tag{4.6}$$

where ϕ is the incident beam size and f is the focal length.

4.2.4 Spetral distribution on the detector array

From the viewpoint of axial resolution and practical detection with limited SNR, we would assume that we wish to detect the spectral components down to 10% from the beak wavelength. Based on the spectral distribution, this gives the spectral range from 1260nm to 1370nm, or $\Delta\lambda_{10\%}$=110nm. Based on Eq.(4.4), the projection of these spectra will be

$$\Delta X = \frac{\Delta\lambda_{10\%} \cdot f}{d^{-1} \cdot \cos\theta_t} \tag{4.7}$$

4.2.5 Image depth of SDOCT

As discussed previously, the depth of SDOCT is determined, if not limited by tissue penetration depth, by

$$D = \frac{\overline{\lambda}^2}{4n\delta\lambda} \tag{4.8}$$

where $n \approx 1.4$ for most biological tissue, $\delta\lambda$ is the spectral resolution of the detection system. This is based on sampling theorem i.e., sampling 2 spots in one cycle.

4.2.6 Design parameters

For most biological applications, the image depth is about D=2mm. From Eq.(4.8), the spectral resolution needs to be:

$$\delta\lambda = 0.15\text{nm} \tag{4.9}$$

Considering that the pixel size of an InGaAs array is only 25μm, the ultimate focal plane resolution is limited by x_D=25μm. In order to project the spectra almost fully on the 1024-pixel InGaAs array (1000 pixels), the spectral spanned

focused beam should be distributed over the lateral range of close to X_D=25mm. Applying this to Eq.(4.7) , i.e., $\Delta X = X_D$, and with $\theta_{t0}=41.37^0$ and $\Delta\lambda_{10\%}$=110nm, we can get $f = \frac{d^{-1}\cdot\cos\theta_t\cdot X_D}{\Delta\lambda_{10\%}}$, i.e., f ≈142mm.

According to Eq.(4.4), the spectral resolution at such configuration will be $\Delta\lambda = \frac{d^{-1}\cdot\cos\theta_t\cdot x_D}{f}$ or $\Delta\lambda$ = 0.11nm. Because $\Delta\lambda < \delta\lambda$, the penetration will be increased to 2.7mm.

For the focal spot size for each spectrum to be less than 25μm, according to Eq.(4.6), the beam size should be $\phi = 4f\bar{\lambda}/\pi\Lambda = 4f\bar{\lambda}/\pi x_D$, or ϕ=9.5mm.

In summary, the parameters for the system designs are:

ϕ=9.5mm;

f ≈142mm;

$\Delta\lambda$ = 0.11nm;

θ_{t0}=41.4˚;

4.3 Spectral calibration

As SDOCT is based on spectral radar, the depth-resolved backscattering

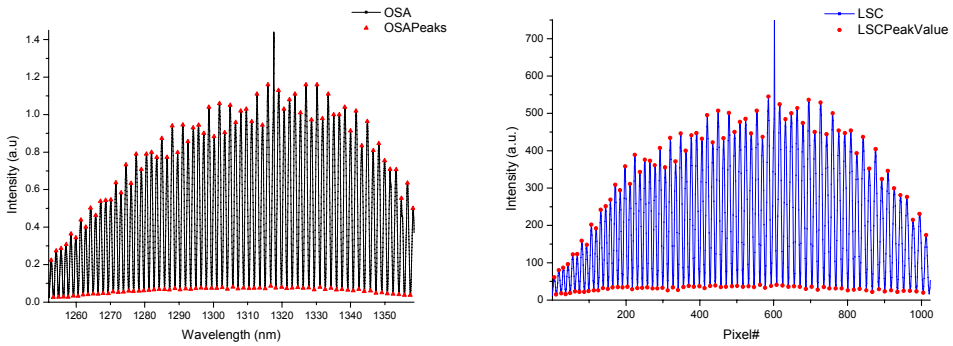

Fig.4. 3 Measured spectral curves by LSC and OSA for spectral calibration.

profile (A-scan) is encoded on spectral interferograms at different modulation frequencies, inverse Fourier transform performed to reconstruct the image, during which spectral calibration, i.e., conversion of the measured spectrographs from λ-space to k-space ($k=2\pi/\lambda$) is required to be uniformly resampled in k-space[57]. Stringent spectral calibration for SDOCT is crucial to avoid severe deterioration of axial resolution and SNR. Several calibration methods have been reported, including parametric iteration[53] and phase linearization[43]. Here, we use a simple fringe mapping method similar to that used in swept-source OCT.

To calibrate the system, a mirror is placed in the sample arm and moved axially (e.g., $\Delta L \approx 1mm$) until high-density fringes are detected by SDOCT and a high-resolution fiberoptic optical spectrum analyzer (Ando 6245, $\Delta\lambda=0.05nm$), as shown in Fig.4.3. By fitting the peaks of these interference fringes the spectral values of SDOCT (i.e., line InGaAs array) can be calibrated accurately both locally and globally across the entire 110nm spectral range. As shown in Fig.4.4, the measured axial resolution ($\Delta z_c=10.2\mu m$) of the reconstructed autocorrelation function or the axial point spread function (PSF) matches well with the theoretical result ($L_C \approx 10\mu m$).

4.4 Pixel Shift

For SDOCT, 1-D spectrograph is detected per A-scan; therefore, pixel shift can be easily implemented by either stepping the line InGaAs camera in the lateral direction or rotating the diffraction grating. The pixel size of the line InGaAs camera used in this study is Δx (e.g., 50 or 25μm), an interpixel shift of $\Delta x/2$ (i.e., 25 or 12.5μm) is implemented per A-scan to increase the pixel

resolution of the spectral camera. As for SDOCT, the ideal cross interference term (prior to camera digitization) between the reference and sample arms can be written as,

$$I(k) = 2S_{sr}(k) \cdot \cos(k\Delta L) \tag{4.10}$$

where $S_{sr}(k)=[S_s(k)\cdot S_r(k)]^{1/2}$ is the mutual-correlation spectrum and ΔL is the pathlength mismatch between the sample and the reference arms. Assume that the spectral resolution $\Delta\lambda$ resulted from a finite pixel size Δx is Δk (e.g., $\Delta k = (-2\pi/\lambda^2)\Delta\lambda$), the detection response of a pixel can be approximated by a rectangular function,

$$\prod(k) = \begin{cases} 0 & for \quad |k| > \Delta k/2 \\ 1/2 & for \quad |k| = \Delta k/2 \\ 1 & for \quad |k| < \Delta k/2 \end{cases}, \tag{4.11}$$

which is an integration or averaging function over the spectral range of k-Δk/2 and k+Δk/2. If the sampling comb function is defined as

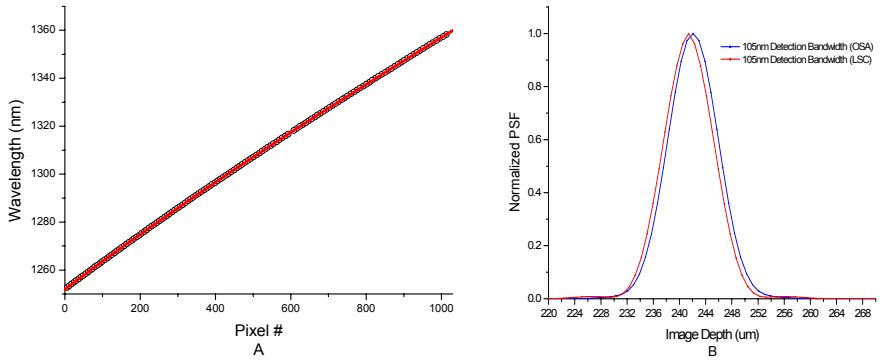

Fig.4. 4 A. Correlation between wavelength and pixel, with 3rd-order polynomial curve fitting;B. Comparison of reconstructed PSF with calibration for both OSA and LSC.

$$C(k) = \sum_{i=-\infty}^{-\infty} \delta\left[k - (k_0 + i\Delta k)\right] \tag{4.12}$$

where N=512 or 1024 is the pixel number of the InGaAs in camera and k_0 is the lowest wave number to be detected, then the measured spectrograph $I_D(k)$ will be given as[58]

$$I_D(k) = C(k) \cdot (\prod(k) \otimes I(k)) \tag{4.13}$$

and the resultant PSF with respect to the pathlength difference ΔL can be derived as,

$$\begin{aligned} PSF(\Delta L) &= \left| FT\left[I_D(k)\right] \right| \\ &= \left| FT[C(k)] \otimes FT\left[S_{sr}(k)\right] \otimes \left[\delta(L+\Delta L) + \delta(L-\Delta L)\right] \cdot \sin c(\Delta L \Delta k/2) \right| \\ &= \left| \frac{\pi}{\Delta k} \sum_{j=-\infty}^{\infty} \left[\delta(L - \frac{2j\pi}{\Delta k} + \Delta L) + \delta(L - \frac{2j\pi}{\Delta k} - \Delta L) \right] \otimes FT\left[S_{sr}(k)\right] \cdot \sin c(\Delta L \Delta k/2) \right| \end{aligned} \tag{4.14}$$

which represents a pair of pulses at ±ΔL whose envelop (i.e., autocorrelatiotion) is determined by the mutual spectrum $S_{sr}(k)$. More importantly, as the envelop is multiplied by the sinc(ΔLΔk/2) function which is the FFT product of the detector rectangular function in Eq.(4.12), Eq.(4.14) reveals that PSF decays with the increase of either pathlength difference ΔL or camera pixel size Δk (i.e., Δx)[39, 59]. The results of theoretical modeling of Eq.(4.14) are shown in Fig.4.5.

Because of limited spectral resolution Δk, the amplitude of PSF(ΔL) decreases with ΔL resulting in SDOCT signal degradation in the high-frequency range. Further analysis of Eq.(4.14) indicates that in the sub-Nyquist-sampling region or beyond the Fourier transform window where $\Delta L \geq \Delta L_{Nq} = 1/2 \cdot (j2\pi/\Delta k)\big|_{j=1} = \pi/\Delta k \approx 4.2$mm, the PSFs as exemplified by the red low

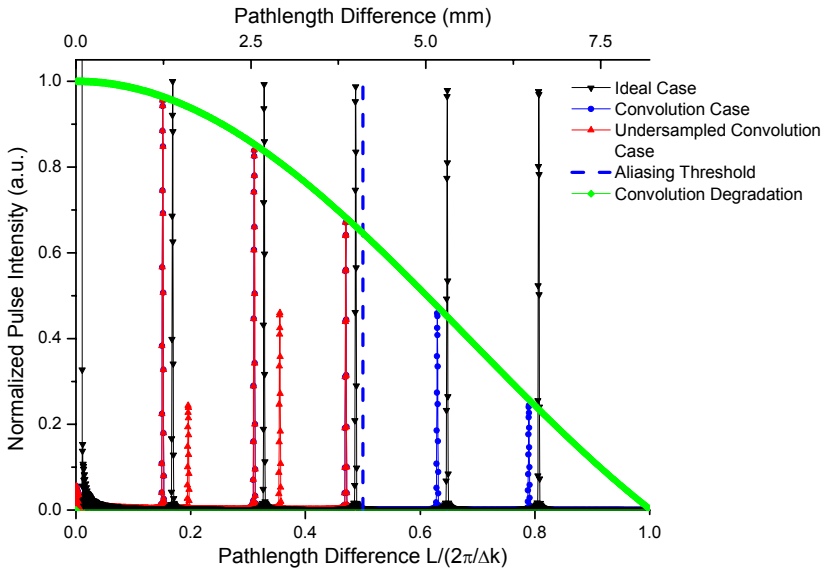

Fig.4. 5 Results of theoretical simulation of the PSF reconstructed PSFs. Simulation is based on the optical parameters given for our setup in Fig.4.1 and a 512-pixel camera and that with pixel shift are used.

peaks are rolled back to incorrect positions as a result of aliasing, which induces artifacts and increases the noise level in this region.

Fig.4.6 illustrates the principle of the pixel shift technique in which curve A is the input interference spectrograph, curves B and C are the measured results prior and post half interpixel shift, and curve D is the recombined result. As can be seen that although pixel shift does not enhance the original pixel resolution Δk or Δx (e.g., 25 or 50μm), it doubles the spectral sampling rate and thus preserves the high-frequency components of the interference modulation contributed mostly from deeper places with a higher ΔL. The sampling function for pixel shift is changed to

$$C_{ps}(k) = \sum_{i=-\infty}^{\infty} \delta\left[k - (k_0 + i\Delta k')\right] \tag{4.15}$$

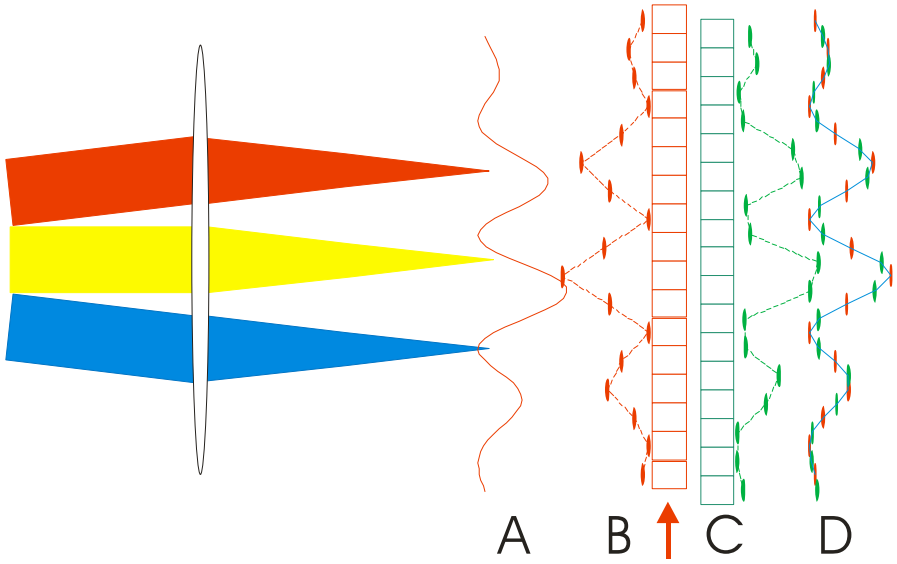

Fig.4. 6 A sketch illustrating the principle of interpixel shifted SDOCT. Spectrographs are of A) incident light, B) detected by a 512-element InGaAs array, C) detected after half-pixel shift, and D) recombined from B) and C), respectively.

where $\Delta k'=\Delta k/2$, and the PSF can be rewritten as

$$\begin{aligned} PSF_{ps}(\Delta L) &= \left|FT\left[I_D(k)\right]\right| \\ &= \left|FT[C_{ps}(k)]\otimes FT\left[S_{sr}(k)\right]\otimes\left[\delta(L+\Delta L)+\delta(L-\Delta L)\right]\cdot \sin c(\Delta L\Delta k/2)\right| \\ &= \left|\frac{\pi}{\Delta k'}\sum_{j=-\infty}^{\infty}\left[\delta(L-\frac{2j\pi}{\Delta k'}+\Delta L)+\delta(L-\frac{2j\pi}{\Delta k'}-\Delta L)\right]\otimes FT\left[S_{sr}(k)\right]\cdot \sin c(\Delta L\Delta k/2)\right| \end{aligned} \tag{4.16}$$

A comparison between Eq.(4.14) and Eq.(4.16) reveals that the decay of PSF amplitude with ΔL, determined by $\mathrm{sinc}(\Delta k\Delta L/2)$, remains unchanged; whereas the Fourier transform window or the Nyquist sampling range is doubled, i.e., $\Delta L'_{Nq}=2\Delta L_{Nq}=(2\pi/\Delta k)\approx 8.4$mm because $\Delta k'=\Delta k/2$. Fig.4.7 shows that as pixel shift doubles the Fourier transform window, the high-frequency components that are rolled back as noise and artifacts as discussed above can be restored. As reflected in Fig.4.5, the two blue curves beyond the Nyquist regime ($\Delta L\geq\Delta L_{Nq}$) can be recovered and the artifacts, i.e., the displaced two red curves are eliminated. Thus, the results of theoretical modeling suggest that interpixel

shifted SDOCT can enhance the system SNR in the high ΔL range and increase the effective imaging depth of SDOCT.

4.5 Results

To verify the theoretical prediction that interpixel shifted SDOCT enhances the system SNR in the high ΔL range and increase the effective imaging depth of SDOCT, we performed the following experimental studies. We first characterized interpixel shifted SDOCT by comparing the degradation of the autocorrelation functions measured without and with pixel shift. Then we performed *ex vivo* imaging of scattering biological tissue to examine the utility of interpixel shifted SDOCT in enhancing image contrast and imaging depth.

In the characterization experiments, we used the specular reflection from the surface of a microscope cover glass slide (R≈4%) in the sample arm to avoid

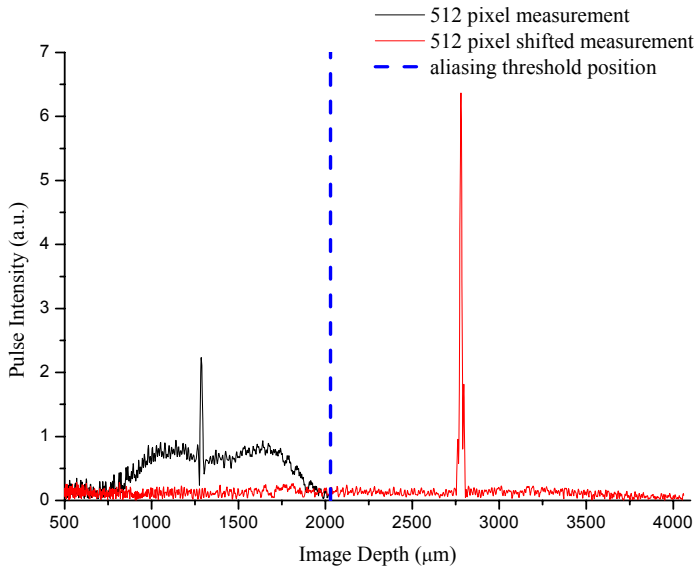

Fig.4. 7 Backscattering from a glass plate at depth of 2.8mm. Red and blue curves are reconstructed with and without pixel shift, respectively. The dashed line represents the aliasing threshold.

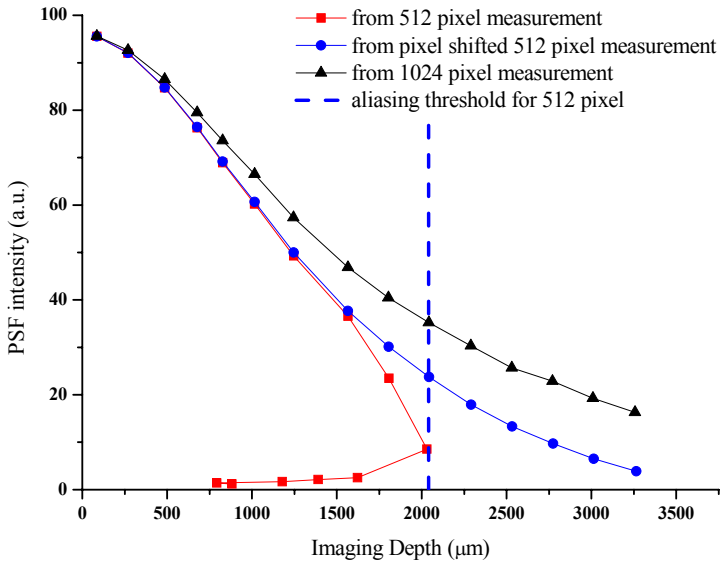

Fig.4. 8 Dependences of PSFs vs depth, reconstructed from 512-pixel, 512 inter pixel shifted and 1024-pixel SDOCT.

saturation of the camera. As the spectral spreading range for a 512-pixel camera is half of that for a 1024-pixel camera with the same pixel size, the optical setup of the spectral radar needs to be changed to accommodate the difference. To avoid the complication in changing optical setup and the complication induced by phase variation due to slow camera stepping (>10ms), a 1024-pixel camera was employed and binning of adjacent 2 pixels were used to simulate the 512-pixel camera with and without pixel shift. Fig.4.7 shows an example of the experimental results. According to Nyquist sampling criterion, the field of view of a FDOCT system is determined[60] by $\Delta z_{Nq}=\Delta L_{Nq}/2=\pi/(2\Delta k)=\lambda^2/(4\Delta\lambda)\approx$ 2.1mm (here the refractive index is assumed n=1 for free space), as indicated by the dashed blue line in Fig.4.7.

As predicted by Eq.(4.14), the PSF of the cover glass at Δz=2.8mm ($\Delta z>\Delta z_{Nq}$) is rolled back to $\Delta z\approx$1.3mm as artifacts in SDOCT image. Whereas with pixel shift,

this pulse is fully restored at Δz=2.8mm, shown as the red curve. It is interesting to see that the restored curve has almost 4-fold enhancement in the peak amplitude over the artifact curve. More importantly, the elevated noise in this range (e.g., ~3dB over the baseline noise level) induced by spectral sub-sampling or aliasing is effectively eliminated by pixel shift. It is important to be noted that this SNR enhancement (~13.6dB) can be crucial because it affects the

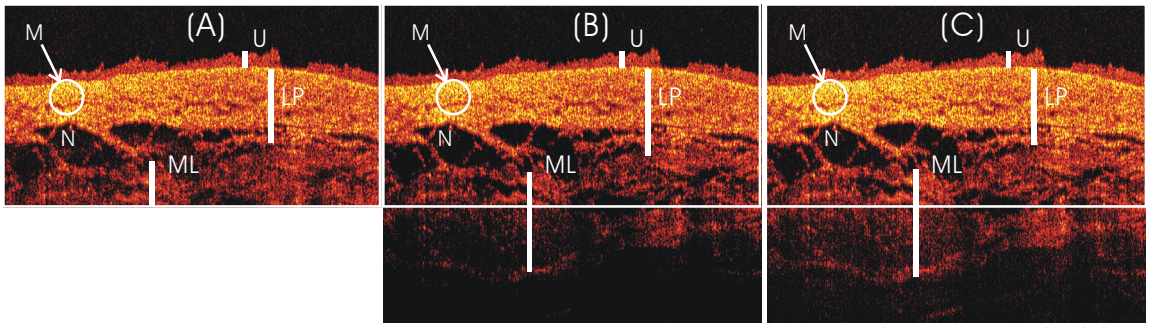

Fig.4. 9 Dog bladder imaged with A) 512-pixel, B) 512-interpixel shifted, and C) 1024-pixel SDOCT. U: urothelium; LP: lamina propria; ML: muscularis. Image dynamic ranges: A) 111.4dB, B) 111.5dB and C) 111.5dB. Image Size (lateral × axial): A) 6mm × 1.2mm, B) and C) 6mm × 1.8mm.

SDOCT image in the deep area (e.g., Δz>1.5mm) where image SNR is usually low for scattering tissue imaging.

Fig.4.8 summarizes the results of PSF measurements for different depths. As can be seen, the measured Nyquist sampling point is at Δz_{Nq}≈2.0mm, consistent with the theoretical prediction of Δz_{Nq}≈2.1mm. The red dotted curve (no pixel shift) and the blue dotted curve (with pixel shift) converge up to Δz≈1.5mm at which the red curve drops significantly due to decreased sampling rate and starts to roll back (aliasing effect) at the Nyquist sampling point Δz_{Nq}≈2.1mm. With simple pixel shift, both problems of aliasing and excessive decrease of signal amplitude with Δz are solved; therefore, the advantages of interpixel shifted SDOCT are

demonstrated. For comparison, the result of a true N=1024 line camera is included as shown by the dark dotted line. As predicted by Eq.(4.14) and Eq.(4.16) in which the envelop term is changed to sinc($\Delta L \Delta k/4$), PSF decays with Δz at a reduced slope, thus providing increased depth of field for SDOCT imaging.

In addition to system characterization study, *ex vivo* imaging study of biological tissue was performed to examine the enhancement of interpixel shifted SDOCT on image contrast and imaging depth. For instance, Fig.4.9 shows the comparative results of a dog bladder tissue imaged by 512-pixel SDOCT (panel A), 512-interpixel shifted SDOCT (panel B), and 1024-pixel SDOCT (panel C). All three images were taken at approximately 7.7fps and post image processing was implemented to reconstruct the 2D OCT images, representing image size (lateral $\times$ axial) of 6mm $\times$ 1.2mm (panel A) and 6mm $\times$ 1.8mm (panel B and C). The results show that all three images can well delineate the bladder morphology such as the low-scattering urothelium (U), the lamina propria (LP), and the muscularis (MS), but the image depth of panel A) is significantly less. As imaging was performed at 24 hours post formalin fixation, artifacts such as several large dark holes in the region of low lamina propria (connective tissue layer) induced by formalin infusion can be seen in all three panels. The SNRs, based on the measured maximum signal value against the noise background, are: 47.9dB (panel A), 48.2dB (panel B) and 48.8dB (panel C) respectively. It must be noted that this SNR quantization does not reflect the influence of aliasing noise effect because the noise level is taken from the dark area above the bladder, which is

the shot noise induced by the reference light. For example, the SNRs at point M in panels A), B) are comparable, and that in C) is 0.5dB higher, which is close to 0.9dB as shown in Fig.4.8. More interestingly, pixel shift can not only enlarge the image depth but also enhance the SNR in the deeper tissue region. For instance, in one of the dark holes N induced by formalin fixation in panel A), the noise level, induced by aliasing or roll-back artifacts, is 1.5dB higher than the corresponding spot in panels B) and C). In other words, pixel shift can effectively eliminate the aliasing noise due to sub-Nyquist sampling and bring the system back to shot-noise limit. This noise reduction, although 1.5dB, is critical to scattering tissue imaging because the SNR at deeper tissue region is usually very low as exemplified in Fig.4.8. For comparison, SNR in the muscularis in panel C) is slightly higher than that in panel B), which is in agreement with the theoretical prediction of Eq.(4.16) and with the experimental results in Fig.4.8. The increase of imaging depth by interpixel shift and the removal of the aliasing noise, although 1.5dB, are important for scattering tissue imaging. For instance, it is found in our clinical trial of SDOCT diagnosis of bladder cancers that due to bladder or scope motion or bladder asperities or invaginations (e.g., caused by tumorigenesis), the displayed OCT image or movie may slightly fall out of the designated axial position; therefore a larger depth of field such as 2.5mm or 3mm can be very useful. In this case, a simple modification using interpixel shifted SDOCT can not only increase the depth of field to 3mm but also enhance the SNR in deeper region (e.g., Δz>1.5mm) by eliminating aliasing noise induced by sub-Nyquist sampling.

4.6 Discussion and conclusion

Spectral-domain OCT offers enormous advantages over time-domain OCT in terms of imaging rate and signal-to-noise ratio and has been replacing time-domain OCT in many applications. However, one of the drawbacks of SDOCT is the degradation of image contrast with in the increase of pathlength difference ΔL or imaging depth Δz. As many OCT diagnoses are based on intensity variations, it may cause artifacts or misinterpretation of image features. This phenomenon of image degradation with depth is resulted primarily from limited spectral sampling resolution of the SDOCT system to resolve high-frequency spectral interference modulations from deeper areas with higher Δz. There are several parameters in the spectral radar design that may limit the detectable spectral resolution, which includes input beam size, grating diffraction efficiency, lens quality (spherical aberration, chromatic aberration, and field flatness), and the camera pixel size and number. With advanced CCD technology to date, cameras for short-wavelength SDOCT (e.g., from visible to 900nm region) may not be an issue in terms of sensitivity, speed, and pixel resolution, but line InGaAs arrays for 1300nm SDOCT are limited in both sensitivity and speed, and pixel resolution (e.g., N=512 or 1024 pixels). As previous study[48] and our theoretical analysis show that this may lead to problems such as coupling of sampling and spectral resolution, limiting the useful depth of field and inducing aliasing artifacts or noise. In this study, we propose to tackle the problem with pixel shift technique. This simple technique enables visualization of features beyond the field of view of conventional FDOCT and

enhances image contrast in deeper image region with $\Delta z \geq 1.5$mm, as has been demonstrated theoretically and experimentally. Nevertheless, a careful comparison between theoretical analysis (Fig.4.5) and experimental results (Fig.4.7 and Fig.4.8) reveals two major problems for the reconstructed point-spread function, i.e., profile skewness and additional amplitude drop. Theoretically, although aliasing occurs whenever undersampled, neither the amplitude nor the shape of PSF will be altered as shown by the red curve in Fig.4.5. On the contrary, significant artifacts are induced around the PSF if undersampled experimentally as shown by the dark curve in Fig.4.7, which may be partly attributed to imperfect k-space linearization. No matter how the system is calibrated, error is inevitably introduced in the processes of either curve fitting or numerical iteration. And the influence of this error on SDOCT signal reconstruction is highly depth dependent. If the spectral interferogram is undersampled, depth uncertainty is very sensitive to the calibration accuracy, resulting in signal skewness with calibration errors. Pixel shift, however, increases sampling rate, and thus provides more raw spectral data for image reconstruction to eliminate PSF skewness. In terms of excessive PSF amplitude drop with depth, as previously reported[59], it is resulted from the convolution (i.e., averaging) effect of finite focal spot size on the camera pixel, which can be seen by comparing the slope of experimental curves in Fig.4.8 with the slope of theoretical modeling (i.e. the green line) in Fig.4.5. This effect reduces the applicable depth range of pixel shift technique due to vanished useful information in deep image region, e.g., with $\Delta z \geq 3$mm. However, improvement on optical

design and alignment may further enhance the spectral resolution and thus recovery of PSF amplitude in this region. Both theoretical modeling (Eq.(4.16)) and experiment (Fig.4.8) show that a 1024-pixel system has higher PSF amplitude level; however, the difference is unremarkable, in particular, in case of scattering tissue imaging such as exemplified in Fig.4.9. In other words, a 512-interpixel shifted system may offer the advantage of cost effectiveness and image rate. It must be noted that for proof of principle, a 1024 pixel camera with pixel binning was used to simulate an interpixel-shifted 512-pixel camera. Currently pixel shift is limited to >10ms per step by stepping the bulky InGaAs camera. High-speed pixel shift (e.g., 7.7kHz or 0.1ms per step) can be implemented by direct PZT stepping of the InGaAs chip, as has been commonly used in interpixel shifted commercial CCD cameras. It should also be pointed out that in this preliminary study, only one-step interpixels shift with half pixel stepsize was performed. As a matter of fact, two-step interpixels shift with 1/3-pixel stepsize has be frequently used to date in high-resolution CCD camera technology, and thus may further improve the image quality of SDOCT, in particular ultrahigh resolution SDOCT at 1300nm range, in which limited pixel resolution of InGaAs remains a technical challenge.

Swept-source SDOCT excels in imaging speed and may permit in vivo 3D OCT and functional imaging (e.g., tracking of dynamic blood flow). However, the sweeping wavelength range of current swept sources is insufficient to permit ultrahigh-resolution OCT. A line camera based SDOCT has limited imaging rate, e.g., 30fps or less. However, the technique is of low cost, compact and reliable,

and easy to handle, it is highly suitable for most clinical applications (2D OCT at 4 fps is sufficient for most clinical diagnosis, such as endoscopic cancer imaging). More importantly, the technique is suitable for ultrahigh-resolution OCT (uOCT). For instance, 800nm spectral-domain uOCT has been reported using high-resolution CCD array (e.g., 2048 pixel or 4096 pixel). However, high-resolution InGaAs array (e.g., .1024 pixels) is not available. Pixel shift technique is a promising solution for ultrahigh-resolution line scan camera based SDOCT at 1.3 μm region.

In conclusion, a simple pixel shift technique is reported to improve the sampling rate and resolution of spectral-domain OCT. Both theoretical analysis and experimental comparison are presented. The results show that although interpixel shifted SDOCT does not necessarily increase the axial resolution, it increases the depth of field of SDOCT image and eliminates the artifacts induced by aliasing effect and therefore enhance the image contrast in the image areas with large depths (e.g., $\Delta z \geq 1.5$mm). Examples of *ex vivo* dog bladder tissue study clearly demonstrate the improvement of imaging depth and the image contrast in deeper layers such as low lamina propria and muscularis (e.g., $\Delta z \geq 1.5$mm), which is critical in clinical OCT application. If combined with our MEMS-based SDOCT endoscope, this technique has the great potential to enhance image fidelity and depth of field in our clinical diagnosis of bladder cancers and cartilage degeneration. The technique can also be of great interest to ultrahigh-resolution SDOCT at 1.3μm in which high-resolution and high pixel-density InGaAs cameras remain unsolved.

Chapter V

Fluorescence Guided Optical Coherence Tomography for the Diagnosis of Early Bladder Cancer in a Rat Model

Both theoretical analysis and preliminary results[12, 61] have demonstrated that OCT is a promising candidate for optical biopsy in bladder cancer diagnosis, as discussed in previous chapters. However, for *in vivo* clinical applications, the current scanning range for endoscopic OCT imaging is limited. For instance, the reported range for OCT endoscopy is typically ~4mm while the diameter for human bladder is ~10cm. This small scanning range prevents efficient OCT examination of the whole bladder wall. Meanwhile, studies on 5-ALA induced fluorescence cystoscopy show very high sensitivity (90~96%) for bladder cancer diagnosis[5, 8], but the relatively low specificity (~60%) remains to be improved. To combine the advantages of these two imaging modalities and enhance the specificity and efficacy (i.e., reducing imaging time) for early bladder cancer diagnosis, fluorescence guided OCT (FG-OCT) cystoscopy has been proposed in our lab[17]. Here, a detailed comparative study is performed based on a rat model in which bladder tumors were developed via MNU instillation and imaged by white-light, 5-ALA fluorescence, OCT and histology. Because imaging was performed longitudinally during tumorigenesis, this study allowed us to examine the utility and limitations of these techniques in detecting specific features such as inflammation, and precancerous and cancerous lesions. This

part of study has been published in Journal of Urology in 2005[19]; the discussion that follows is drawn from the content of that paper.

5.1 Materials and methods

A standard rat bladder cancer model[62] was employed in which TCCs were induced chemically by intravesical MNU instillation. 54 female Fisher 344 rats were used in the study. After general anesthesia, the solution consisting of 1.5mg of MNU in 0.15ml of PBS vehicle, was instilled intravesically into rat bladder through a $5^1/_2$" Tom Cat catheter followed by 10 minutes of occlusion. The rat was then allowed to void freely and yet remained anesthetized for 5 minutes before anesthesia was curtailed. Each rat received 3 additional biweekly instillations during which antibiotics were added prophylactically to their drinking water to prevent bladder infection and possible strictures caused by MNU instillation. Recent studies[63, 64] indicated that TCCs routinely developed starting roughly during week 12 when imaging studies were begun to track weekly the changes induced by tumorigenesis. All the animal procedures were performed in compliance with animal care regulations and were approved by the Stony Brook University Animal Care and Use Committee.

During weeks 11-33, 2-3 MNU-treated rats were studied weekly. Prior to imaging, 5-ALA, freshly dissolved in 10% normal saline (0.9%) vehicle at 100mg/ml (pH=5.5), was instilled intravesically into each rat bladder using urethral cannulation of 0.2ml/100g body weight and remained occluded for 2-2.5hrs. Then, anesthesia was curtailed and the rats were free to void for 2 more hours to yield peak PpIX production[65] for fluorescence examination. The rats

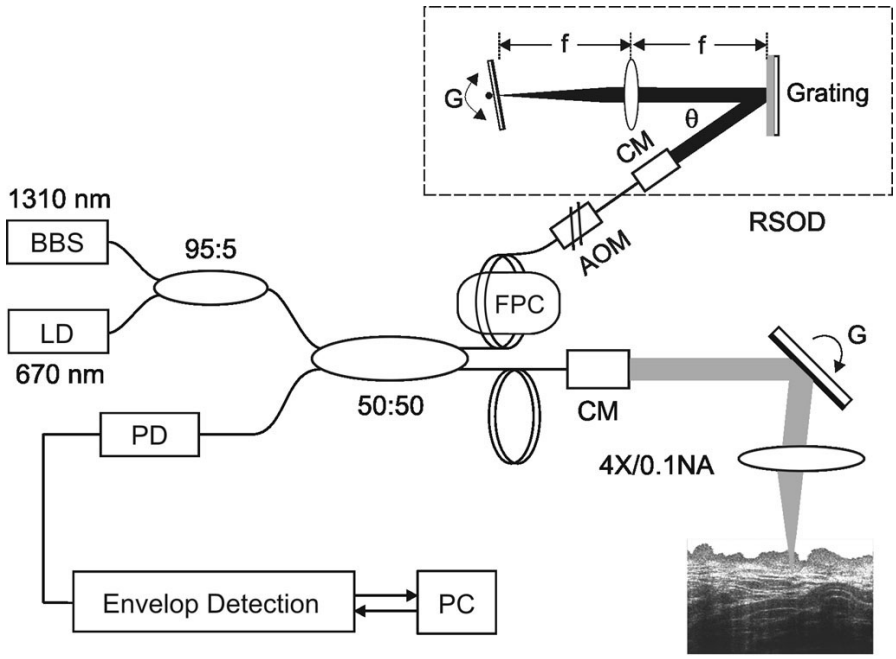

Fig.5. 1 A sketch of an OCT setup for ex vivo study. BBS: broadband light source, LD: red aiming laser; PD: photodiode; CM: fiberoptic collimator, G: galvo mirror; FPC: fiber polarization controller.

were euthanized using anesthetic overdose and the intact bladder was removed by a midline laparotomy incision, opened from the urethra to the dome and mounted uniformly on a ring holder placed in a modified Ringer's buffer solution (37°C, pH7.4) to undergo imaging. Hematoxylin and eosin (H&E) stained histology was performed on sections precisely marked during OCT scans to confirm the identifications made during imaging studies.

A Nikon stereoscope with a 1X Plan APO UV objective was modified for fluorescence imaging, in which blue light (λ=380-420nm) was used for fluorescence excitation to yield red fluorescence emission (λ=620-700nm) from bladder lesions imaged by a 12-bit CCD camera which was easily switchable to white-light mode via a liquid crystal tunable filter. A schematic of the OCT setup used in this study is depicted in Fig. 5.1. A broadband light source was employed

to illuminate the OCT system which was based on a fiberoptic Michelson interferometer. The pigtailed output power of BBS was 13mW, and central wavelength was 1320nm with spectral bandwidth $\Delta\lambda$=78nm, thus yielding a coherence length of L_C=9.8μm (i.e., axial resolution). A grating-lens-based rapid scanning optical delay line (RSOD) was used in the reference arm to provide 2.8mm axial scan (in free space) at a rate of 1 kHz, and a fiber acousto-optic modulator (AOM) was inserted prior to RSOD to provide an ultra-stable Doppler frequency shift at 2MHz for optical heterodyne detection. In the sample arm, light exiting the fiber was collimated to ϕ4.8mm, deflected laterally by a servo mirror and focused on the bladder surface by a 4X/0.1NA objective. A red diode laser (λ=670nm) was introduced to guide the OCT scan and the later histological sectioning of the lesions. OCT imaging was fully automatic and in near real time (>4 frames/s). Both the lateral and axial resolutions of OCT setup were roughly 10μm.

The sensitivity and specificity were computed based on a 2×2 frequency table for fluorescence and FG-OCT. Histology served as the objective standard. Fluorescence was considered positive ('+') when a lesion showed red fluorescence or appeared papillary under white light and negative ('-') otherwise. The threshold for fluorescence diagnosis was set to 25dB over the dark baseline of normal urothelium. The result of OCT was classified as normal, hyperplasia, or TCC based on increased urothelial thickening and backscattering, but only TCC was considered positive ('+'). Chi-square analysis was employed to compare the

sensitivity and specificity of fluorescence and FG-OCT, in which $p<.05$ was considered statistically significant.

5.2 Results

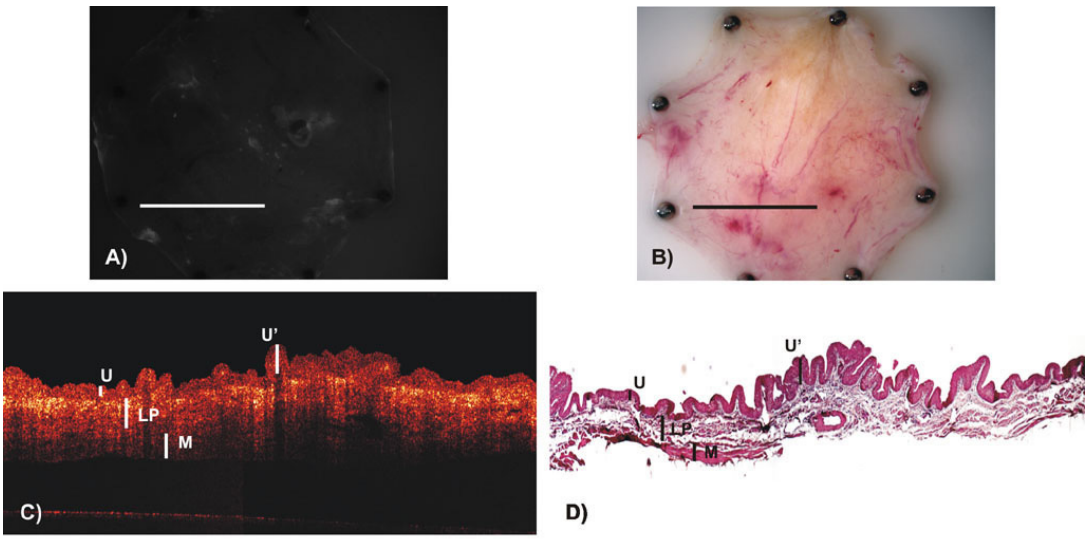

Fig.5. 2 Rat bladder imaged at week 22 post MNU instillation. A) 5ALA fluorescence image, B) white-light image; C) cross-sectional OCT, D) corresponding histology. Bars in A and B indicate the lateral margin for images C and D. U: normal urothelium; LP: lamina propria; M: muscularis, U': urothelial hyperplasia.

OCT delineates the micro-morphological details of bladder, e.g., urothelium (U), lamina propria (LP), muscularis (M), and in some cases the attached fatty layer (F) owing to their backscattering differences: in normal bladder, U appears as a low scattering thin layer, LP is of high scattering, M is of high scattering but showing large bifurcated structures, and F appears as barely resolved fat cells[61]. Our recent study further demonstrates that OCT detects acute responses of MNU instillations (e.g., urothelial denudation, LP edema) and chronic changes (e.g., hyperplasia to TCC) of rat bladder based on urothelial thickening and backscattering enhancement[12]. In contrast to morphological

delineation, 5-ALA fluorescence detects biochemical alterations associated with carcinogenesis.

All fluorescence images presented here are 12-bit grayscale *en face* images with a full field of view of 17mm × 23mm identical to the corresponding white-light images. All OCT images are 12-bit grayscale cross-sectional images (6mm lateral × 2.1mm vertical in bladder tissue) with no post-image processing. OCT scans were performed in lesions identified by fluorescence ('+') and those missed by fluorescence ('-') but suspicious under white light. A set of 4 images (i.e., white-light, fluorescence, OCT, and histology) are presented for each lesion. Fig. 5.2 shows a bladder lesion which was invisible under either white-light or fluorescence ('-'); whereas OCT delineated morphological details of normal bladder such as U (~85μm thick), LP (~320μm) and M (~150μm) and diagnosed it as hyperplasia exhibiting thickened, low-scattering urothelium U' (~250μm) as

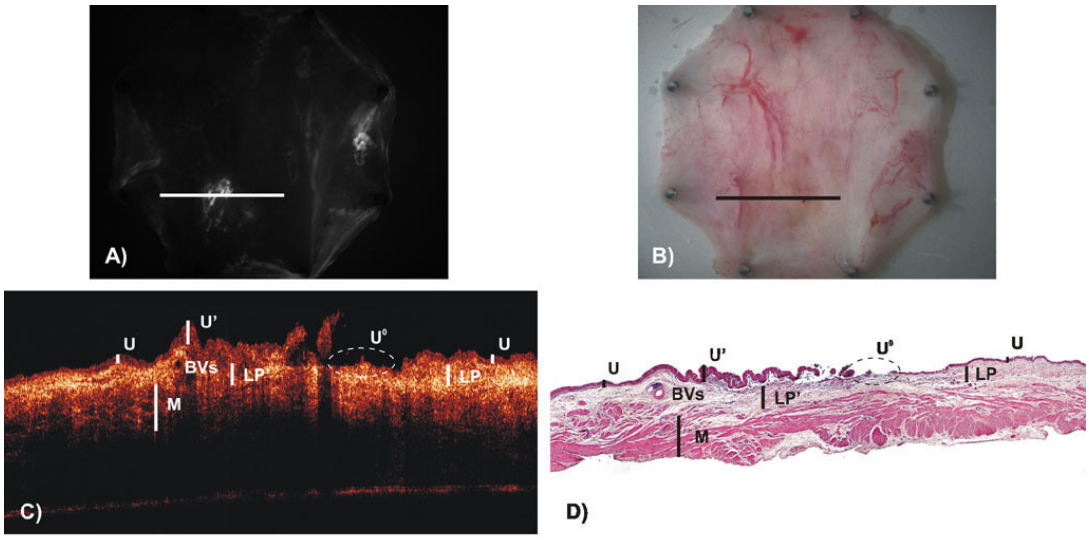

Fig.5. 3 Rat bladder imaged at week 30 post MNU instillation. U': urothelial hyperplasia; U^0: denuded urothelium; LP': slight edema, chronic inflammation; BVs: blood vessels.

confirmed by histology.

During the study, a total of 63 hyperplastic lesions were encountered. Fluorescence detected 38 as normal ('-'); whereas OCT detected all 63 lesions and was able to identify 57 of them as hyperplasia ('-') as later confirmed histologically. Fig. 5.3 exemplifies that many hyperplastic lesions appeared normal under white-light but were misdiagnosed by fluorescence. OCT diagnosed the lesion as minor hyperplasia U' (~220μm) with urothelial denudation (~0.6mm wide) in the adjacent area U^0. Morphological details identified by OCT were confirmed by histology, which include 2 small blood vessels (BVs) and inflammation of LP (LP'), the latter identified by decreased scattering due to edema as compared to normal. During the study, 25 out of 63 hyperplastic lesions were misdiagnosed fluorescently ('+') contributing primarily to the low specificity of 5-ALA fluorescence; nevertheless, these lesions were

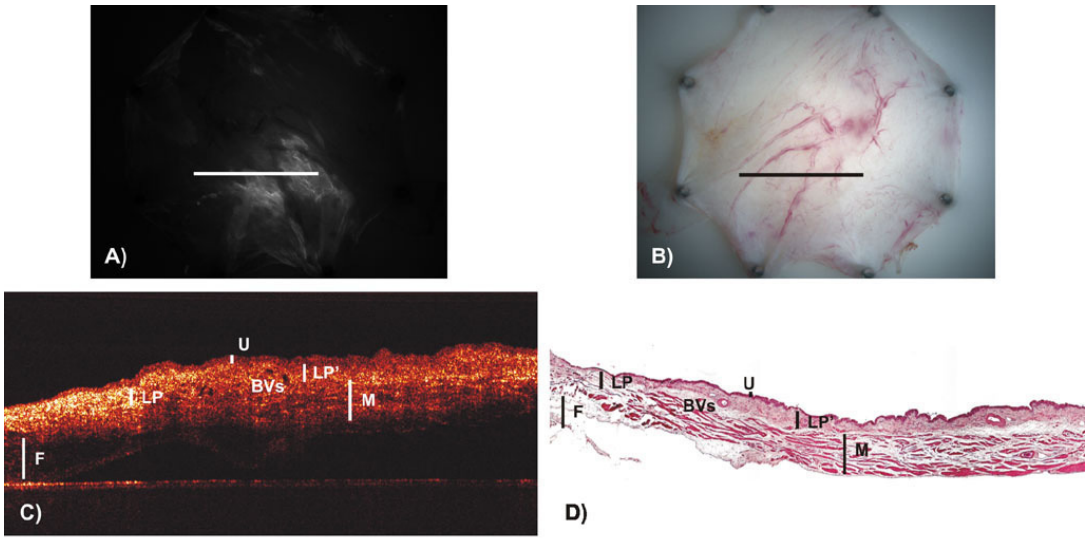

Fig.5. 4 Rat bladder imaged at week 18 post MNU instillation. F: fatty layer; LP': inflammation; BVs: blood vessels.

fully detected and 90% were differentiated by OCT as hyperplasia ('-').

In addition to urothelial hyperplasia, minor inflammatory lesions and even normal bladders were misjudged by fluorescence. In Fig. 5.4, the lesion, which was invisible under white light but was diagnosed fluorescently ('+'), was easily diagnosed as minor inflammation (LP') by OCT as confirmed by histology. Eight normal or inflammatory lesions were encountered, among which 3 were fluorescently diagnosed but were corrected by OCT. Compared with hyperplasia, this group contributed negligibly to the high false-positive rate of fluorescence diagnosis.

Fig. 5.5 shows 2 lesions occurring in one specimen. One lesion (C-D)

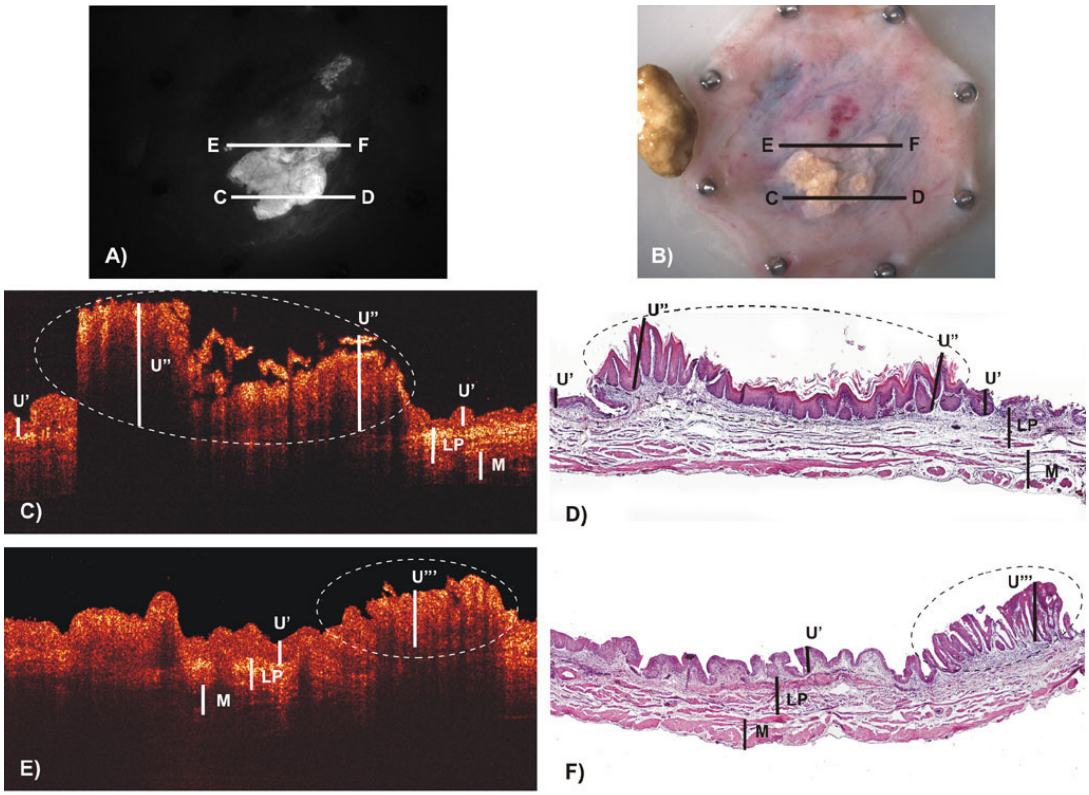

Fig.5. 5 Rat bladder imaged at week 28 post MNU instillation. The bars C-D and E-F mark the lesions imaged in panels C, D and panels E, F, respectively. U': hyperplasia; U": SH; U"': papillary TCC (grade 1/3, T0).

supporting a large stone was visible but the other (E-F) in the surrounding area might be missed under white light. Both lesions were diagnosed '+' under fluorescence. Based on urothelial thickening and backscattering increase, OCT diagnosed both lesions as TCCs ('+') whereas histology showed U'' (C-D) as squamous hyperplasia and U''' (E-F) as TCC (grade 1/3, stage T0). A total of 26 papillary or squamous lesions were encountered, which included papilloma (Pap), squamous hyperplasia/metaplasia (SH/SM), and papillary TCC. Among 12 non-TCC lesions later confirmed histologically, the false-positives were 11 by fluorescence and 10 by OCT. As both SH/SM and papillary TCC exhibited urothelial thickening and backscattering increase, OCT might not have sufficient sensitivity to differentiate these two types of lesions, which was the major cause of false-positives in OCT diagnosis. However, all 12 such lesions were SH/SM or Pap associated with lithiasis; so, these false-positives can be reduced to 0% for OCT and 8% for fluorescence if complemented by white light.

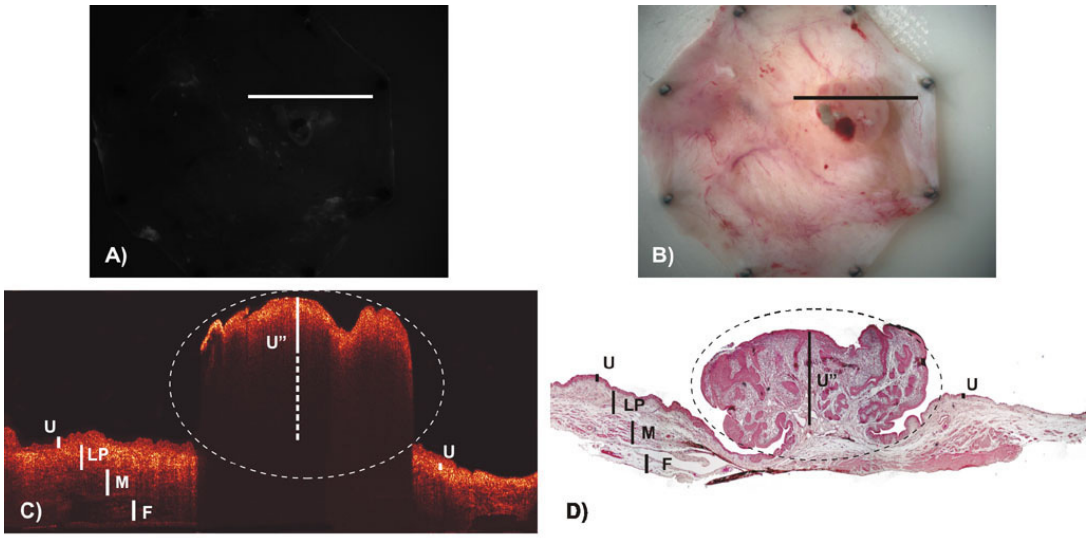

Fig.5. 6 Rat bladder imaged at week 32 post MNU instillation. U": papillary TCC (grade 2/3, T1).

Although 5-ALA fluorescence is highly sensitive, it occasionally missed TCCs that could be identified by white light and OCT. In Fig. 5.6, the lesion, missed by fluorescence, was clearly visible under white light due to its exophytic growth. Based on enhanced urothelial backscattering and rapid signal decay due to increased heterogeneity and blood absorption, this lesion was diagnosed as papillary TCC (grade 2/3, stage T1) by OCT and was confirmed histologically.

A total of 97 biopsied lesions were obtained from 54 female Fisher 344 rats among which 14 were histologically confirmed TCCs. The results are summarized in Table 1.

Table 5. 1 Summary of the Experimental Results

	NR	Infl	UH	SM/SH	Pap	TCC	Subtotal
5-ALA (+)	2	1	25	10	1	11	50
5-ALA (-)	3	2	38	0	1	3	47
OCT (+)	0	0	6	10	0	14	30
OCT (-)	5	3	57	0	2	0	67
Subtotal	5	3	63	10	2	14	97

NR: normal; Infl: inflammation; UH: urothelial hyperplasia including papillary UH; SH/SM: squamous hyperplasia/metaplasia; Pap: papilloma; TCC: transitional cell carcinoma.

Three TCCs were missed by fluorescence but were excluded if complemented by white light. Fluorescence false-positively diagnosed 39 benign lesions, while for OCT there were only 16 such cases, among which 10 were severe SH/SM associated with lithiasis and were excluded if complemented by white light. According to the results, Table 2 reveals that on a per lesion basis, the sensitivity and specificity of fluorescence diagnosis are 79% and 53%,

respectively; whereas for FG-OCT these are improved to 100% and 93%, respectively.

5.3 Discussions

Even with the advent of highly sensitive screening techniques, noninvasive cystoscopic localization of early TCCs remains a clinical challenge. Incomplete transurethral tumor resection (e.g., positive margins or undetected lesions) has been a major cause of tumor recurrence and repeat surgical intervention due to the limited accuracy of white-light cystoscopy in identifying tumor margins.

Table 5. 2 Sensitivity and Specificity Results

	Fluorescence-only		White-light complemented	
	Sensitivity	Specificity	Sensitivity	Specificity
5-ALA	79%	53%	100%	65%
FG-OCT	100%	81%	100%	93%

Complemented by white-light imaging, some papillary TCCs missed by 5-ALA fluorescence were captured and some squamous hyperplastic or metaplastic lesions falsely-diagnosed by OCT were corrected.

Because white-light cystoscopy is limited to the diagnosis of gross morphological patterns of lesions (e.g., large, higher-stage papillary alteration), urologists have been seeking more effective methods to enhance the diagnosis of early TCCs and reduce the risk of missing cancerous lesions as well as unresected tumor. Imaging diagnosis of fluorescence induced by systemic administration and more recently intravesical instillation of photosensitizers (e.g., 5-ALA) has shown promising results for drastically enhanced diagnosis (>90% sensitivity) of early TCCs over conventional white-light cystoscopy. Because of

tumor-specific labeling, the technique is highly sensitive with a mean 27dB fluorescence enhancement of lesions, thus substantially reducing imaging duration. However, the relatively low specificity of 5-ALA induced fluorescence of PpIX (60-70%) remains to be improved. OCT is capable of instant, high-resolution imaging of bladder morphology, and our recent studies suggested its ability to detect and stage tumorigenesis based on urothelial backscattering increase as a result of nuclear-to-cytoplasmic ratio change associated with hyperplasia, dysplasia, and neoplasia[12]. Recent technological advances have permitted endoscopic OCT for high-resolution *in vivo* imaging suitable for clinical diagnosis[62]. Although OCT imaging can be performed in real time, complete scanning of the entire mammalian bladder wall is time consuming, as the field of view per OCT scan is limited. To tackle this problem, we recently proposed using FG-OCT and have demonstrated the technical capability of FG-OCT endoscopy[17].

In this study, we examined the utility and potential limitations of FG-OCT based on a rat bladder tumorigenesis model in which parallel fluorescence, OCT, and histology were performed longitudinally following MNU instillations. Therefore, various features of tumorigenesis were evaluated, varying from urothelial disruption and inflammatory lesions to hyperplasia, dysplasia, and TCC. A total of 97 lesions were imaged from 54 MNU-treated rats among which 14 TCCs, 10 SH/SM, 2 Paps, and 63 hyperplastic lesions were obtained. 5-ALA fluorescence was highly sensitive (~79%) and could reach 100% sensitivity if complemented[5] with white light, but the specificity was limited to 53%. The high

false-positive rate was primarily due to urothelial hyperplasia (~92%), among which ~40% were false-positively identified as TCCs. These false-positives of fluorescence were immensely reduced by OCT to ~7% (or 19% without white-light correction of squamous lesions), and the results presented in Table 2 clearly demonstrate the potential of FG-OCT to substantially enhance the specificity to 93%. The rat bladder is small and can thus be sequentially scanned by OCT in less than 1 minute; nevertheless, the advantage of fluorescence guidance (with field of view >ϕ30mm) in reducing examination time is crucial for imaging larger bladders, e.g., human bladder in clinical diagnosis. We anticipate reducing the scoping time of OCT from ~15 to ~3 minutes by FG-OCT. In terms of specificity, data analysis reveals that the false-positives of OCT resulted primarily from difficulties in differentiating TCCs from SH/SM because in either case the backscattering was enhanced due to heterogeneity and outgrowth. A major goal of OCT cystoscopy is the detection of early flat TCCs such as CIS; however, in the MNU rat model, most lesions become papillary prior to invading TCC, and CIS was not seen. Moreover, hyperplasia is rarely seen in humans, the results in the rat may not reflect the clinical performance of OCT[11] or FG-OCT. We plan to address this problem by orthotopic induction of tumors using AY-27 cells, allowing us to investigate minute superficial dysplastic and neoplastic changes with far less papillary outgrowth and providing a more realistic projection of its efficacy in humans. Nevertheless, as our OCT diagnosis of TCC is based on urothelial backscattering enhancement rather than urothelial thickening, the results provide an important baseline for future clinical studies.

5.4 Conclusions

Results of this comparative study demonstrate that FG-OCT combines the advantage of the high sensitivity of fluorescence in detecting cancer-specific biochemical changes and the high resolution of OCT in diagnosing morphological changes induced by tumorigenesis. This new technology promises to be an efficient means of early bladder cancer diagnosis with an estimated 100% sensitivity and 93% specificity. The results justify the development of FG-OCT cystoscopy for early clinical study.

Chapter VI

Bladder cancer diagnosis with TD-OCT: *in vivo* study

Encouraged by the exciting results from the ex vivo study, we improved MEMS-based endoscopic OCT probe design and studies have been performed to evaluate the capability of OCT for bladder cancer diagnosis *in vivo* in a standard pig acute inflammation animal model and in clinical applications with the time domain OCT (TD-OCT) system. Experimental results have shown that the current endoscopic OCT system provide high imaging performance with signal to noise ratio of 108~110 dB, comparable with the bench-top system. The promising results suggest that endoscopic OCT imaging can provide high fidelity physiological structure of bladder and thus is a very promising technique for diagnosis of bladder transitional cell carcinomas (TCCs).

6.1 Experimental setup

OCT system setup has been briefly summarized here. As depicted in Fig.6.1, a high-power broadband source (BBS) is employed, which can provide pigtailed output power of 13mW, central wavelength at $\lambda=1320nm$ and full-width-half-maximum spectral bandwidth $\Delta\lambda=78nm$ (resulting in a coherence length $L_C \approx 10\mu m$). The light is delivered to a fiberoptic Michelson interferometer in which light is divided equally to reference and sample arms. For visual guidance, the red light from a 670nm diode laser is coupled into the input arm via a 95%:5% fiber coupler. In the reference arm, a grating-lens-based optical delay line is used to implement longitudinal scan. Through a modified FC/APC connector, the

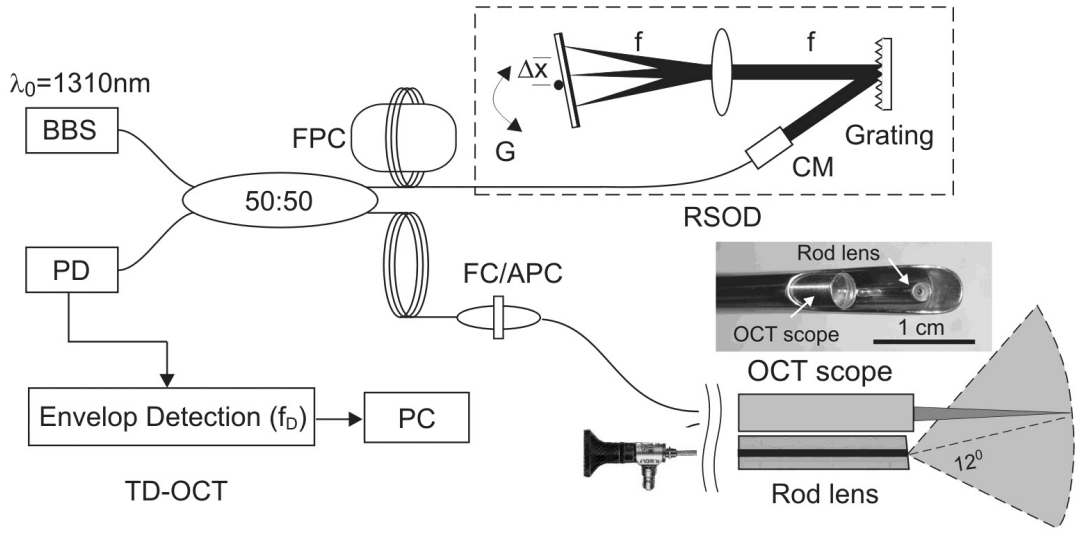

Fig.6. 1 Schematic diagram for endoscopic OCT system. BBS: broadband light source; FPC: fiber polarization controller; FC/APC: angled fiber connector; RSOD: rapid-scanning optical delay line; CM: collimator; G: servo mirror; PD: photo diode; PC: personal computer.

sample arm is connected to a MEMS-based pigtailed OCT endoscope, which is detailed in the following subsections. The light scanning range in the OCT endoscope is ~4.2mm (limited by the scope size) in the transverse direction at a repetition rate up to 100Hz. Based on the above parameters used in our setup, the axial resolution is ~10μm, and the transverse resolution is ~12μm.

6.2 MEMS-based OCT endoscope design

OCT is based on fiber optics, therefore it is readily incorporated with current endoscopy to deliver light inside the body. Various designs for sample arm miniaturization have been implemented in OCT application for internal organs[10, 13, 14, 66-68]. Since the introduction of MEMS technology to OCT endoscopy[13], we have made substantial improvements over the last years on the design and packaging of MEMS-based OCT endoscopes. Experimental results show that the current MEMS-based endoscopic OCT design provides

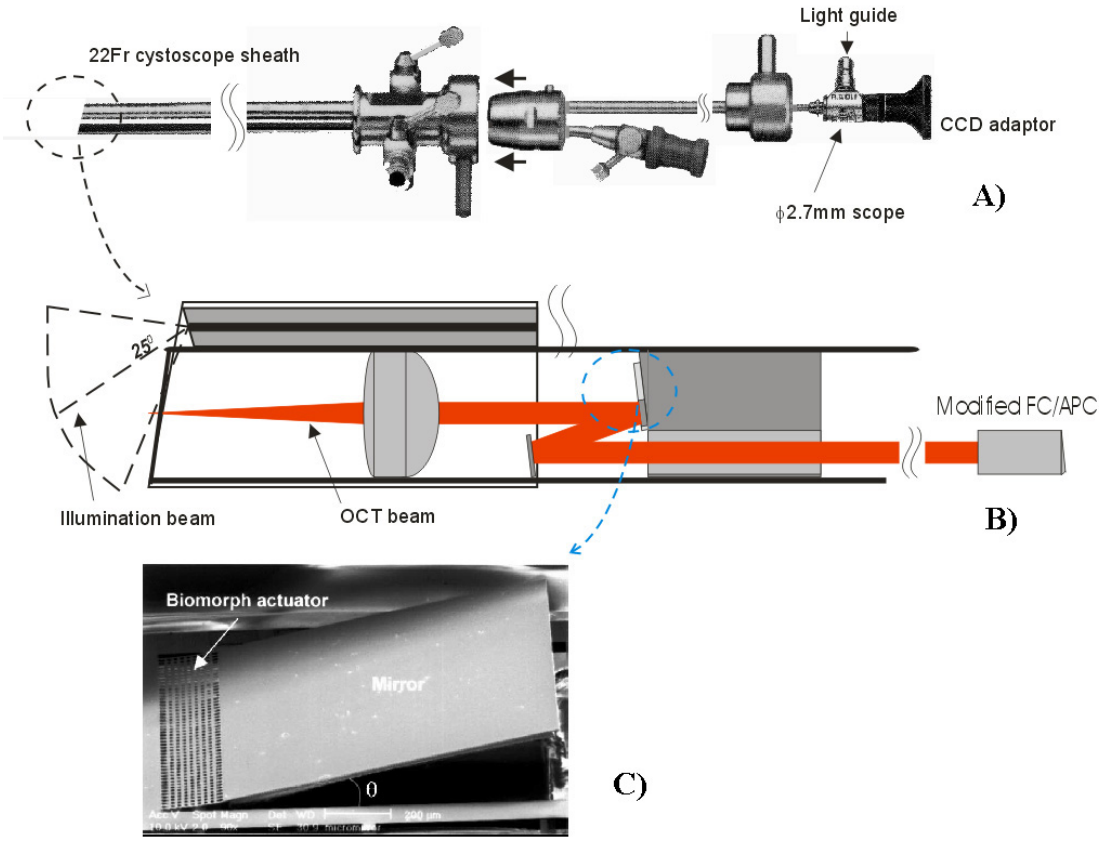

Fig.6. 2 Photo of MEMS-mirror base OCT endoscope (A), schematic diagram of distal OCT probe (B) and SEM photo of MEMS mirror (C)[13].

high fidelity imaging performance at SNR of ~108 dB, comparable to bench-top system.

The optical layout of MEMS endoscope is shown in Fig. 6.2 (A-B). It is a pigtailed OCT catheter through a modified FC/APC fiberoptic connector that can be inserted into the ϕ4mm instrumental channel of a 22Fr commercial endoscopic sheath for *in vivo* imaging study. The optical layout in the distal OCT scope is illustrated, which enables instantaneous visual guidance for EOCT imaging via a ϕ2.8mm scope with either white light or fluorescence [56]. In the OCT endoscope, the light exiting the SM fiber is coupled by a 0.25-pitch selfoc lens to a ϕ1.1mm collimated beam and deflected by a fixed reflecting prism and a

MEMS mirror. The transverse light scanning in the OCT scope is facilitated by the MEMS planar mirror which is actuated by the applied electrical voltage. The transversely steered beam is then focused by a laser doublet (f10mm/ϕ5mm) to a roughly ϕ12μm spot size on the front focal plan of the OCT scope where the bladder wall under examination is placed.

The MEMS mirror employed in the endoscope is designed and fabricated by one of our collaborators, the group led by Dr. Xie in electric engineering department of Florida University. This chapter serves as a brief description. Fig. 6.2 (C) shows the scanning-electron micrograph (SEM) of the MEMS mirror structure. The current model used in OCT endoscope is a single-crystalline silicon chip fabricated by a complementary metal-oxide semiconductor (CMOS)–MEMS process[13, 69]. Its hinge is an Al-SiO_2 bimorph thermal actuator and can be electrothermally actuated. Because of residual stress the hinge curls up to an initial bending angle (~20˚) above the chip plane, and bending angle θ changes with the temperature (current/voltage) within the bimorph due to a difference in the thermal expansion coefficients between two thin layers. The relationship between actuation angle θ and external voltage V can be approximated as[69]

$$\theta \propto V^2 \qquad (6.1).$$

The resistance of the embedded polysilicon heater is 1.6~2.2 kV. Preliminary test has shown that the maximal electrical voltage applied to the heater is below 30V, making it a safe and low consumption device. The resonant frequency of the CMOS MEMS mirror is >100 Hz, sufficient for one-dimensional endoscopic laser scanning application. According to Eq. (6.1), nonlinear correction to the applied

voltage is required to obtain linear scanning across the sample. The results on a test stage show that the mechanical scan angle is of the order of ±12˚, yielding a

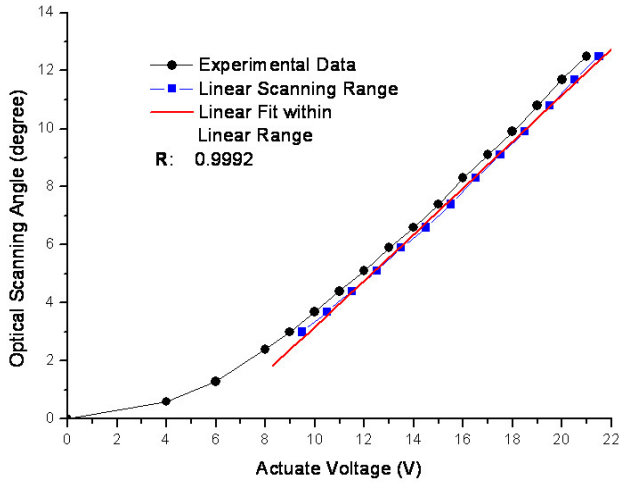

Fig.6. 3 Optical scanning curve for MEMS mirror. R: linearity coefficient. Experimental data are intentionally shifted at linear (high voltage) range for visual clarity.

±24˚ optical scan angle for beam steering. During our in vivo studies, the scan range is ~4.5 mm when an f=10 mm achromatic lens is used, eventually limited by the diameter (5mm) of the endoscope sheath, which houses the MEMS scanning mirror.

To evaluate the scanning nonlinearity of the MEMS mirror and provide necessary corrections of actuating voltage across the mirror, the electro-mechanical response of MEMS mirror has been measured. A typical scanning curve is shown in Fig. 6.3 as an example. Consistent with Eq.(6.1), there exists some nonlinearity at low voltage range. However, the optical angle increases linearly with applied voltage in high voltage range (>9V in Fig. 6.3). To characterize the nonlinearity quantitatively, the experimental data are linearly

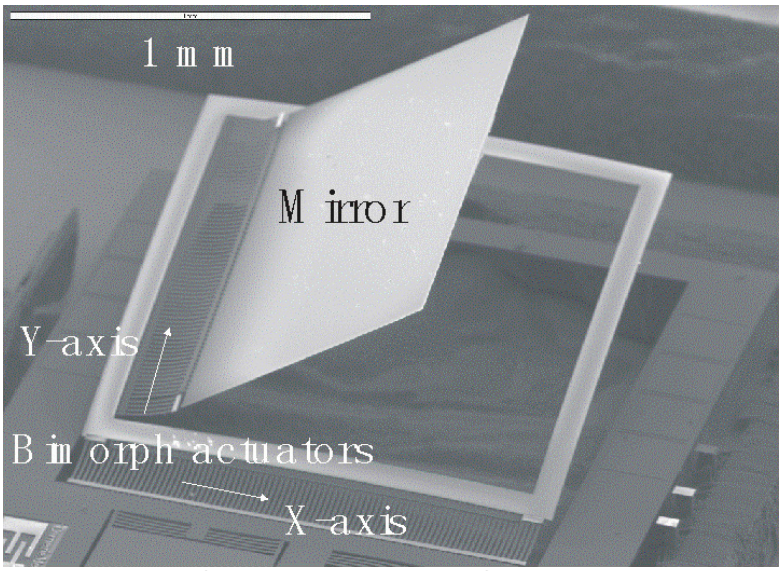

Fig.6. 4 2D MEMS mirror structure under SEM.

fitted, resulting in linearity coefficient R=0.9992, which is sufficient for endoscopic application of laser scanning.

With development of MEMS technique, multiple dimension mirror, such as 2D or even 4D mirror, has been available. For instance, Fig. 6.4 shows the structure of a 2D MEMS mirror examined with SEM. These mirrors offer more freedom in terms of controlling. This can not only facilitate optical alignment, especially for endoscopic application where space is very limited, but also enable focus tracking for current system. In combination with sweep source OCT, 3D or even 4D imaging in real time is possible in near future, making OCT endoscopy much more attractive, particularly in bladder cancer diagnosis with *en face* scanning capability.

6.3 Animal model for in vivo endoscopic OCT study and human subjects

The animal model employed in this study has been reported previously[70]; therefore, only a brief summary is provided here. The porcine acute bladder

inflammation model was modified, based on a well-developed rat bladder irritation model. Protamine sulfate solution (15mg/kg) was instilled intravesically into a female porcine bladder and retained inside for 30~45 minutes while the animal was under general anesthesia, then the instillation was curtailed and animal was freed to return to the cage. Endoscopic OCT was performed 24-48 hours after the instillation and this allowed us to examine the utility of this technique in imaging the morphological changes resulted from acute bladder irritation due to exposure to protamine sulfate. Acute responses included disruption to the urothelium or urothelial denudation and acute inflammatory lesions such as edema, vasodilatation, and sometimes acute cystitis. Although it did not induce bladder cancer growth, this bladder irritation model provided a controllable mechanism to examine endoscopic OCT technology in identifying various morphological changes associated with acute inflammation, i.e., noncancerous lesions. Prior to OCT imaging, the pig was anaesthetized with 5% inhale isoflurane for induction and 1-2.5% for maintenance, then the bladder was imaged by white-light-guided OCT inserted into a standard 22Fr endoscopic sheath. The entire imaging procedure lasted less than 30 minutes, and then the anesthesia was curtailed and the animal was freed.

Human study was performed on patients who were scheduled to undergo endoscopic procedures for bladder cancer diagnosis and treatment in the operation room and were consented for add-on endoscopic OCT. The entire OCT imaging procedure lasted less than 10 minutes. All the animal and human

studies followed the protocols approved by the IACUC and IRB committees of SUNY at Stony Brook.

6.4 Experimental results with TD-OCT endoscope ex vivo

To examine the imaging fidelity and suitability of MEMS-based OCT systems for bladder imaging, experiments were performed to compare endoscopic versus bench-top OCT systems for the porcine bladder sample *ex vivo*. In the bench-top OCT setup, the sample arm was connected to a stereoscope in which the light beam exiting the fiber was collimated to ϕ4.5mm

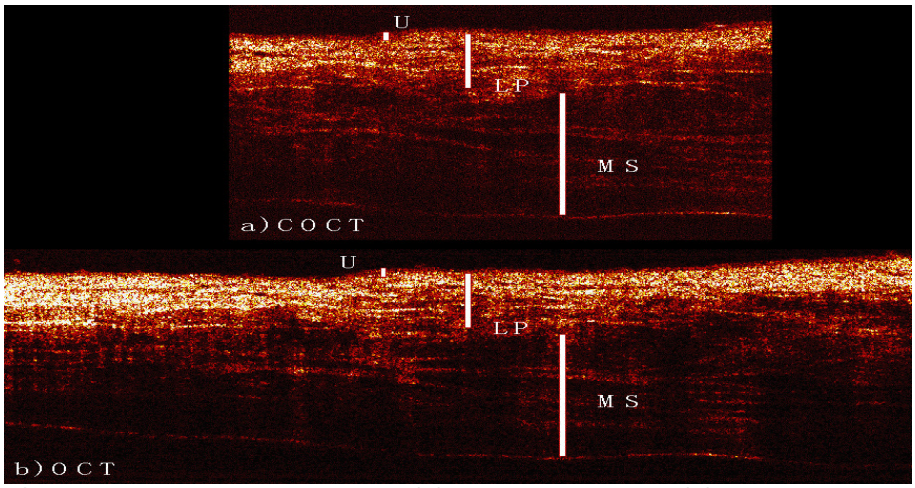

Fig.6. 5 Comparison between endoscopic OCT (a) and benchtop OCT (b). U: urothelium; LP: lamina propria; MS: muscle layer. Lateral scanning range: a). ~4mm; b). ~6mm. Axial resolution: ~10 μm.

and focused by a ϕ40mm achromatic lens, which provided comparable beam quality in the transverse direction (e.g., approximately 12μm focal spot) to that of the endoscopic OCT catheter. The transverse laser steering range is ~6mm.

Fig. 6.5 shows the comparative 2D cross-sectional OCT images of a porcine bladder taken by OCT endoscope a) versus bench-top OCT stereoscope b). The morphological details of porcine bladder such as urothelium (U), lamia propria (LP), and muscularis (MS) in A) are clearly delineated at fairly comparable image

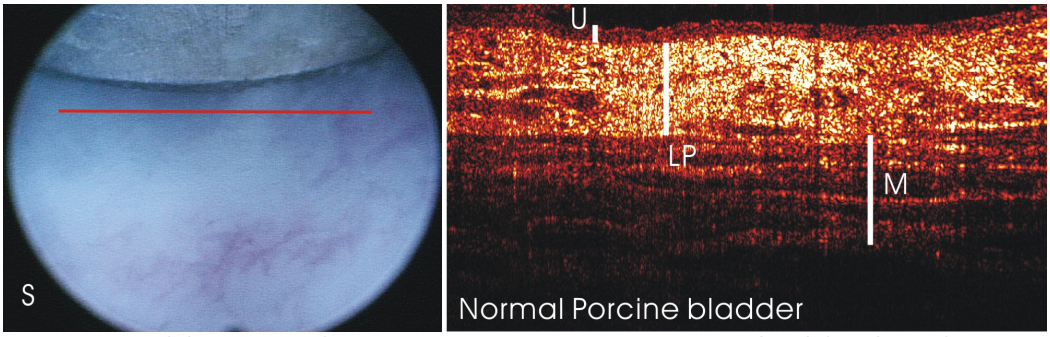

Fig.6. 6 In vivo OCT image of a normal porcine bladder taken by SD-OCT. S: surface image. OCT Image size (right panel): 4mm laterally and 2mm vertically. Morphological details of the porcine bladder, e.g., urothelium (U), lamina propria (LP), and muscularis (M) are clearly delineated based on their backscattering differences. Red line in surface images indicates OCT scanning position.

fidelity to those in B) except a slight reduction (3dB) of image SNR due to light coupling loss in the endoscope, thereby justifying the use of the MEMS-based OCT endoscope for *in vivo* image study.

6.5 Experimental results from animal study

To examine the utility of endoscopic OCT imaging systems *in vivo,* experiments have been performed in the animal study with acute inflammation porcine bladder model. Surface imaging and OCT imaging were performed at the 24 to 48 hour time points after intravesical instillation of protamine sulfate dissolved in PBS vehicle. OCT imaging was instant and was completed in less than 30 minutes (completed in 15 minutes for human studies) as required by the IACUC and IRB protocols. 2D OCT images were displayed in pseudocolour on a PC monitor for improved visual contrast and stored simultaneously with surface images for later imaging diagnosis in comparison with surface image diagnosis.

Fig.6.6 shows a 2D endoscopic OCT image of normal porcine bladder (image size: 4mm×2mm), in which the morphological details of the porcine bladder wall (a close human homologue), e.g., urothelium (U), lamina propria or submucosa

(LP), and the muscularis or smooth muscle layers (M) are clearly delineated based on their location and backscattering differences: normal urothelium is usually a thin layer with low backscattering, the lamina propria is of high scattering and the muscularis appears lower scattering than LP with large bifurcated interfaces between layers of collagen bundles.

Compared with normal porcine bladder, morphological changes pertinent to acute irritation following protamine sulfate instillation can be detected by OCT images. For instance, Fig.6.7 shows two 2D cross-sectional OCT images of bladder lesions induced by protamine sulfate instillation. Both lesions appeared reddish under white light surface imaging. Based on the resultant morphological changes imaged by *in vivo* OCT, we were able to diagnose lesion A) as urothelial

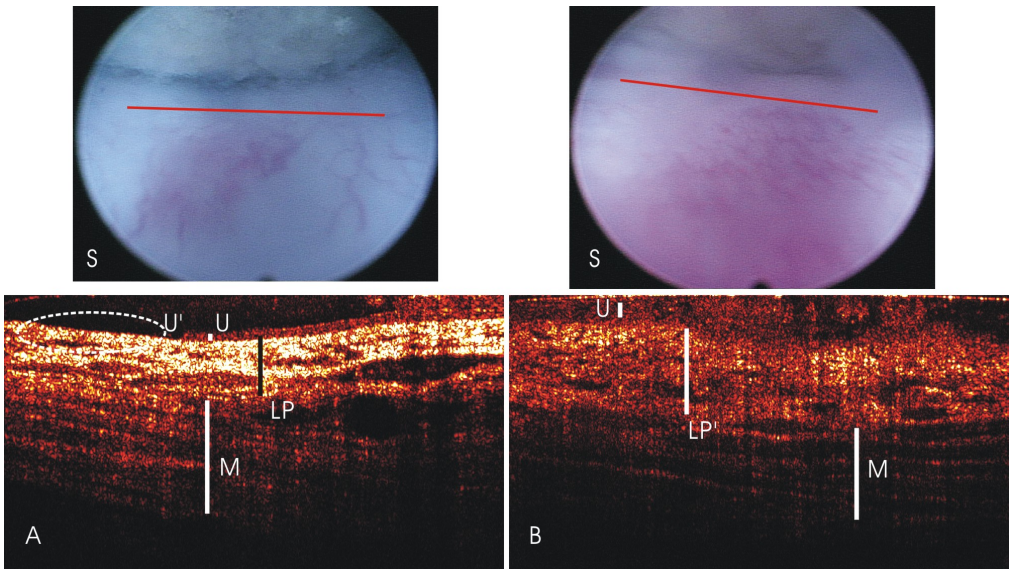

Fig.6. 7 2D cross-sectional OCT images of two bladder lesions post protamine sulfate instillation. Image size: 4mm laterally and 2mm vertically. Panel S): surface images. Panel A): urothelial denudation U' as indicated by dashed oval area. Panel B): acute inflammatory lesion with LP edema (LP') as detected by reduced scattering (fluid infiltration) in the lamina propria (as indicated by dashed circle. Normal urothelium: U, lamina propria (LP), and muscularis (M). Red line in surface images indicate OCT scanning position.

denudation and lesion B) as acute inflammatory lesion with LP infiltrate.

6.6 Results from clinical study

As this inflammatory animal model is limited to acute lesions and did not generate bladder tumors, no malignant lesions were studied. To further evaluate the MEMS-based endoscopic SDOCT system for bladder cancer diagnosis, white light guided endoscopy and OCT imaging was performed by trained physicians *in vivo* in bladder cancer patients. The preliminary result is shown below. As shown in Fig.6.8, consistent with previous porcine animal model, three basic layers, urothelium, laminar propria and muscularis were clearly differentiated from the normal bladder area, while in malignant lesions, these distinct structures were completely altered: urothelium was no longer distinguishable from lower laminar propria layer due to the increased nuclei to cytoplasm ratio of cancer cells and the resultant increased scattering within that layer.

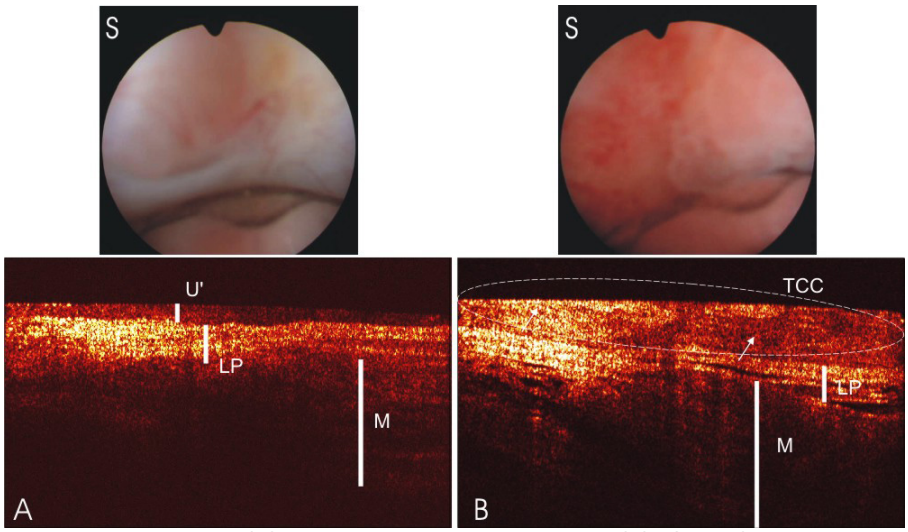

Fig.6. 8 Endoscopic OCT imaging: hyperplasia v.s. TCC. S: surface image; A: bladder with hyperplasia; B: bladder with TCC. U': urothelial hyperplasia; LP: lamina propria; M: muscle; TCC: transitional cell carcinoma.

During human *in vivo* study, it is found out that human cases are much more complicated that animal study. However, with high axial resolution, EOCT is still able to differentiate various benign lesions from malignant bladder tumors. For instance, in Fig.6.9, panel A shows OCT imaging of thickened urothelium, i.e., hyperplasia, while panel B also shows thicker urothelium, the enhanced scattering and present of micro blood vessels (indication of angiogenesis and carcinogenesis) suggest that it is malignant lesion. Until now, endoscopic OCT has been performed in more than 40 cases. Both normal and abnormal bladder surface under standard endoscope were under examination with OCT. At the same time, specimens are collected and sent for histological evaluation. The results from pathologists are used as diagnostic gold standard to evaluate the sensitivity and specificity for OCT. Based on the first 40 cases, statistics analysis shows that the sensitivity and specificity of OCT with endoscopic guidance is

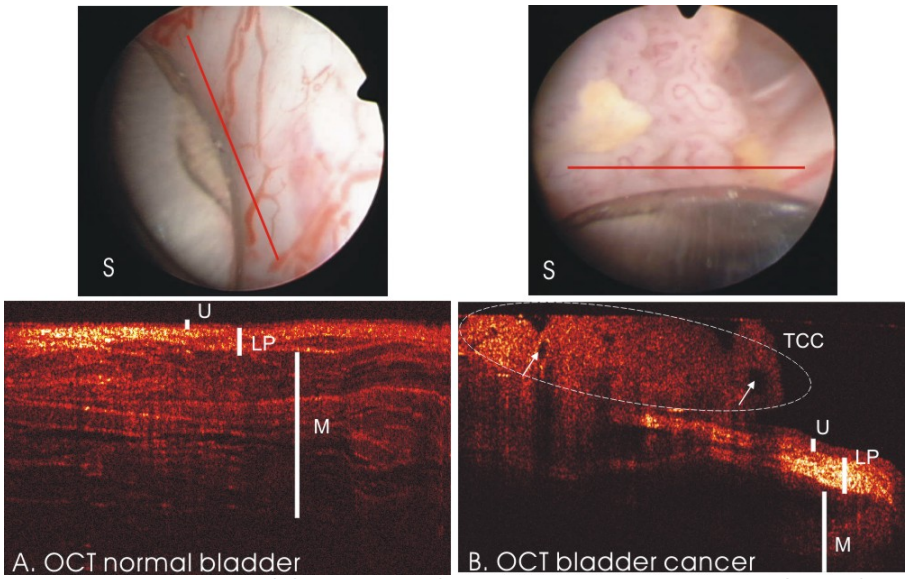

Fig.6. 9 Endoscopic OCT images from human in vivo study. S: surface imaging; A: normal bladder; B: papillary TCC. U: urothelium; LP: lamina propria; M: muscle; TCC: transitional cell carcinoma. Red lines in surface images indicate OCT scan position.

96% and 85%, respectively.

6.7 Discussions and conclusions

Among several of currently viable imaging techniques, OCT offers a great promise to noninvasive diagnosis of early bladder cancers, owing to its high spatial resolution (e.g., <10μm at current stage) and high dynamic range (>100dB) at imaging depths of 2-3mm. In recent years, there have been a number of reports on endoscopic OCT techniques, such as implementations using a rotary joint, PZT transducer, paired-angle-rotation-scanning probe and MEMS micro-mirror have been reported[13-15]; however, the development of a workable high-fidelity endoscopic OCT suitable for *in vivo* clinical imaging diagnosis remains a technical challenge.

The MEMS-based OCT endoscope presented in this chapter is of particular interest to urological applications for the following reasons: 1) the larger beam size (e.g., ≥ ϕ1.0mm) allows for improved transverse OCT resolution (e.g., ~12μm). 2) Full-range MEMS laser scanning to achieve a larger image size (e.g., >4.5mm) in the transverse direction, which has been found very useful for precise locating of the cancer boundary. 3) The front-view OCT catheter can be easily incorporated with surface imaging guidance for effective endoscopic OCT examination of larger areas such as bladder surface. This is critical, because the urologist always wants to know the surface condition and the location of the lesions under examination, and the combined surface and OCT images can eliminate some false positive diagnosis by OCT such as calcified lesions resulted from previous TURBT. 4) The unique setup that incorporates surface and OCT

scopes makes it easy to focus during *in vivo* imaging and the OCT scope is reliable, sterilizable, and cost effective.

In summary, preliminary results with significantly improved sensitivity and specificity indicate that OCT endoscopy is a very promising technique for bladder cancer diagnosis.

Chapter VII

Bladder cancer diagnosis with SD-OCT: *in vivo* study

Recent technological advances of spectral domain OCT (SDOCT) has dramatically improved the dynamic range and imaging rate[40, 71]. With optical configurations in spectral domain that circumvent the slow mechanical scanning in the reference arm, imaging rate has been improved by up to several hundred folds and potentially permits in vivo 3-D OCT imaging [41, 44, 72]. Besides, direct access of spectral interference modulation enables Fourier-domain Doppler OCT for real-time blood flow imaging[35, 49], ultrahigh-resolution FDOCT[35, 51] of retinal imaging, polarization-sensitive SDOCT[52, 53] and spectral second-harmonic generation[54] OCT to enhance image contrast in biological tissue. In addition to technological advances, clinical applications of SDOCT have been performed in various tissues to date, including eye[41], esophagus[72] and urinary bladder[56], demonstrating dramatic improvement on image fidelity and imaging rate.

This chapter discusses the recent technological advances on spectral-domain endoscopic OCT (SDEOCT) that permits faster structural imaging and simultaneous blood flow measurement of bladder in vivo. We compare the image results obtained from time-domain OCT (TDOCT) and SDOCT systems. Then, we present diagnostic results to evaluate the utility and potential limitations of SDEOCT for *in vivo* bladder imaging diagnosis based on animal and preliminary clinical studies. This part of study has been published in Journal of Biomedical

Optics in 2007[73]; the discussion that follows is drawn from the content of that paper.

7.1 Materials and methods

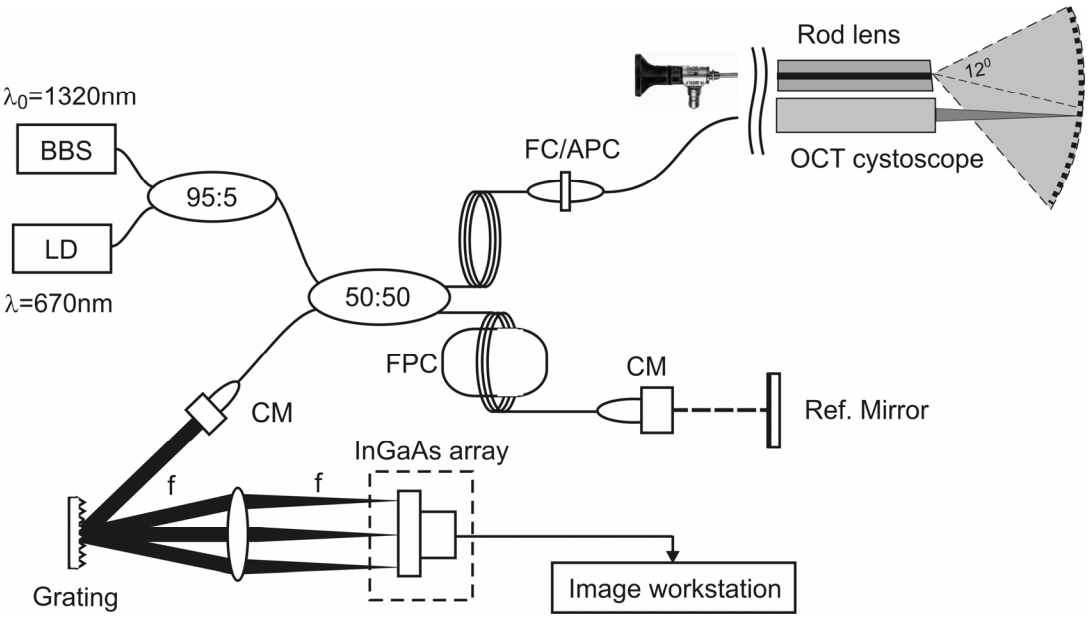

Fig.7. 1 Schematic diagram of a fiber-optic spectral-domain endoscopic optical coherence tomography (SDEOCT) system. The SDOCT system is connected to a MEMS-based OCT endoscope for *in vivo* bladder imaging study. BBS: broadband source (λ_0=1320nm, $\Delta\lambda_{FWHM}$=78nm, P=12mW); LD: aiming laser diode (λ=670nm); CM: fiberoptic collimator; FPC: fiber polarization controller. For the endoscopic setup, lateral scanning range is up to 4.5mm, and the spatial resolutions are 10 μm axially and 12 μm laterally. The single frame dynamic range of the endoscopic OCT system reached 108dB. A rod lens imaging catheter is placed parallel to OCT endoscope for image guidance.

7.1.1 MEMS-based endoscopic SDOCT

As depicted in Fig.7.1, a high-power broadband source (BBS) is employed, which can provide pigtailed output power of 12mW at central wavelength of λ=1320nm and with full-width-half-maximum spectral bandwidth of Δλ=78nm (resulting in a coherence length L_C≈10μm). The light is delivered to a fiberoptic Michelson interferometer in which light is divided equally to reference and sample arms. For visual guidance, the red light from a 670nm diode laser is

coupled into the input arm via a 95%:5% fiber coupler. In contrast to TDOCT which uses a grating-lens-based optical delay line to implement longitudinal scan, a stationary mirror is employed in the reference arm to match the optical pathlengths between the sample and the reference arms of the fiberoptic interferometer. The sample arm can be either connected to a bench-top stereoscope in which light exiting the fiber is collimated to ϕ5mm, scanned laterally by a servo mirror, and focused by an f=40mm achromatic lens onto biological tissue under examination. Through a modified FC/APC connector, it can also be connected to a MEMS-based pigtailed OCT endoscope which is inserted into the ϕ4mm instrument channel of a 22Fr commercial endoscopic sheath for in vivo animal or human study. As previously reported[13], the optical arrangement in the distal OCT scope allows visual guidance via a ϕ2.8mm scope with either white light or fluorescence image of the bladder surface. In the OCT endoscope, the light from the SM fiber is coupled by a 0.25-pitch selfoc lens to a ϕ1.0mm collimated beam, deflected by a fixed reflecting prism and a MEMS mirror, and is then focused by a laser doublet (f 10mm/ϕ5mm) onto the bladder wall for OCT scan. The transverse light scanning in the OCT endoscope is facilitated by an Al-coated CMOS-MEMS mirror which is actuated over 18^0 or 4.2mm (limited by the scope size) in the transverse direction by an applied electrical voltage or current at a repetition rate up to 100Hz.

In the detection fiber, the light beams returning from sample and reference arms are recombined and connected to a spectral radar in which light is collimated by a fiberoptic achromatic lens (f=55mm), diffracted by a holographic

grating (d=1200mm^{-1}) and then focused by an achromatic lens (f=120mm) onto a 1024-pixel line InGaAs photodiode array (Sensors Unlimited, NJ) mounted on a motored 3D stage for high-precision focusing alignment. The detected spectral graph, including spectrally encoded interference fringes from different depth within the biological sample, is amplified and then digitized and streamlined to the hard disk of an image workstation via a multi-channel 12bit A/D (DAQ6111E, NI) at 5MHz to permit 2D imaging at nearly 8fps (post image processing). Because of complex data processing (e.g., spline interpolation, FFT) involved in converting spectral graphs to a reconstructed OCT image, instantaneous image processing and display is reduced to approximately 5fps, but is sufficient for in vivo visualization of bladder wall. Data processing to reconstruct each depth profile or A-scan is implemented simultaneously with scanning of the lateral servo mirror, i.e., the MEMS mirror in the OCT endoscope following detection of each spectral graph until a 2D image is completed and displayed. Similar to TDEOCT, the axial and the transverse resolutions of SDEOCT are determined by the coherence length L_c and the focal spot size of the OCT scope, respectively. Based on the above parameters used in our setup, the axial resolution is ~10μm, and the transverse resolution is ~12μm.

In terms of SDOCT vs. TDOCT, of particular interest is the ability of SDOCT to simultaneously image tissue architecture and subsurface blood flow/velocity (i.e., Doppler SDOCT) in nearly real time, which can be readily extracted from differential spectrograph data (i.e., phase difference) with minimal hardware modification[35]. Doppler OCT imaging can provide very useful

functional blood flow information pertinent to bladder cancer because abnormal angiogenesis underneath the bladder surface can be induced by bladder tumorigenesis. For instance, cancer cells can induce abnormal angiogenesis once the tumor size is greater than 1–2 mm in diameter[74], and when the fresh nutrients and oxygen are rapidly depleted and new blood vessel formation is necessary to replenish them [75]. Thus detecting abnormal angiogenesis within bladder wall can provide additional diagnostic information for bladder cancers, thereby improving diagnostic sensitivity and specificity. As previously reported[35], subsurface Doppler flow image can be acquired by subtraction of multiple (N) A-scans at each lateral position. In addition to the amplitude term $I(z) = |\tilde{I}(z)|$ of the inverse complex Fourier transform $\tilde{I}(z) = iFFT\{I(k)\}$ that constitutes the structural SDOCT image, the phase term $\Phi(z,\tau) = \tan^{-1}(\mathrm{Im}(\tilde{I}(z))/\mathrm{Re}(\tilde{I}(z))$ is extracted. And the phase variation between two adjacent A-scans at the same lateral position $\Delta\Phi(z, \tau)$ is used to reconstruct the Doppler flow velocity $v(z) = \Delta\Phi(z,\tau)\lambda/(4\pi\tau\cos(\alpha))$ [35], where τ is the interval between two A-scans. The excessive phase noise that imposes a major limitation to the dynamic range of Doppler OCT can be improved by implementing multiple scans and averaging $\Delta\Phi(z, \tau)$[76]. The major advantages of such technique for *in vivo* Doppler imaging are obvious: it does not require hardware modification and imaging can be much faster to reduce the influence of motion artifacts.

7.1.2 Animal model for *in vivo* SDEOCT study

The animal model employed in this study has been reported previously[56]; therefore, only a brief summary is provided here. Because of lack

of large animal bladder cancer model suitable for testing OCT endoscopes for in vivo imaging, the porcine acute bladder inflammation model was modified, based on a well-developed rat bladder irritation model. Protamine sulfate solution (15mg/kg) was instilled intravesically into a female porcine bladder and retained inside for 30~45 minutes while the animal was under general anesthesia, then the instillation was curtailed and animal was freed to return to the cage. Endoscopic OCT was performed 24-48 hours after the instillation, allowing us to examine the utility of this technique in imaging the morphological changes resulted from acute bladder irritation due to exposure to protamine sulfate. Acute responses included disruption to the urothelium or urothelial denudation and acute inflammatory lesions such as edema, vasodilatation, and sometimes acute cystitis. Although it did not induce bladder cancer growth, this bladder irritation model provided a controllable mechanism to examine endoscopic OCT technology in identifying various morphological changes associated with acute inflammation, i.e., noncancerous lesions. Prior to OCT imaging, the pig was anaesthetized with 5% inhale isoflurane for induction and 1-2.5% for maintenance, then the bladder was imaged by white-light-guided OCT inserted into a standard 22Fr endoscopic sheath. The entire imaging procedure lasted less than 30 minutes, and then the anesthesia was curtailed and the animal was freed. Human study was performed on patients who were scheduled to undergo endoscopic procedures for bladder cancer diagnosis and treatment in the operation room and were consented for add-on endoscopic OCT, and the entire OCT imaging procedure lasted less than 10 minutes. All the animal and human

studies followed the protocols approved by the IACUC and IRB committees of SUNY at Stony Brook.

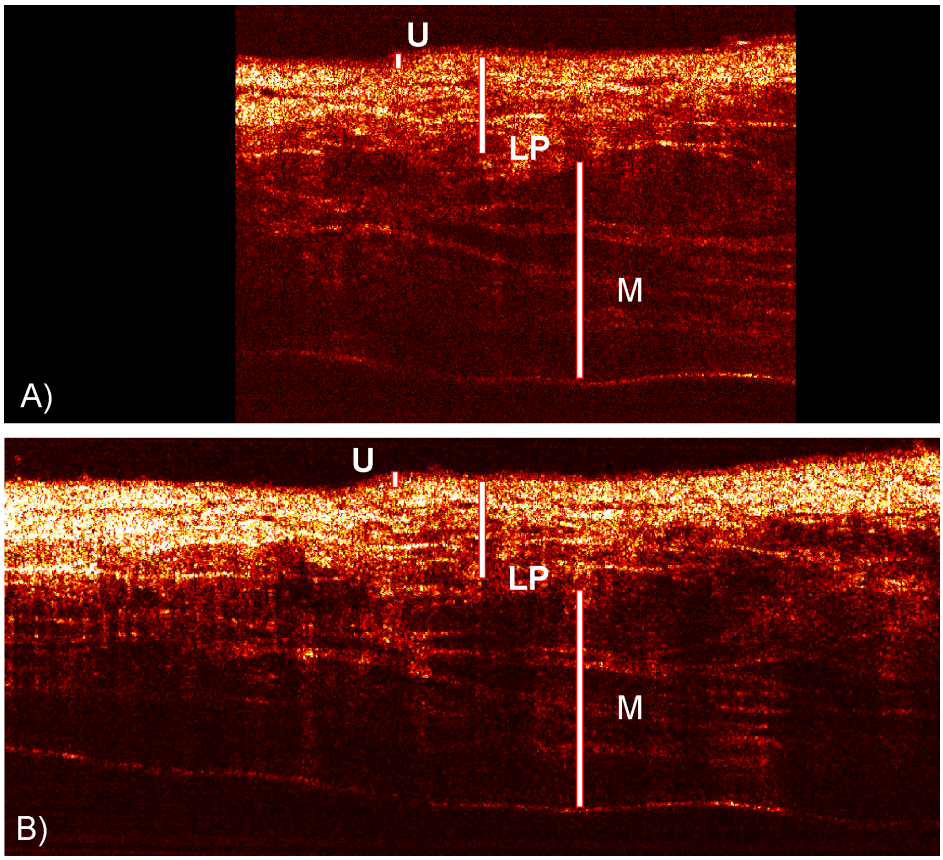

Fig.7. 2 Comparison between endoscopic OCT image and bench-top OCT image of a fresh porcine bladder. A). endoscopic OCT image; B). bench-top OCT image. U: urothelium; LP: lamina propria; M: muscularis. Image size: A) 2mm axially × 4.2mm laterally; B) 2mm axially × 6mm laterally. Due to light coupling loss in the endoscope, there is a slight SNR reduction (~2.87dB) in image A).

7.2 Results

To examine the imaging fidelity and suitability of MEMS-based OCT systems for *in vivo* bladder imaging, we performed experiments to compare endoscopic vs. bench-top OCT systems and endoscopic SDOCT vs. TDOCT systems. The axial resolution of the bench-top OCT setup that employed a ϕ4.5mm beam collimator and a f/40mm achromatic lens was approximately

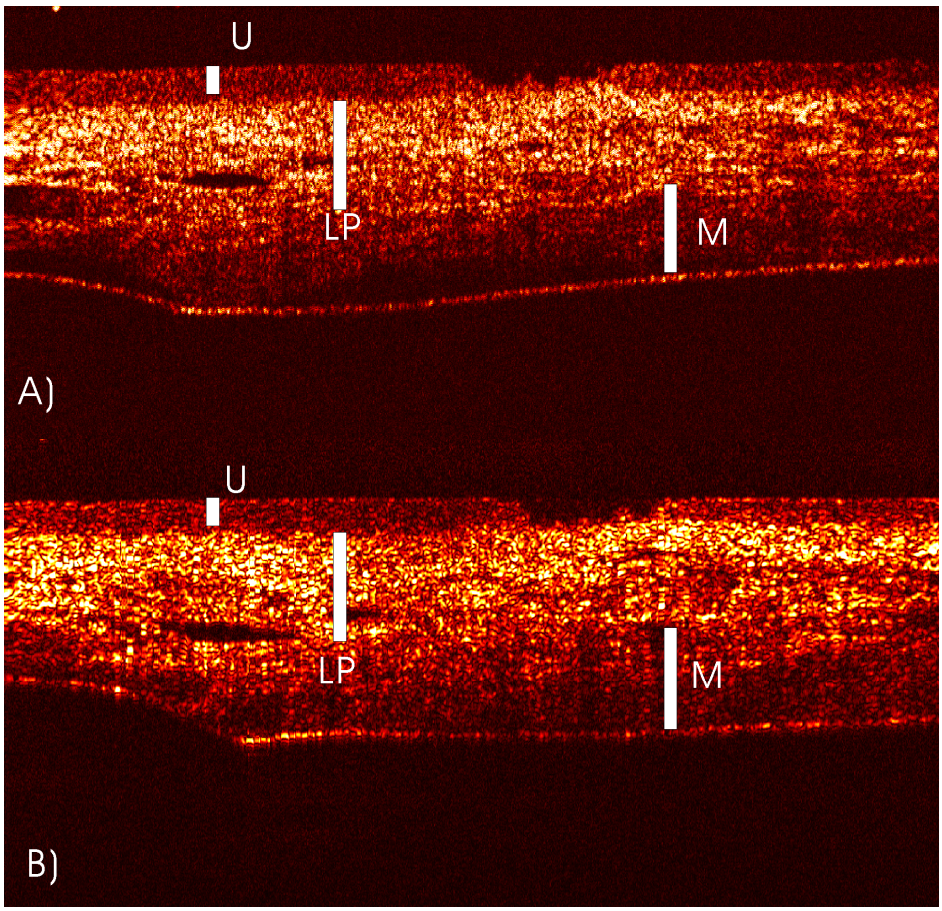

Fig.7. 3 Comparison between TDOCT and SDOCT endoscopic bladder images. A). endoscopic TDOCT image; B). endoscopic SDOCT image. U: urothelium; LP: lamina propria; M: muscularis. Image size: 2mm axially × 4.2mm laterally. SDOCT (B) shows 2.5dB enhanced image SNR than TDOCT (A) at ~6 times faster frame rate.

ϕ12μm, equivalent to that of the MEMS-based endoscopic OCT catheter with a ϕ1mm beam collimator and a f/10mm achromatic lens. But the transverse laser steering range of OCT catheter was limited (<4.6mm) by the scope size and was smaller than that of the bench- top setup (6mm).

Fig.7.2 shows the comparative 2D cross-sectional OCT images of a porcine bladder taken by OCT endoscope A) versus bench-top OCT stereoscope B). The morphological details of porcine bladder (a close mammalian

homologue) such as urothelium (U), lamina propria (LP), and muscularis (M) in A) were clearly delineated at fairly comparable image fidelity to those in B) except a slight reduction (2.87dB) of image SNR due to light coupling loss in the endoscope. The result demonstrates the drastic improvement on our implementation of MEMS-based OCT catheter and justifies the utilities of *in vivo* bladder imaging study.

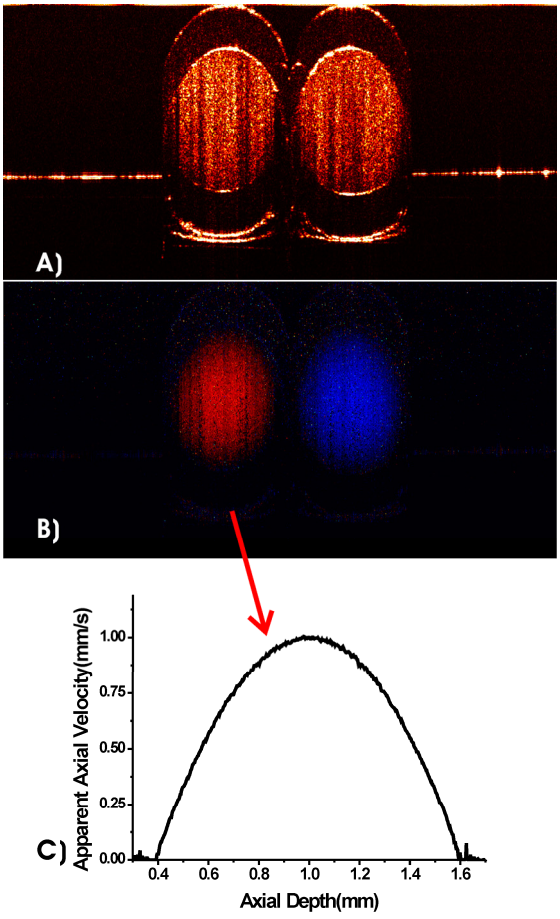

Fig.7. 4 2D Doppler OCT of bidirectional flows of intralipid solution. A) Structural image; B) Flow image; C) Depth-dependent mean flow rate. Using parabolic curve fitting, the measured apparent volumetric velocity is ~3.1ml/h, which is consistent with experimental flow set of 3.0ml/h (the slant angle was 20° and the camera frame rate 7.7 kHz).

Fig.7.3 shows the comparison between TDOCT and SDOCT endoscopic images. Both OCT images delineate the bladder morphology, e.g., U, LP, and M; however, a quantitative analysis between these two images indicates that at almost 6-fold improved imaging rate, SDOCT (panel B) still shows 2.5dB enhanced image SNR than TDOCT (panel A). Therefore, SDOCT offers benefits in both image fidelity and imaging speed for endoscopic *in vivo* imaging study.

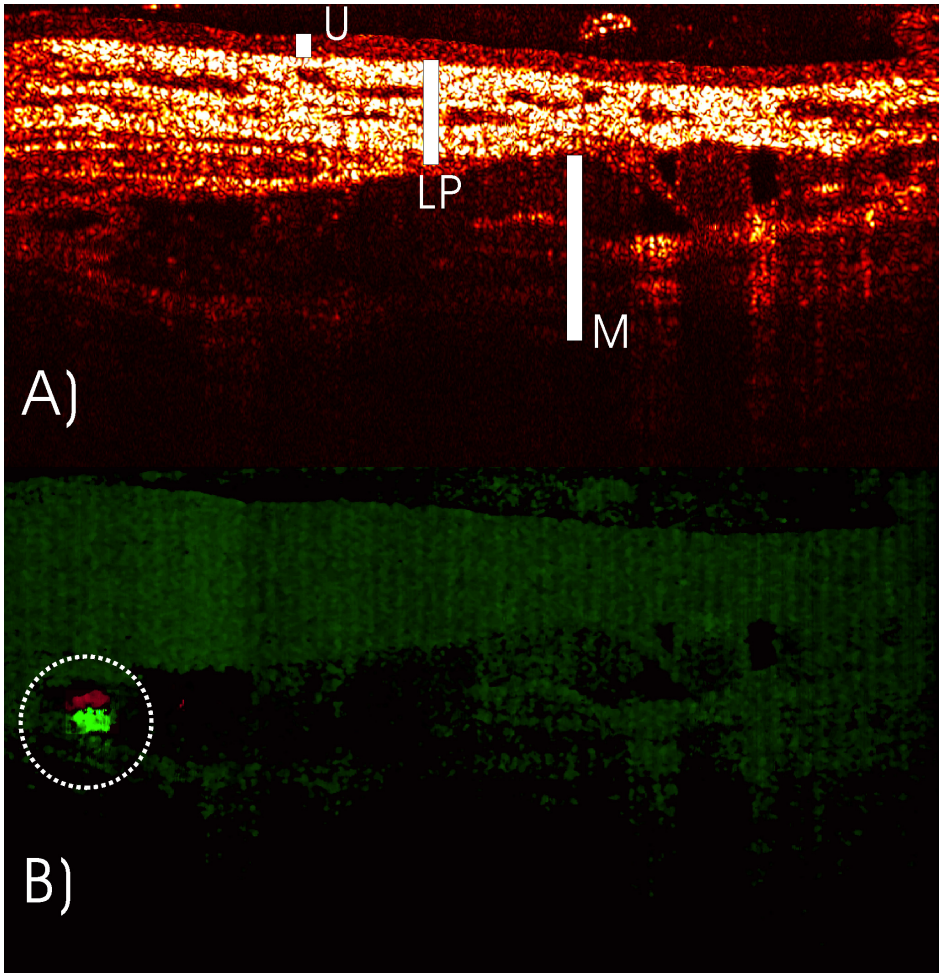

Fig.7. 5Doppler SDEOCT of subsurface blood flow in a porcine bladder *in vivo*. U: urothelium; LP: lamina propria; M: muscularis. Image size: 2mm axially × 4.2mm laterally. Two minute blood flows (roughly ϕ180um) were detected in the lamina propria (about 800μm underneath the bladder surface). The estimated apparent flow rates were 0.51mm/s and 0.13 mm/s, respectively.

More importantly, SDOCT can provide simultaneous Doppler image to map subsurface blood flow distribution. For instance, Fig.7.4 shows the result of calibration study using tissue phantom in which the profile of two bidirectional flows (1% intralipid solution, $\mu_s \approx 2.4 cm^{-1}$) in a ϕ0.56mm translucent conduit can be quantitatively imaged by SDOCT. Based on the calibration result, Fig.7.5 shows the result of *in vivo* porcine bladder study in which two minute blood flows (roughly ϕ150um) in the lamina propria (about 800μm underneath the bladder surface) were detectable as indicated by the dashed circles with estimated apparent flow rate of 0.51mm/s and 0.13 mm/s. It was observed during the experiment that the phase noise induced by bladder movement and handshaking compromised the dynamic range of *in vivo* blood flow imaging. Currently, we are implementing interpixel-shifted SDOCT[77] to increase imaging rate (while maintaining imaging depth) and thus to minimize the influence of motion artifacts on Doppler OCT *in vivo*.

Following successful *in vivo* porcine bladder imaging study, we initiated *in vivo* clinical study on symptomatic patients scheduled for operation-room examinations and treatments such as endoscopy with possible biopsies, transurethral resection of bladder tumors (TURBT), and cystectomy. As a blind study to examine the diagnostic sensitivity and specificity of OCT endoscopy, the OCT diagnosis was given during the endoscopic procedure, and was later validated by the result of biopsied histology which served as gold standard of clinical diagnosis. As exemplified in Fig.7.6 are the results of a normal human bladder in which panel A) is surface image *in vivo*, panel B) is endoscopic OCT

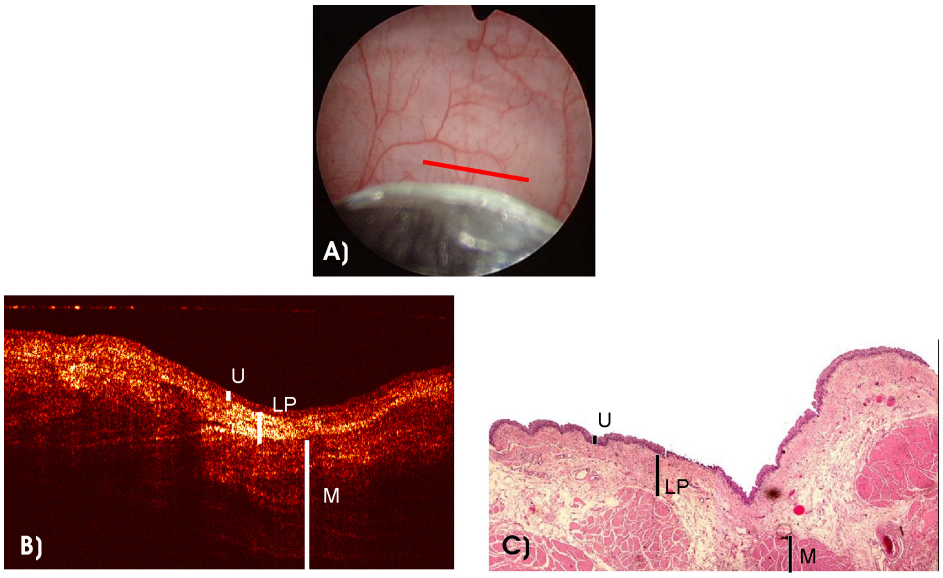

Fig.7. 6Endoscopic OCT image of a normal human bladder *in vivo*. A) Surface image, B) Endoscopic OCT image, C) H&E stained histological section. U: urothelium; LP: lamina propria; M: muscularis. Image sizes for panel A) and panel B) are ϕ12mm and 2mm axially × 4.2 mm laterally, respectively. The red line in panel A) indicates the lateral position of the OCT scan.

image *in vivo*, and panel C) is the corresponding H&E stained histological section from the biopsied specimen.

As can be seen, white light endoscopic image, with field of view of approximately ϕ12mm, appears flat and uniform with plenty of visible subsurface blood vessels. Both endoscopic OCT and histological sections are 4.2mm in the transverse direction and 2mm in the vertical direction. It is obvious to see that human bladder bears a close similarity to porcine bladder (Fig.7.2) in terms of the anatomic architecture and optical properties such as scattering and absorption. The morphological details of normal human bladder delineated by OCT, e.g., the low scattering urothelium U, high-scattering lamina propria LP, and the upper muscularis M, correlated well with the those in the histological section. For instance, the *in vivo* OCT measurement of urothelial thickness of d_U=67.9$\pm$5.6μm

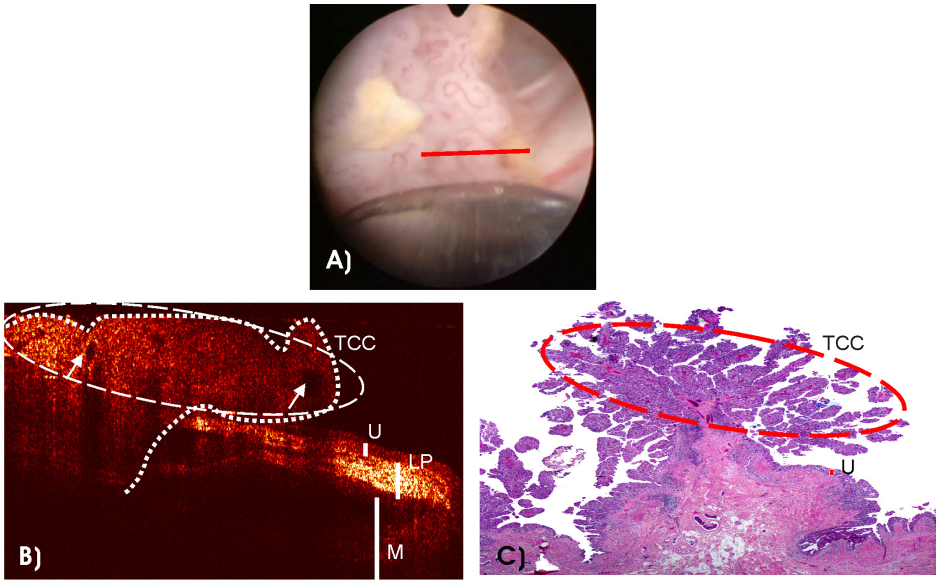

Fig.7. 7 Endoscopic OCT image of a human bladder cancer *in vivo*. A) Surface image, B) Endoscopic OCT image, C) H&E stained histological section. U: urothelium; LP: lamina propria; M: muscularis. Image size: 2mm axially × 4.2 mm laterally. Image sizes for panel A) and panel B) are ϕ12mm and 2mm axially × 4.2 mm laterally, respectively. The red line in panel A) indicates the OCT scanning position. Endoscopic OCT image clearly provides the margin between the tumor and the adjacent normal bladder wall, as indicated by the dash curve. The lesion shown is papillary transitional cell carcinoma (TCC, low grade I/III, stage T2).

matches the histological evaluation of d_U=62.8 ±4.1μm, which appears as a homogeneous, low-scattering thin layer.

In addition to normal bladder, Fig.7.7 shows the result of a bladder tumor including the transition to the adjacent normal bladder. The papillary appearance of the lesion is apparent under the endoscopic surface RGB image as seen in panel A). OCT in panel B) diagnoses the lesion as papillary TCC and clearly provides the margin between the tumor and the adjacent normal bladder wall. Unlike normal bladder in Fig.7.6, the distinct morphological structures such as U, SM, and M were drastically changed: the urothelium was no longer distinguishable from underlying laminar propria due to carcinogenesis in the

urothelium and the resultant increase in scattering properties and homogeneity. Here, the OCT diagnosis of this TCC was based on identifying papillary features of the lesion such as the dark holes as highlighted by arrows in the thickened cancerous urothelium. Histology in panel C) confirms the lesion as a papillary TCC (low grade I/III, stage T2). It must be noted that although OCT can mark the boundary of the papillary lesion as highlighted by the dashed line, it may not always be able to stage the invasion of cancer (e.g., >T2a) because of signal loss in the cancerous region. High attenuation of OCT signal in cancerous lesions can be attributed by light loss due to increased in homogeneity (such as papillary features) and enhanced subsurface vascularization.

7.3 Discussions

In summary, we report the technical improvement of MEMS-based OCT endoscope to enable high-resolution imaging of bladder morphology (e.g., urothelium, lamina propria, and upper muscularis) and function (e.g., subsurface blood flows) noninvasively, and the preliminary results of *in vivo* clinical diagnosis of transitional cell cancers. To examine the utility of endoscopic OCT for *in vivo* imaging and diagnosis of bladder morphology, functions, and malformations (e.g., TCCs), we proposed a protocol that incorporated conventional endoscopy, endoscopic OCT, and excisional biopsy to compare the diagnostic results for each lesion, in which histological evaluation of the biopsied lesion specimens served as gold standard for clinical diagnoses. As the bladder surface images in Fig.7.6(A) and Fig.7.7(A) indicate, conventional endoscopy is based on visual inspection of gross topological (i.e., superficial) changes of the bladder to

diagnose bladder tumors. Therefore, it can efficiently locate and diagnose highly papillary TCCs as exemplified by Fig.7.7. However, because of inability to resolve in depth direction, it is common that endoscopy may fail to distinguish benign bladder inflammatory lesions from early flat TCCs such as carcinomas *in situ*, both of which may show a normal or slightly reddish surface appearance[78, 79]. Therefore, improved endoscopic imaging techniques are needed that will permit high-resolution visualization of morphological details below the bladder surface to diagnose early flat TCCs and to stage cancer invasion. Among several of currently viable imaging techniques, OCT offers a great promise to noninvasive diagnosis of early bladder cancers, owing to its high spatial resolution (e.g., <10μm at current stage) and high dynamic range (>100dB) at imaging depths of 2-3mm. Based on previous animal bladder carcinogenesis studies, the unique cross-sectional imaging fashion of OCT - that is analog to histopathology - allows the urologist to visualize the morphological architectures of the bladder critical to early caner diagnosis such as the urothelium, the lamina propria and the upper muscularis noninvasively, instantaneously, and at sub-10um resolution close to histopathology, if implemented endoscopically.

As shown in Fig.7.6, the morphological details of a normal human bladder are clearly delineated. In contrast to normal bladder, the contrast and structural details in cancerous lesions as exemplified in Fig.7.7 are drastically reduced or diminished and the effective imaging depth is decreased. Because of this, the use of endoscopic OCT for staging cancer invasion is likely to be limited to stages T1 or T2a (i.e., prior to muscle invasion). Previous systemic *ex vivo* rat

bladder carcinogenesis studies revealed that OCT differentiated TCC from normal bladder and benign lesions such as inflammatory lesions and hyperplasia by detecting enhanced urothelial backscattering as a result of increased nuclear-to-cytoplasmic ratio in TCCs. However, it has been found that some human TCCs may also show no obvious increase in backscattering such as the lesions in Fig.7.7. More detailed human data and analysis are required to study the relation between urothelial backscattering enhancement and cancer grading and staging. Fortunately, hyperplasia is far less common in human cases than in the animal carcinogenesis model following MNU installation, the estimated diagnostic sensitivity and specificity based on initial human cases (20 cases so far) are over 91% and 80%, respectively. Currently, the identification of TCCs is based on abnormal changes in the urothelium such as the papillary features of TCCs as exemplified in Fig.7.7(B). Based on more human data analysis and classification, potential future approaches to further improve OCT diagnosis of human TCCs *in vivo* will include detection of local vascularization with endoscopic Doppler OCT, quantification of urothelial backscattering for TCC grading, and endoscopic ultrahigh-resolution OCT for quantification of nuclear-to-cytoplasmic ratio. The initial results of endoscopic Doppler OCT as shown in Fig.7.5 are of great interest for future detection of elevated tumor vasculature. However, we have noticed that due to phase noise induced in *in vivo* imaging the dynamic range for small flow mapping is compromised. We are addressing the issue by employing common path optical topology[80, 81] to minimize the phase drift caused by motion artifacts induced by patient or the examining physician.

7.4 Conclusions

In summary, a spectral-domain endoscopic OCT imaging system is presented and its utility in bladder cancer diagnosis is examined *in vivo* based on porcine data and initial clinical trial. Preliminary results demonstrate the potential of MEMS-based SDEOCT for providing the morphological details of porcine and human bladders such as the urothelium, the lamina propria and the upper muscularis at the resolution and contrast comparable to TDEOCT and even the bench-top OCT system. The SDEOCT imaging system can provide cross sectional OCT images of 2mm in the depth direction and 4.5mm in the transverse direction per scan at a frame rate of approximately 8 fps. The imaging system is fully automatic, and incorporated with surface endoscope for visual guidance and complimentary diagnosis with OCT scope. Additional *in vivo* results of blood flows in the lamina propria of bladder and clinical diagnosis of human TCCs are presented, suggesting that MEMS-based SDEOCT is a very promising optical biopsy technique for noninvasive and instantaneous imaging diagnosis bladder diseases such as early diagnosis of bladder cancers.

Chapter VIII

Doppler OCT for angiogenesis detection

So far, the diagnostic mechanism of OCT for bladder cancer detection has been mainly based on the hypotheses that bladder cancer cells will show enhanced urothelial backscattering due to increased nuclei-to-cytoplasmic ratio and cell density, loss of morphological structures (e.g., urothelium, lamina propria and upper muscularis), and enhanced urothelial inhomogeneity (such as those in papillary TCCs). These hypotheses are proposed based on our theoretical modeling (Chapter 2.6) and successful *ex vivo* carcinogenesis studies using a standard rat bladder tumor model. For instance, previous systematic study of fluorescence guided OCT technique has achieved exciting results with sensitivity and specificity of 100% and 93%, respectively (Chapter 5.2). However, recent results of our *in vivo* human study suggest that clinical cases are much more complicated than ex vivo animal study; a significant portion of low-grade bladder cancers actually show reduced scattering when examined with OCT cystoscope, making it more difficult to differentiate them from benign lesions, such as inflammatory lesions.

Additional contrast mechanism is desirable to further improve OCT diagnostic efficacy in clinical settings. We incorporated Doppler technique with our OCT endoscopy and proposed to visualize subsurface blood flow in the bladder wall in vivo, which provides a contrast mechanism more specific to carcinogenesis. As mentioned previously, a minor modification of SDOCT may

permit not only morphological image (amplitude), but also subsurface vasculature within the bladder wall and blood flow rate in the same field of view by extracting the phase change of the spectral interferograms. We hypothesize that this capability can enable Doppler OCT to identify abnormal angiogenic changes associated with bladder carcinogenesis such as increased blood circulation, thereby potentially improve the diagnostic sensitivity and specificity for endoscopic OCT technique if combined with structural OCT image.

8.1 Cancer angiogenesis

Angiogenesis is the process of formation of new blood vessels in biological tissue. It has been known that cancer cells can induce abnormal angiogenesis to replenish the rapid depletion of fresh nutrients and oxygen as a result of excessive tumor growth[74]. Therefore, combined with structural OCT imaging, detection of angiogenesis with Doppler OCT can potentially improve the diagnosis of bladder cancers.

8.2 Doppler shift

The Doppler shift refers to the apparent frequency change of light waves when measured by a moving observer relative to the source of the wave. In the OCT scenario, the scattering centers such as red blood cells that move at a velocity of v and in the direction θ towards the incident light propagation will produce a Doppler shift,

$$f_D = 2v\cos\theta/\lambda \tag{8.1}$$

where λ is the light wavelength and $2v\cos\theta$ is the round-trip velocity projected along the direction of the incident light propagation.

8.3 Time domain Doppler OCT (TD-ODT)

In a TD-OCT system, the overall Doppler frequency shift f_0 is in fact the summation of those in sample and reference arms as previously given by Eq.(2.12) as,

$$\mathrm{I} = I_R + I_S + 2\sqrt{I_R I_S}\, e^{\left(-\frac{4\ln 2 t^2}{\tau^2}\right)} \cos[2\pi f_0 t] \tag{8.2}$$

where $f_0=(k_0/2\pi)\partial(\Delta L)/\partial t=(\upsilon_R-\upsilon_S)/\lambda_0$ is the carrier frequency of the signal processing electronics for heterodyne detection. υ_R is introduced by the optical delay line and υ_S is the Doppler shift induced by the flow in the sample arm. For most subsurface small blood flow, υ_S≤5-10mm/s. However, υ_R≥1.5×10^{3}mm/s is required to facilitate near real-time OCT (e.g., at an A-scan depth of 3mm at 500Hz). In order words, υ_S/υ_R≈5×10^{-2} and considering the instability of υ_R due to mechanical scanning, direct measurement of υ_S based on $\upsilon_S=\upsilon_R-f_0\lambda_0$ gives very poor sensitivity, if it is not impossible.

In late 1990, an interesting technique was reported to tackle this challenge in high-speed Doppler OCT required for in vivo study [82, 83]. Instead of extracting flow-induced Doppler frequency shift $f_D=\upsilon_S/\lambda_0$ within A-scan, the phase difference $\Delta\phi$(x,z) between two sequential A-scans is used to extract the Doppler frequency shift $f_D=\Delta\phi$(x,z)/T where T is the time interval between two A-scans. To extract $\Delta\phi$(x,z), short-time window FFT is needed to calculate the centroid frequency and high-speed A/D is required to acquire the undemodulated OCT signal sequence or A-scans [84]. However, this technique is computation

intensive and thus compromises the frame rate, spatial resolution and flow sensitivity [34].

8.4 Spectral domain Doppler OCT (SD-ODT)

According to Eq.(2.13) the measured interference spectrograph in the presence of flow can be expressed as,

$$I \infty S(k) + S(k)\cos(2k\Delta L) \tag{8.3}$$

but ΔL changes to $\Delta L = l_R - l_S = \Delta L_0 - v_S t$ where $\Delta L_0 = l_R - l_{S0}$ and v_S is the flow velocity, i.e.,

$$I \infty S(k) + S(k)\cos(2k\Delta L_0 - 2k_0 v_S t) \tag{8.4}$$

As discussed above, $v_S t << \Delta L_0$, Eq.(8.4) implies that although the flow does not affect the structural image which is determined by ΔL_0 and $S(k)$, it affects the phase change $\Delta\varphi = -2k_0 v_S t$. Similar to TDODT, the flow rate can be acquired by retrieving the phase shift over two adjacent A-scans at the same lateral position,

$$\upsilon_S(x,t) = \frac{1}{2k_0}\frac{\partial\varphi(x,z)}{\partial t} = \frac{\lambda_0}{4\pi}\frac{\Delta\varphi(x,z)}{\Delta t} \tag{8.5}$$

where $\Delta\varphi$ is the phase change within $\Delta t = T$ is the minimum time interval for A scan. As $|\Delta\varphi|_{max} = \pi$ for bi-directional flow measurement, the maximum flow velocity that can be measured is $v_{Smax} = \lambda_0 / 4T$. For instance, $v_{Smax} \approx 2.54 mm/s$ for our current system with λ_0 =1320nm and T$=1/7700$s (i.e., at frame rate of 7.7fps).

8.5 Doppler OCT for bladder cancer diagnosis

Our current endoscopic SDOCT system was adopted accordingly for in vivo blood flow measurement within the bladder wall. In the following sections, I will present the system setup and preliminary results for proof of concept. I will also discuss the usefulness and limitations of the current system for in vivo study.

Fig.8.1 depicts the schematic diagram of the experimental SDODT setup which is essentially the same as our current SDOCT system. The light source employed is a high-brightness broadband source (BBS) with pigtailed output power of 13mW, central wavelength at λ=1320nm and spectral bandwidth of ∆λ=78nm. A stationary reference mirror is employed to replace the grating-lens-based optical delay line in TDOCT. For bench-top study, the light beam exiting the SM fiber of the sample arm is collimated to ϕ5mm, scanned laterally by a servo mirror and then focused onto the specimen by an achromatic doublet with focal length of f=40mm. For endoscopic study, the sample arm will be connected to a MEMS-based OCT catheter.

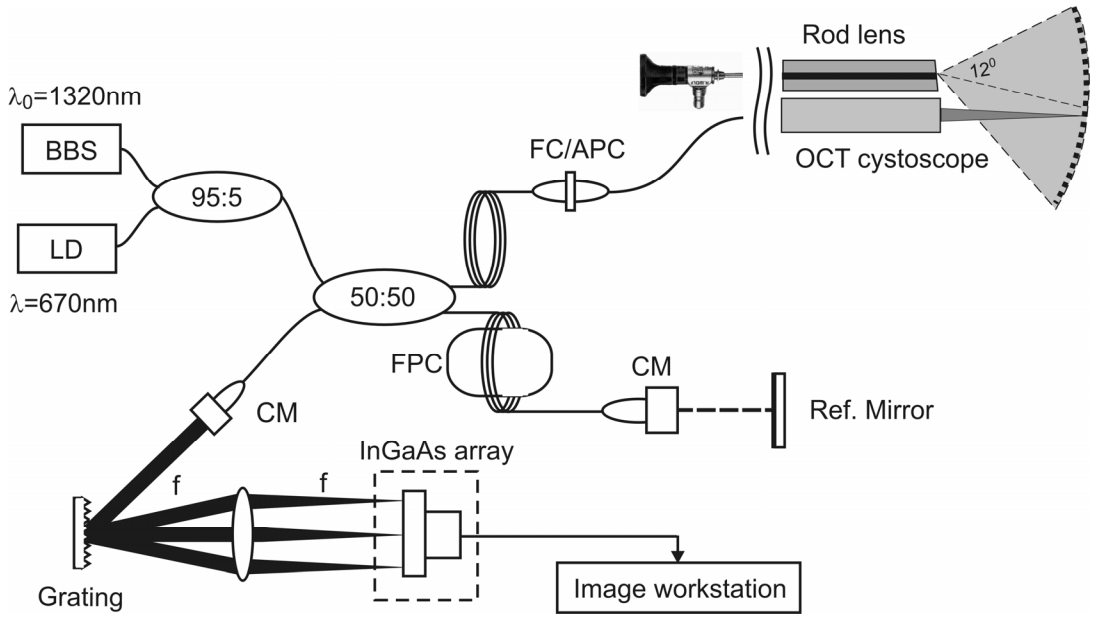

Fig.8. 1 Schematic diagram of a fiber-optic spectral-domain endoscopic optical coherence tomography (SDEOCT) system. The SDOCT system is connected to a MEMS-based OCT endoscope for *in vivo* bladder imaging study. BBS: broadband source (λ_0=1320nm, $\Delta\lambda_{FWHM}$=78nm, P=12mW); LD: aiming laser diode (λ=670nm); CM: fiberoptic collimator; FPC: fiber polarization controller. For the endoscopic setup, lateral scanning range is up to 4.5mm, and the spatial resolutions are 10 μm axially and 12 μm laterally. The single frame dynamic range of the endoscopic OCT system reached 108dB. A rod lens imaging catheter is placed parallel to OCT endoscope for image guidance

The combined light beams from both reference and sample arms are collimated, diffracted by a holographic grating and focused by an achromatic lens onto an InGaAs line scan camera (Sensorsunlimited, NJ). The spectrally resolved interference signal detected by the diode array is digitized using a high speed A/D converter (DAQ6111E, National Instrument), stored and processed on the PC (Precision 670, Dell Inc., Texas). The line scan camera can operate up to 7.7k A-scan/s that leads to a maximum measurable apparent velocity of 2.5mm/s according to Eq.(8.5) [35].

8.6 Previous problems

The spectral OCT system provides higher imaging rate and enhanced dynamic range, which greatly facilitates in vivo study. However, during our experiments there still remain many technical problems, especially for Doppler flow measurement. For instance, direct phase difference calculation by subtraction is susceptible to calculation noise, which degrades the image contrast and diagnostic sensitivity. Fig.8.2 shows SD-OCT measurements of a normal porcine bladder in vivo with our endoscope. Panel A) is the structure image while panel B) and C) are both flow images reconstructed with different

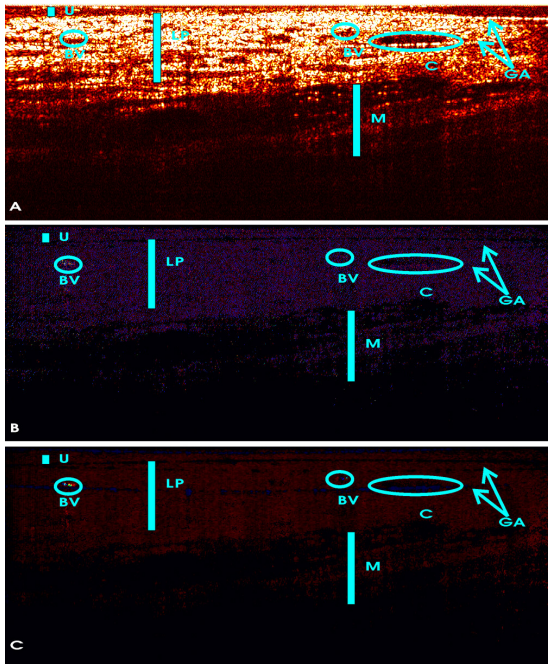

Fig.8. 2 Previous problem for spectral domain Doppler OCT. A) structure image; B) flow image with phase subtraction algorithm; C) flow image with Kasai velocity estimator. U: urothelium; LP: lamina propia; M: muscle layer; BV: blood vessel; C: cystitis; GA: glass artifacts. Image size: 4mm x 2mm laterally and axially.

algorithms. The flow image acquired by phase subtraction (panel B) barely shows the blood vessel on the left, while there are two present in lamina propria (as circled). It is noticed that the background is very noisy because for each phase difference two angles are calculated. Each calculation is susceptible to speckle noise and phase wrapping (phase range [-π, π]).

Another minor but non-trivial problem is the mirror image caused by image reconstruction algorithm (i.e. Fourier transform). As discussed in Chapter IV, the signal to noise ratio (SNR) degrades with increased path length mismatch. To optimize the field of view and obtain better image quality, the reference needs to be carefully positioned so that the glass window occupies as little space as possible. Meanwhile, in clinical scenario, the path length mismatch constantly varies due to the polarization effect. With mismatched path length, this could introduce artifacts for both structure image and Doppler flow image (Fig.8.2), which in turn compromises diagnostic efficiency. As shown in Fig.8.2, the mirror

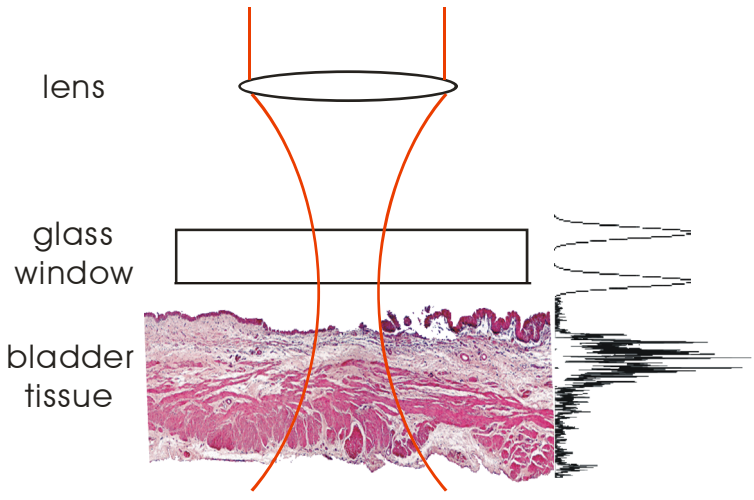

Fig.8. 3 Common path SDOCT.

image of the glass window at the tip of the endoscope overlaps with the bladder image. For Doppler image, two circled areas (BV) show real blood flow while the third (C) Doppler signal is actually artifact caused by the glass window.

To solve this problem, we have proposed a common path setup (Fig.8.3). One particular advantage of SDOCT technique is that because reference mirror scanning is circumvented, it is possible for the reference and sample arms to share the same optical fiber to eliminate the phase noise induced by the fiber motion. However, after several trials, we found that this optical design is not practical due to the non-flatness of the laser doublet focal plane which causes non-uniform reference intensity (Fig.8.4). Consequently, the field of view of the endoscope is reduced by more than 50%. With achievable 2.0 mm or less scanning range, the advantage of MEMS-mirror based endoscopy is compromised.

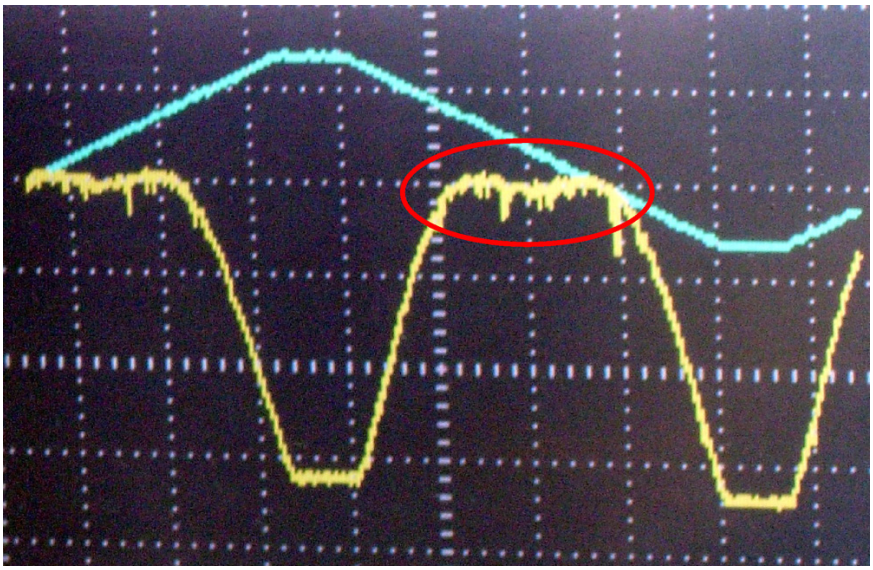

Fig.8. 4 Non-uniform reference intensity across the scanning range for common path setup. Blue line: MEMS-mirror driving voltage; yellow line: reference intensity; red circle: useful scanning range, ~2mm laterally.

Alternatively, reference arm and sample arm are kept separate and a much thicker glass window is employed in the endoscope so that only one reflection interface appears in the field of view. This not only takes full advantage of the large scanning range of MEMS-mirror, but also facilitates to solve the mirror image problem mentioned previously. Additionally, Kasai velocity estimator [20] is employed where the phase difference is achieved with complex signal and only one angle calculation is required. This algorithm significantly improves the contrast, as shown in Fig.8.2C).

8.7 Preliminary experimental results

8.7.1 Flow rate measurement accuracy

To evaluate the performance of the Doppler endoscopic system, preliminary experiment was first conducted on phantoms with intralipid flows. A syringe pump was utilized to control the volumetric flow rate. 0.5% intralipid diluted from stock 20% Intralipid (Fisher Scientific, Inc) was pumped into a

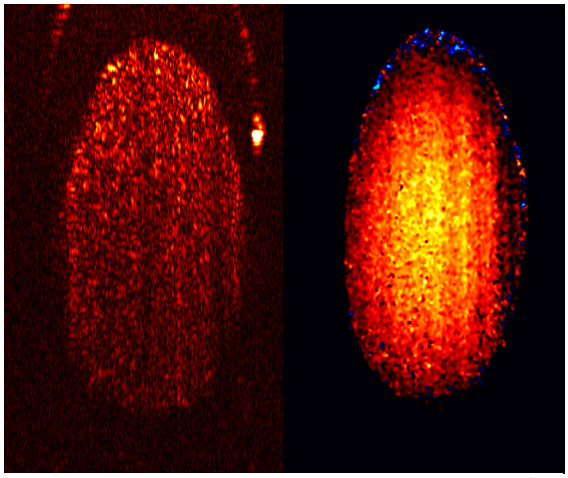

Fig.8. 5 Doppler endoscopic image for intralipid flow within 0.57mm translucent Teflon tubing at 30 μl/min. left panel: structure image; right panel: flow image.

translucent Teflon tubing (ϕ0.57mm I.D.) at flow rates range of 0~50μl/min. The tilting angle of the capillary was 63º with respect to the incident beam, generating flow rate of 0~2.42mm/s. Fig.8.5 shows the images of intralipid flow structure (OCT) and the flow velocity distribution (ODT) at 30 μl/min. Left panel displays the structural OCT image in pseudo-color scale, and right panel maps the flow profile in pseudo-color scale. For the flow inclined to the incident light, the color changes from black to red, yellow and white; otherwise the color changes from dark to blue and cyan. As predicted by Eq.(8.5), the maximum measurable apparent velocity is limited by the ambiguity caused by phase change over π in the phase-resolve algorithm. In our current system, this prevents velocity

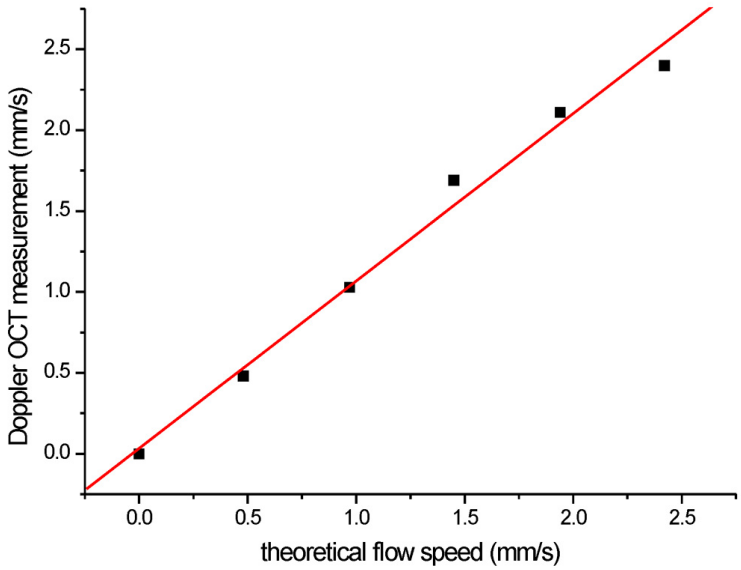

Fig.8. 6 Accuracy of Doppler endoscopic OCT measurement

measurement beyond 2.5mm/s. Potentially, this can be solved using the phase unwrapping algorithm in which phase change in vicinity of π can be determined and corrected.

Totally 6 experimental points were measured at interval of 10 μl/min and used to evaluate the measurement accuracy of Doppler endoscope. Fig.8.6 shows the result of SDOCT measurements of flow rate in the translucent Teflon tubing driven by a precision pump for calibration. The result of least square fit (R=0.994) indicates that the flow rate can be correctly quantified by SDOCT.

8.7.2 Lateral resolution for flow measurement

Sufficient resolution is required to visualize blood vessels within tumors because capillaries can be less than 10 μm in diameter. As discussed previously, the axial and lateral resolution of current system are both ~12μm. Therefore theoretically, the Doppler OCT endoscope has the capability for angiogenesis detection. To evaluate its ability in quantifying flow rate in small vessels, an experiment was performed to measure the 0.5%-Intralipid flow in a capillary with diameter of 155 μm and the result was summarized in Fig.8.7. Panel A) and B) are structure and Doppler flow image respectively. Panel C) is an

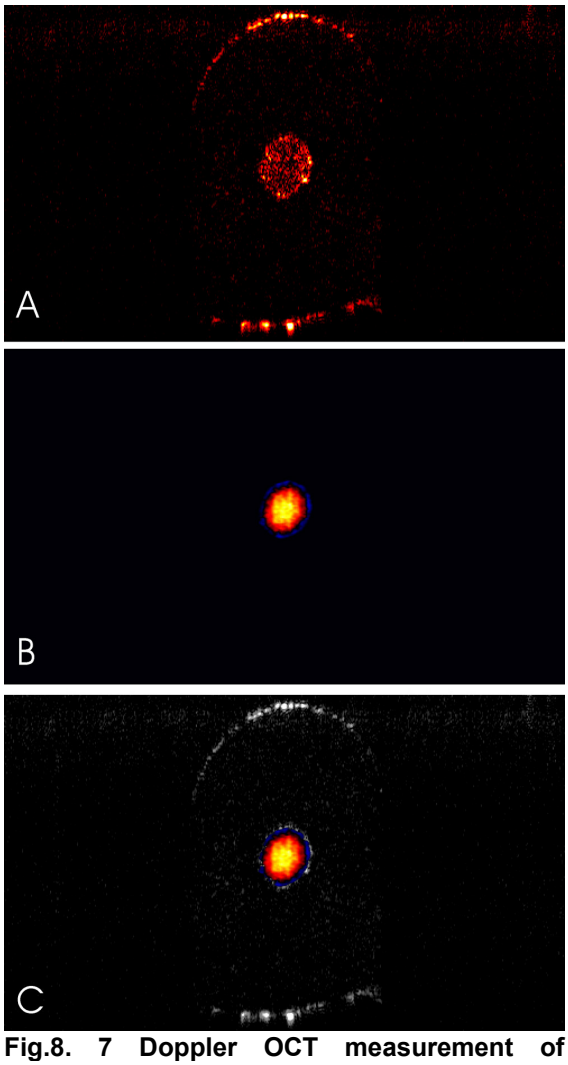

Fig.8. 7 Doppler OCT measurement of intralipid flow at 3μl/min in 155 μm Teflon tube. A) structure image; B) flow image; C) overlapped image. Image size: 2.0 mm laterally and 1.0 mm axially.

overlapped image with gray structure image and color flow image. The flow rate was set at 2 mm/s (3 μl/min), while OCT measured at 1.9 mm/s. This high consistency indicates that the current system can potentially measure blood flow inside tumors in vivo.

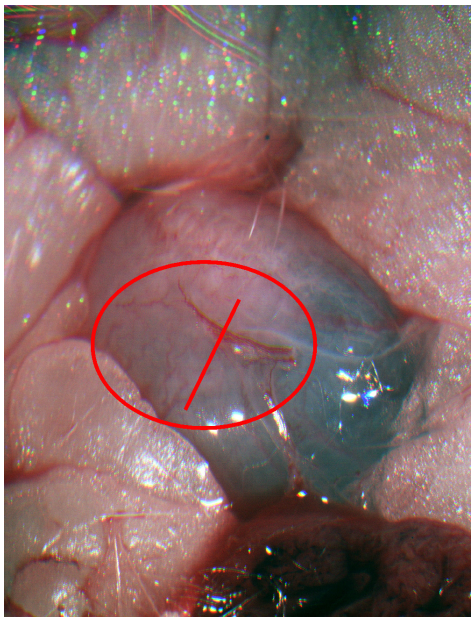

Fig.8. 8 Photograph of the exposed rat bladder. Doppler OCT measurement were performed along the straight line in red circled area. Image size: 2.0 mm × 2.5 mm.

8.8 in vivo animal study (laparoscopic)

Due to the lack of small capillary and precision pump, it is difficult to simulate the in vivo conditions with Telfon tubes. Therefore a rat animal model was employed to further evaluate the performance of the Doppler system where the intact bladder was exposed by opening the abdomen and OCT endoscope was placed against the exterior bladder wall. Measurements were performed primarily in the circled area as shown in Fig.8.8. The OCT images are summarized in Fig.8.9 where the panel A), B) and C) are structure, flow and overlapped image respectively. Since the penetration depth at 1.3 μm is sufficient to visualize the full thickness of the rat bladder which is about 0.25 mm, OCT is able to delineate three basic morphological layers at high resolution: urothelium (U), lamina propria (LP) and muscle layer (M). It is interesting to notice that in structure image A) the urothelium layer is thicker in the circled area. Based on the diagnostic criteria of morphology and enhanced scattering, this could be identified as hyperplasia or

cancer and potentially cause false positive diagnosis. With additional flow information provided by panel B), however, it is obvious that this is a normal bladder with several large blood vessels right below the urothelium and therefore correct diagnosis can be achieved. This implies that the additional Doppler flow measurement is a very promising contrast enhancement technique to improve the diagnostic specificity.

Besides the large blood vessels with apparent blood flow rate of ~6 mm/s, many very small blood vessels are also visualized within 4 mm lateral scanning range. It is also noticed that the smallest one is only about 16 μm (Bv2) in diameter with apparent flow rate of ~2 mm/s. A blood vessel of this size is very difficult to identify based on structure image alone. The enhanced contrast for flow imaging at high resolution indicates that the Doppler OCT endoscope has sufficient sensitivity to visualize angiogenesis inside tumor. And the combination of structure image and Doppler flow measurement can potentially improve both the diagnostic sensitivity and specificity of OCT endoscopy for bladder cancer.

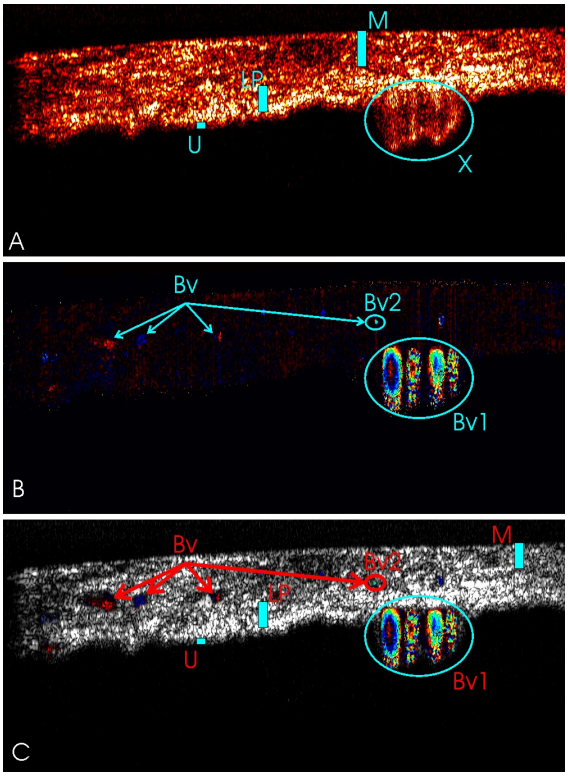

Fig.8. 9 ex vivo flow measurement for a rat bladder. A) structure; B) flow; C) overlapped image. U: urothelium; LP: lamina propria; M: muscle layer; Bv: blood vessel. Image size: 4mm laterally and 0.7mm axially.

8.9 *In vivo* animal study prior to clinical trial

To further evaluate the capability of Doppler OCT system for blood flow measurement *in vivo*, the sample arm was connected to endoscope probe in stead of the benchtop stereoscope and preliminary experiment was performed in the animal study with acute inflammation porcine bladder model as described in Chapter VI. OCT imaging was performed at the 24 to 48 hour time points after intravesical instillation of protamine sulfate dissolved in PBS vehicle. Prior to OCT imaging, the pig was anaesthetized with 5% inhale isoflurane for induction and 1-2.5% for maintenance, then the bladder was imaged by white-light-guided OCT inserted into a standard 22Fr cystoscopic sheath. The entire imaging procedure lasted less than 30 minutes, and then the anesthesia was curtailed and the animal was freed. The animal study followed the protocols approved by the IACUC committee of SUNY at Stony Brook. 2D OCT images were displayed in pseudocolour on a PC monitor for improved visual contrast.

Fig.8.10 shows a 2D endoscopic OCT image of normal porcine bladder with acute irritation, in which the morphological details of the porcine bladder wall (a close human homologue), e.g., urothelium (U),

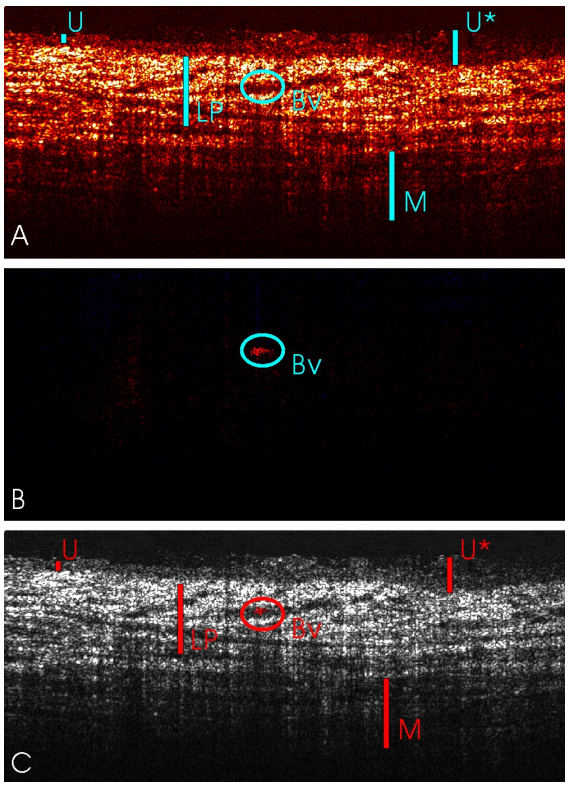

Fig.8. 10 Doppler OCT measurement for porcine bladder in vivo. A): structure; B) flow; C) overlapped image. U: urothelium; U*: thickening urothelium due to acute irritation; LP: lamina propria; M: muscle layer; Bv: blood vessel. Image size: 4mm laterally and

lamina propria (LP), and the muscularis or smooth muscle layers (M) are clearly delineated based on their location and backscattering differences (Panel A): normal urothelium is usually a thin layer with low backscattering, the lamina propria is of high scattering and the muscularis appears lower scattering than LP with large bifurcated interfaces between layers of collagen bundles. Morphological changes pertinent to acute irritation following protamine sulfate instillation can also be detected by OCT, as indicated on the right side of the image.

Panel B) shows the Doppler blood flow image, in which a blood vessel of 144 μm in diameter is identified. The apparent flow rate is estimated to be ~0.65 mm/s. This relatively slow blood flow is partially attributed to the large angle between the incident light beam and the blood vessel. Nevertheless, the flow image helps to differentiate real blood vessels from those 'gap' structures within lamina propria which are related to acute irritation. More importantly, the results of this in vivo study indicate that Doppler OCT endoscopy is practical in clinic scenario.

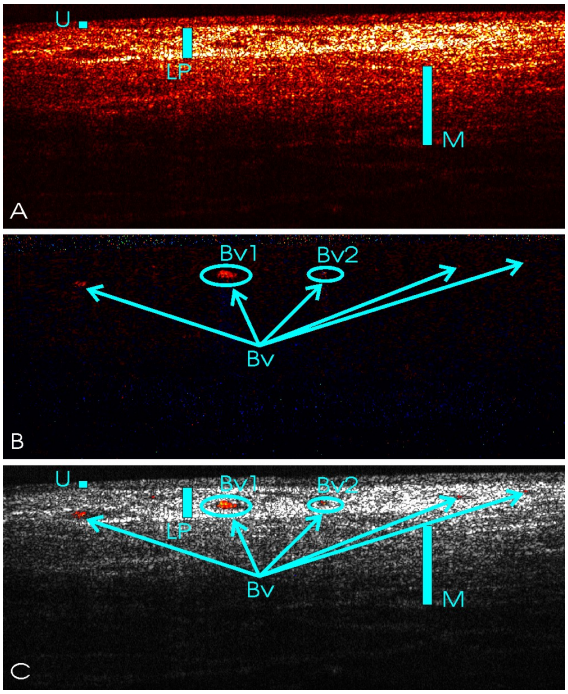

Fig.8. 11 in vivo flow measurement for human in a normal bladder. A): structure; B): flow; C) overlapped image. U: urothelium; LP: lamina propria; M: muscle layer; Bv: blood vessel. Image size: 4mm laterally and 2mm axially.

8.10 in vivo human study

Following successful *in vivo* porcine bladder imaging study, we initiated *in vivo* clinical study on symptomatic patients scheduled for operation-room examinations and treatments such as cystoscopy with possible biopsies, transurethral resection of bladder tumors (TURBT), and cystectomy. As exemplified in Fig.8.11 are the results of a normal human bladder in which panel A) is structure OCT image *in vivo*, panel B) is the Doppler flow image, and panel C) is the overlapped image. The endoscopic OCT is 4mm in the transverse direction and 2mm in the vertical direction. It is obvious to see that human bladder bears a close similarity to porcine bladder in terms of the anatomic architecture and optical properties such as scattering and absorption. The morphological details of normal human bladder were well delineated by OCT, e.g., the low scattering urothelium U, high-scattering lamina propria LP, and the upper muscularis M. Doppler flow image indicated that in normal bladder the blood vessels primarily locate within the lamina propria (LP) layer. The size of the blood vessels ranges from 21 μm to 134 μm with apparent flow rate of 0.5 to 1 mm/s in this case.

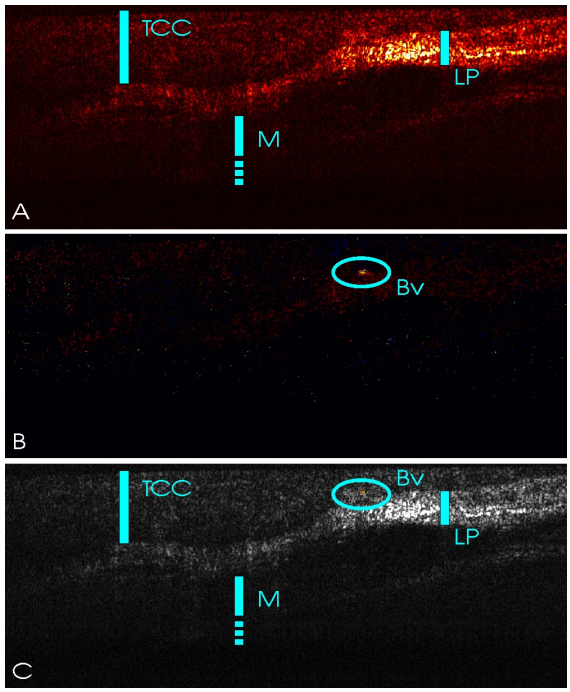

Fig.8. 12 in vivo flow measurement for human bladder cancer. A): structure; B): flow; C) overlapped image. TCC: transitional cell carcinoma; LP: lamina propria; M: muscle layer; Bv: blood vessel. Image size: 4mm laterally and 2mm axially.

In addition to normal bladder, Fig.8.12 shows the results of a bladder

tumor at the transition area. The structure image in panel A) shows low scattering papillary structure. It is interesting to notice that in panel B), a blood vessel of 76 um with apparent flow rate of 0.9 mm/s is in the low scattering lesion, which possibly is fibro vascular cord which usually presents in papillary TCCs. This suggests that Doppler OCT endoscopy is a very promising technique to improve diagnostic specificity. More in vivo studies are undergoing to evaluate the capability of Doppler OCT for diagnostic specificity enhancement in vivo.

8.11 Discussions and conclusions

In summary, the technical improvement of MEMS-based OCT endoscope to enable high-resolution imaging of subsurface blood flows has been presented to provide functional information besides bladder morphology noninvasively, and the preliminary results of *in vivo* clinical diagnosis of transitional cell cancers (TCCs). To examine the utility of endoscopic Doppler OCT for *in vivo* imaging, we initiated *in vivo* clinical study on symptomatic patients scheduled for operation-room examinations. As the cross sectional structure images in Fig.7.6 and Fig.7.7 indicate, structural OCT diagnosis is based on changes of the bladder morphology and scattering intensity to diagnose bladder tumors. Therefore, it can efficiently locate and diagnose highly papillary TCCs as exemplified by Fig.7.7 and high grade cancer with enhanced scattering. With much more complicated situations in human cases, it is not uncommon that OCT structure image alone may fail to distinguish benign bladder lesions (hyperplasia, inflammation) from flat TCCs such as carcinomas *in situ*, both of which may show a thicker urothelium with low scattering. Therefore, additional contrast

mechanisms are needed that will permit more accurate diagnosis, especially flat TCCs. Among several of currently viable contrast enhancement techniques for OCT, Doppler flow imaging offers a great promise to noninvasive detection of angiogenesis induced by carcinogenesis, owing to its high spatial resolution (e.g., <10μm at current stage) and high sensitivity (0.1 mm/s) at imaging depths of 2-3mm. Based on our ex vivo and in vivo studies, the additional flow information allows to visualize the vasculature of the bladder and it can be used for caner diagnosis such as angiogenesis noninvasively, instantaneously, and at ~10um resolution, if implemented endoscopically. Detection of local vascularization with endoscopic Doppler OCT can potentially further improve OCT diagnosis of human TCCs *in vivo.* The initial results of endoscopic Doppler OCT as shown in Fig.8.12 are of great interest for future detection of elevated tumor vasculature. Combined with structure imaging, Doppler OCT endoscopy can further improve diagnostic efficacy and is a very promising technique for bladder cancer diagnosis.

Chapter IX

Conclusions and future work

From 1985-2000, the number of patients diagnosed annually with bladder cancer increased by 33%, and there are 300,000-400,000 patients with bladder cancer each year in the United States[85]. Early diagnosis is crucial for appropriate treatment of bladder cancer, and yet this still remains a clinical challenge. For instance, screening techniques, such as urine cytology and fluorescence in situ hybridization (FISH) test, are highly sensitive screening techniques for the clinical detection of carcinoma in situ (CIS) and high grade transitional cell carcinoma (TCC). These techniques are much less sensitive for early, low grade TCC, however. The value of sensitive cancer screening techniques is compromised without an effective method of locating cancerous lesions non-invasively. Unfortunately conventional imaging methods, such as x-ray, computerized tomography (CT) and magnetic resonance imaging (MRI), fail to detect early bladder malignancies because of limited resolution. Cystoscopy is currently the clinical standard for early cancer detection. As an en face image modality, cystoscopy is not able to resolve in depth direction and often misses flat TCC. Thus, conclusive diagnosis and staging of malignancy in patients with positive cytology relies on random biopsy, which is invasive and may miss almost 50% of early flat TCCs[5, 6].

Optical coherence tomography (OCT) is a fiber optic imaging technique that can provide high resolution cross-sectional images of tissue morphology at a

depth of 2 to 3 mm. Therefore, OCT endoscopy is a novel medical modality with high potential to diagnose early bladder cancer. In recent years, there have been a number of reports on endoscopic OCT techniques; however, the development of a workable high-fidelity endoscopic OCT suitable for *in vivo* clinical imaging diagnosis remains a technical challenge. The MEMS-based OCT endoscope presented in this dissertation is of particular interest to urological applications for the following reasons: 1) the larger beam size allows improved lateral resolution; 2) full-range MEMS laser scanning can achieve a larger image size (e.g., >4.5mm) in the transverse direction; 3) the front-view OCT catheter can be easily incorporated with surface imaging guidance for effective endoscopic OCT examination of bladder surface; and the OCT scope is reliable, sterilizable, and cost effective.

This dissertation describes MEMS-based OCT endoscopy for bladder cancer diagnosis in detail and presents the ex vivo and in vivo studies to evaluate its utility. The preliminary results demonstrate that OCT endoscopy is a very promising technique for bladder cancer diagnosis. It can provide cross-sectional image, clearly delineating micro-morphological structure of the bladder including urothelium, lamina propria and muscular layer. With 2-3 mm penetration depth into bladder, OCT is able to delineate the tumor boundary and to stage bladder cancer in early phases. With technical advances including spectral domain OCT (SDOCT) to enhance imaging speed and dynamic range and Doppler OCT to visualize blood flow within bladder wall, OCT is potentially

capable of detecting abnormal blood vessel formation due to carcinogenesis and thus enhance the diagnosis of bladder cancers.

Future developments that can optimize system performance include

1) Future study to refine the diagnostic criteria based on morphological structure and optical scattering properties due to complex situations in clinical human cases. It has been found that some human TCCs may also show no obvious increase of urothelial backscattering. More detailed human data and analysis are required to study the relation between urothelial backscattering enhancement and cancer grading and staging.

2) Doppler OCT provides additional contrast mechanism for bladder cancer diagnosis. Preliminary results show that Doppler OCT endoscopy is able to identify fibro vascular cord present in papillary TCCs, which can provide more specific criteria for cancer diagnosis. However, it is noticed that the accurate flow rate measurement is susceptible to several factors. For instance, the measured flow rate is inherently dependent on the angle between incident laser beam and the blood vessel. At perpendicular position, no phase change will be detected and therefore diagnostic sensitivity is compromised. In addition, the actual blood flow rate is affected by the pressure when the OCT endoscope is pushed against the bladder wall during clinical study, which can temporally decrease or even stop the blood flow. Possible solutions include modification of the tilting angle of the glass window at the endoscope distal end to avoid perpendicular position. Also, the focal plane of the endoscope can be shifted a little further away so that OCT images can be taken without pushing against the bladder wall.

3) Flexible OCT catheter to be developed in addition to the current rigid one. This modification may allow access to some areas of the bladder such as the bladder neck that current rigid OCT catheter fails.

4) Further technical advances to achieve larger mirrors which allow higher lateral resolution instead of current MEMS-mirror of 1.2 × 1.2 mm. Also, improvement in dynamic scanning range can enlarge the endoscopic field of view and therefore potentially facilitate OCT guidance for surgeries. MEMS-mirrors without flatness distortion, combined with a field flatness correction lens can potentially provide constant reference intensity for common-path spectral domain OCT setup, which will decrease phase noise and improve dynamic range for Doppler OCT measurement.

5) Minimization is possible with customized signal processing chips that enables portable system which can be easily transported and operated. The current OCT imaging system is bulky mainly due to many analog signal processing units, which requires more space in operation room and is not user friendly.

6) Other contrast enhancement mechanism may provide more information for cancer diagnosis besides Doppler OCT measurements. As mentioned previously, current application of OCT for bladder cancer diagnosis is mainly scattering intensity based, with little exploration in other optical properties such as polarization status and spectroscopic features. It will be interesting to study the changes in cancerous lesions versus normal tissue which can possibly further improve diagnostic efficacy.

7) Development of super-high resolution OCT has shown the ability for cellular imaging which can resolve sub-cellular components (e.g. nuclei), while with current light source and optical design, the OCT resolution is ~ 10 μm axially and laterally, which is insufficient to measure nuclei size directly. The endoscopic application of super-high resolution OCT can potentially provide optical biopsy diagnosis in real time.

References

1. *Cancer Facts & Figures 2007*. 2007 [cited 2007 August, 1]; Available from: http://www.cancer.org/downloads/STT/CAFF2007PWSecured.pdf.

2. Cajulis, R.S., G.K. Haines, D. Friashidvegi, K. McVary, and J.W. Bacus, *Cytology, Flow-Cytometry, Image-Analysis, And Interphase Cytogenetics By Fluorescence In-Situ Hybridization In The Diagnosis Of Transitional-Cell Carcinoma In Bladder Washes - A Comparative-Study.* Diagnostic Cytopathology, 1995. **13**(3): p. 214.

3. Sarosdy, M.F., P. Schellhammer, G. Bokinsky, P. Kahn, R. Chao, L. Yore, J. Zadra, D. Burzon, G. Osher, J.A. Bridge, S. Anderson, S.L. Johansson, M. Lieber, M. Soloway, and K. Flom, *Clinical evaluation of a multi-target fluorescent in situ hybridization assay for detection of bladder cancer.* Journal Of Urology, 2002. **168**(5): p. 1950.

4. Leyh, H., M. Marberger, P. Conort, C. Sternberg, V. Pansadoro, F. Pagano, P. Bassi, L. Boccon-Gibod, V. Ravery, U. Treiber, and L. Ishak, *Comparison of the BTA stat (TM) test with voided urine cytology and bladder wash cytology in the diagnosis and monitoring of bladder cancer.* European Urology, 1999. **35**(1): p. 52.

5. Kriegmair, M., R. Baumgartner, R. Knuchel, H. Stepp, F. Hofstadter, and A. Hostetter, *Detection of early bladder cancer by 5-aminolevulinic acid induced porphyrin fluorescence.* Journal Of Urology, 1996. **155**(1): p. 105.

6. Zaak, D., D. Frimberger, H. Stepp, S. Wagner, R. Baumgartner, P. Schneede, M. Siebels, R. Knuchel, M. Kriegmair, and A. Hofstetter, *Quantification of 5-aminolevulinic acid induced fluorescence improves the specificity of bladder cancer detection.* Journal Of Urology, 2001. **166**(5): p. 1665.

7. Kriegmair, M., D. Zaak, R. Knuechel, R. Baumgartner, and A. Hofstetter, *5-aminolevulinic acid-induced fluorescence endoscopy for the detection of lower urinary tract tumors.* Urologia Internationalis, 1999. **63**(1): p. 27.

8. Zaak, D., M. Kriegmair, H. Stepp, H. Stepp, R. Baumgartner, R. Oberneder, P. Schneede, S. Corvin, D. Frimberger, R. Knuchel, and A. Hofstetter, *Endoscopic detection of transitional cell carcinoma with 5-aminolevulinic acid: Results of 1012 fluorescence endoscopies.* Urology, 2001. **57**(4): p. 690.

9. Koenig, F., S. Gonzalez, W.M. White, M. Lein, and M. Rajadhyaksha, *Near-infrared confocal laser scanning microscopy of bladder tissue in vivo.* Urology, 1999. **53**(4): p. 853-7.

10. Tearney, G.J., M.E. Brezinski, J.F. Southern, B.E. Bouma, S.A. Boppart, and J.G. Fujimoto, *Optical biopsy in human urologic tissue using optical coherence tomography.* Journal Of Urology, 1997. **157**(5): p. 1915.

11. Zagaynova, E.V., O.S. Streltsova, N.D. Gladkova, L.B. Snopova, G.V. Gelikonov, F.I. Feldchtein, and A.N. Morozov, *In vivo optical coherence tomography feasibility for bladder disease.* Journal Of Urology, 2002. **167**(3): p. 1492.

12. Xie, T.Q., M.L. Zeidel, and Y.T. Pan, *Detection of tumorigenesis in urinary bladder with optical coherence tomography: optical characterization of morphological changes.* Optics Express, 2002. **10**(24): p. 1431.

13. Pan, Y.T., H.K. Xie, and G.K. Fedder, *Endoscopic optical coherence tomography based on a microelectromechanical mirror.* Optics Letters, 2001. **26**(24): p. 1966.

14. Feldchtein, F.I., G.V. Gelikonov, V.M. Gelikonov, R.V. Kuranov, A.M. Sergeev, N.D. Gladkova, A.V. Shakhov, N.M. Shakhova, L.B. Snopova, A.B. Terent'eva, E.V. Zagainova, Y.P. Chumakov, and I.A. Kuznetzova, *Endoscopic applications of optical coherence tomography.* Optics Express, 1998. **3**(6): p. 257.

15. Wu, J.G., M. Conry, C.H. Gu, F. Wang, Z. Yaqoob, and C.H. Yang, *Paired-angle-rotation scanning optical coherence tomography forward-imaging probe.* Optics Letters, 2006. **31**(9): p. 1265.

16. Xie, T.Q., Z.G. Wang, and Y.T. Pan, *High-speed optical coherence tomography using fiberoptic acousto-optic phase modulation.* Optics Express, 2003. **11**(24): p. 3210.

17. Pan, Y.T., T.Q. Xie, C.W. Du, S. Bastacky, S. Meyers, and M.L. Zeidel, *Enhancing early bladder cancer detection with fluorescence-guided endoscopic optical coherence tomography.* Optics Letters, 2003. **28**(24): p. 2485.

18. Wang, Z.G., Z.J. Yuan, H.Y. Wang, and Y.T. Pan, *Increasing the imaging depth of spectral-domain OCT by using interpixel shift technique.* Optics Express, 2006. **14**(16): p. 7014.

19. Wang, Z.G., D.B. Durand, M. Schoenberg, and Y.T. Pan, *Fluorescence guided optical coherence tomography for the diagnosis of early bladder cancer in a rat model.* Journal Of Urology, 2005. **174**(6): p. 2376.

20. Yang, V.X.D., M.L. Gordon, A. Mok, Y.H. Zhao, Z.P. Chen, R.S.C. Cobbold, B.C. Wilson, and I.A. Vitkin, *Improved phase-resolved optical Doppler tomography using the Kasai velocity estimator and histogram segmentation.* Optics Communications, 2002. **208**(4-6): p. 209-214.

21. Huang, D., E.A. Swanson, C.P. Lin, J.S. Schuman, W.G. Stinson, W. Chang, M.R. Hee, T. Flotte, K. Gregory, C.A. Puliafito, and J.G. Fujimoto, *Optical Coherence Tomography.* Science, 1991. **254**(5035): p. 1178.

22. *Handbook of Optical Coherence Tomography*, ed. B.E. Bouma and G.J. Tearney. 2002: Marcel Dekker, Inc.

23. Pan, Y.T., R. Birngruber, and R. Engelhardt, *Contrast limits of coherence-gated imaging in scattering media.* Applied Optics, 1997. **36**(13): p. 2979.

24. Chen, N.G. and Q. Zhu, *Rotary mirror array for high-speed optical coherence tomography.* Optics Letters, 2002. **27**(8): p. 607.

25. Ballif, J., R. Gianotti, P. Chavanne, R. Walti, and R.P. Salathe, *Rapid and scalable scans at 21 m/s in optical low-coherence reflectometry.* Optics Letters, 1997. **22**(11): p. 757.

26. Tearney, G.J., B.E. Bouma, and J.G. Fujimoto, *High-speed phase- and group-delay scanning with a grating-based phase control delay line.* Optics Letters, 1997. **22**(23): p. 1811.

27. Hausler, G. and W.M. Lindner, *'Coherence Radar' and 'Spectral Radar'--New Tools for Dermatological Diagnosis.* Journal Of Biomedical Optics, 1998. **3**(1): p. 21-31.

28. , M.G.I. *Gaussian Beam Optics*. 2002 [cited 2006; Available from: http://www.mellesgriot.com/products/optics/gb_2.htm.

29. Pan, Y.T., R. Birngruber, J. Rosperich, and R. Engelhardt, *Low-Coherence Optical Tomography In Turbid Tissue - Theoretical-Analysis.* Applied Optics, 1995. **34**(28): p. 6564.

30. Kwong, K.F., D. Yankelevich, K.C. Chu, J.P. Heritage, and A. Dienes, *400-Hz Mechanical Scanning Optical Delay-Line.* Optics Letters, 1993. **18**(7): p. 558.

31. Fetterman, M.R., J.C. Davis, H.S. Tan, W. Yang, D. Goswami, J.K. Rhee, and W.S. Warren, *Fast-frequency-hopping modulation and detection demonstration.* Journal Of The Optical Society Of America B-Optical Physics, 2001. **18**(9): p. 1372.

32. Hitzenberger, C.K., P. Trost, P.W. Lo, and Q.Y. Zhou, *Three-dimensional imaging of the human retina by high-speed optical coherence tomography.* Optics Express, 2003. **11**(21): p. 2753.

33. Xie, T.Q., Z.G. Wang, and Y.T. Pan, *Dispersion compensation in high-speed optical coherence tomography by acousto-optic modulation.* Applied Optics, 2005. **44**(20): p. 4272.

34. Zhao, Y.H., Z.P. Chen, C. Saxer, S.H. Xiang, J.F. de Boer, and J.S. Nelson, *Phase-resolved optical coherence tomography and optical Doppler tomography for imaging blood flow in human skin with fast scanning speed and high velocity sensitivity.* Optics Letters, 2000. **25**(2): p. 114.

35. Leitgeb, R.A., L. Schmetterer, C.K. Hitzenberger, A.F. Fercher, F. Berisha, M. Wojtkowski, and T. Bajraszewski, *Real-time measurement of in vitro flow by Fourier-domain color Doppler optical coherence tomography.* Optics Letters, 2004. **29**(2): p. 171.

36. Rollins, A.M., M.D. Kulkarni, S. Yazdanfar, R. Ung-arunyawee, and J.A. Izatt, *In vivo video rate optical coherence tomography.* Optics Express, 1998. **3**(6): p. 219.

37. Smith, E.D.J., A.V. Zvyagin, and D.D. Sampson, *Real-time dispersion compensation in scanning interferometry.* Optics Letters, 2002. **27**(22): p. 1998.

38. Treacy, E.B., *Optical Pulse Compression With Diffraction Gratings.* Ieee Journal Of Quantum Electronics, 1969. **QE 5**(9): p. 454.

39. Leitgeb, R., C.K. Hitzenberger, and A.F. Fercher, *Performance of fourier domain vs. time domain optical coherence tomography.* Optics Express, 2003. **11**(8): p. 889.

40. de Boer, J.F., B. Cense, B.H. Park, M.C. Pierce, G.J. Tearney, and B.E. Bouma, *Improved signal-to-noise ratio in spectral-domain compared with time-domain optical coherence tomography.* Optics Letters, 2003. **28**(21): p. 2067.

41. Wojtkowski, M., V. Srinivasan, J.G. Fujimoto, T. Ko, J.S. Schuman, A. Kowalczyk, and J.S. Duker, *Three-dimensional retinal imaging with high-speed ultrahigh-resolution optical coherence tomography.* Ophthalmology, 2005. **112**(10): p. 1734.

42. Oh, W.Y., S.H. Yun, G.J. Tearney, and B.E. Bouma, *115 kHz tuning repetition rate ultrahigh-speed wavelength-swept semiconductor laser.* Optics Letters, 2005. **30**(23): p. 3159.

43. Yasuno, Y., V.D. Madjarova, S. Makita, M. Akiba, A. Morosawa, C. Chong, T. Sakai, K.P. Chan, M. Itoh, and T. Yatagai, *Three-dimensional and high-speed swept-source optical coherence tomography for in vivo investigation of human anterior eye segments.* Optics Express, 2005. **13**(26): p. 10652.

44. Huber, R., M. Wojtkowski, and J.G. Fujimoto, *Fourier Domain Mode Locking (FDML): A new laser operating regime and applications for optical coherence tomography.* Optics Express, 2006. **14**(8): p. 3225.

45. Leitgeb, R.A., C.K. Hitzenberger, A.F. Fercher, and T. Bajraszewski, *Phase-shifting algorithm to achieve high-speed long-depth-range probing by frequency-domain optical coherence tomography.* Optics Letters, 2003. **28**(22): p. 2201.

46. Choma, M.A., C.H. Yang, and J.A. Izatt, *Instantaneous quadrature low-coherence interferometry with 3 x 3 fiber-optic couplers.* Optics Letters, 2003. **28**(22): p. 2162.

47. Zhang, J., J.S. Nelson, and Z.P. Chen, *Removal of a mirror image and enhancement of the signal-to-noise ratio in Fourier-domain optical coherence tomography using an electro-optic phase modulator.* Optics Letters, 2005. **30**(2): p. 147.

48. Davis, A.M., M.A. Choma, and J.A. Izatt, *Heterodyne swept-source optical coherence tomography for complete complex conjugate ambiguity removal.* Journal Of Biomedical Optics, 2005. **10**(6).

49. Vakoc, B.J., S.H. Yun, J.F. de Boer, G.J. Tearney, and B.E. Bouma, *Phase-resolved optical frequency domain imaging.* Optics Express, 2005. **13**(14): p. 5483.

50. Leitgeb, R.A., W. Drexler, A. Unterhuber, B. Hermann, T. Bajraszewski, T. Le, A. Stingl, and A.F. Fercher, *Ultrahigh resolution Fourier domain optical coherence tomography.* Optics Express, 2004. **12**(10): p. 2156.

51. Cense, B. and N.A. Nassif, *Ultrahigh-resolution high-speed retinal imaging using spectral-domain optical coherence tomography.* Optics Express, 2004. **12**(11): p. 2435.

52. Zhang, J., W.G. Jung, J.S. Nelson, and Z.P. Chen, *Full range polarization-sensitive Fourier domain optical coherence tomography.* Optics Express, 2004. **12**(24): p. 6033.

53. Park, B.H., M.C. Pierce, B. Cense, S.H. Yun, M. Mujat, G.J. Tearney, B.E. Bouma, and J.F. de Boer, *Real-time fiber-based multi-functional spectral-domain optical coherence tomography at 1.3 mu m.* Optics Express, 2005. **13**(11): p. 3931.

54. Sarunic, M.V., B.E. Applegate, and J.A. Izatt, *Spectral domain second-harmonic optical coherence tomography.* Optics Letters, 2005. **30**(18): p. 2391.

55. Yasuno, Y., S. Makita, T. Endo, M. Itoh, T. Yatagai, M. Takahashi, C. Katada, and M. Mutoh, *Polarization-sensitive complex Fourier domain optical coherence*

tomography for Jones matrix imaging of biological samples. Applied Physics Letters, 2004. **85**(15): p. 3023-3025.

56. Wang, Z.G., H. Adler, D. Chan, A. Jain, H.K. Xie, Z.L. Wu, and Y.T. Pan, *Cystoscopic optical coherence tomography for urinary bladder imaging in vivo.* Proceedings of SPIE: Coherence Domain Optical Methods and Optical Coherence Tomography in Biomedicine X, 2006. **6079**: p. 91.

57. Dorrer, C., N. Belabas, J.P. Likforman, and M. Joffre, *Spectral resolution and sampling issues in Fourier-transform spectral interferometry.* Journal Of The Optical Society Of America B-Optical Physics, 2000. **17**(10): p. 1795.

58. Oppenheim, A.V. and R.W. Schafer, *Discrete-Time Signal Processing*. Prentice Hall Signal Processing, ed. A.V. Oppenheim. 1989: Prentice Hall.

59. Yun, S.H., G.J. Tearney, B.E. Bouma, B.H. Park, and J.F. de Boer, *High-speed spectral-domain optical coherence tomography at 1.3 mu m wavelength.* Optics Express, 2003. **11**(26): p. 3598.

60. Wojtkowski, M., R. Leitgeb, A. Kowalczyk, T. Bajraszewski, and A.F. Fercher, *In vivo human retinal imaging by Fourier domain optical coherence tomography.* Journal Of Biomedical Optics, 2002. **7**(3): p. 457.

61. Pan, Y.T., J.P. Lavelle, S.I. Bastacky, S. Meyers, G. Pirtskhalaishvili, M.L. Zeidel, and D.L. Farkas, *Detection of tumorigenesis in rat bladders with optical coherence tomography.* Medical Physics, 2001. **28**(12): p. 2432.

62. Pan, Y., H. Xie, and G. Fedder, *Endoscopic optical coherence tomography based on a microelectromechanical mirror.* OPTICS LETTERS, 2001. **26**(24): p. 1966-1968.

63. Steinberg, G.D., C.B. Brendler, R.A. Squire, and J.T. Isaacs, *Experimental intravesical therapy for superficial transitional cell carcinoma in a rat bladder tumor model.* J Urol, 1991. **145**(3): p. 647-53.

64. Hicks, R.M. and J.S. Wakefield, *Rapid induction of bladder cancer in rats with N-methyl-N-nitrosourea. I. Histology.* Chem Biol Interact, 1972. **5**(2): p. 139-52.

65. Chang, S.C., A.J. MacRobert, and S.G. Bown, *Biodistribution of protoporphyrin IX in rat urinary bladder after intravesical instillation of 5-aminolevulinic acid.* Journal Of Urology, 1996. **155**(5): p. 1744-1748.

66. Fujimoto, J.G., S.A. Boppart, G.J. Tearney, B.E. Bouma, C. Pitris, and M.E. Brezinski, *High resolution in vivo intra-arterial imaging with optical coherence tomography.* Heart, 1999. **82**(2): p. 128.

67. Bouma, B.E., G.J. Tearney, C.C. Compton, and N.S. Nishioka, *High-resolution imaging of the human esophagus and stomach in vivo using optical coherence tomography.* Gastrointestinal Endoscopy, 2000. **51**(4): p. 467.

68. Li, X.D., S.A. Boppart, J. Van Dam, H. Mashimo, M. Mutinga, W. Drexler, M. Klein, C. Pitris, M.L. Krinsky, M.E. Brezinski, and J.G. Fujimoto, *Optical coherence tomography: Advanced technology for the endoscopic imaging of Barrett's esophagus.* Endoscopy, 2000. **32**(12): p. 921.

69. Xie, H.K., Y.T. Pan, and G.K. Fedder, *A CMOS-MEMS mirror with curled-hinge comb drives.* Journal Of Microelectromechanical Systems, 2003. **12**(4): p. 450.

70. Wang, Z.G., H. Adler, D. Chan, A. Jain, H.K. Xie, Z.L. Wu, and Y.T. Pan. *Cystoscopic optical coherence tomography for urinary bladder imaging in vivo*. in *Proceedings of SPIE: Coherence Domain Optical Methods and Optical Coherence Tomography in Biomedicine X*. 2006. San Jose, California, USA.

71. Leitgeb, R.A., L. Schmetterer, W. Drexler, A.F. Fercher, R.J. Zawadzki, and T. Bajraszewski, *Real-time assessment of retinal blood flow with ultrafast acquisition by color Doppler Fourier domain optical coherence tomography.* Optics Express, 2003. **11**(23): p. 3116.

72. Yasuno, Y., T. Endo, S. Makita, G. Aoki, M. Itoh, and T. Yatagai, *Three-dimensional line-field Fourier domain optical coherence tomography for in vivo dermatological investigation.* Journal Of Biomedical Optics, 2006. **11**(1).

73. Wang, Z., C.S.D. Lee, W.C. Waltzer, J. Liu, H. Xie, Z. Yuan, and Y. Pan, *in vivo Bladder Imaging with MEMS-based Endoscopic Spectral Domain Optical Coherence Tomography.* Journal of Biomedical Optics, 2007. **12**: p. 034009.

74. Goddard, J.C., C.D. Sutton, P.N. Furness, K.J. O'Byrne, and R.C. Kockelbergh, *Microvessel density at presentation predicts subsequent muscle invasion in superficial bladder cancer.* Clin Cancer Res, 2003. **9**(7): p. 2583-6.

75. Richard, D.E., E. Berra, and J. Pouyssegur, *Angiogenesis: how a tumor adapts to hypoxia.* Biochem Biophys Res Commun, 1999. **266**(3): p. 718-22.

76. Saxer, C.E., J.F. de Boer, B.H. Park, Y.H. Zhao, Z.P. Chen, and J.S. Nelson, *High-speed fiber-based polarization-sensitive optical coherence tomography of in vivo human skin.* Optics Letters, 2000. **25**(18): p. 1355.

77. Wang, Z., Z. Yuan, H. Wang, and Y. Pan, *Increasing the imaging depth of spectral-domain OCT by using interpixel shift technique.* Optics Express, 2006. **14**(16): p. 7014.

78. Flamm, J. and S. Dona, *The Significance Of Bladder Quadrant Biopsies In Patients With Primary Superficial Bladder-Carcinoma.* European Urology, 1989. **16**(2): p. 81.

79. Messing, E.M. and W. Catalona, *Urothelial tumors of the urinary tract*. 7th ed. Campbell's Urology, ed. P.C. Walsh, et al. 1998: Saunders. 2327-2410.

80. Tumlinson, A.R., J.K. Barton, B. Povazay, H. Sattman, A. Unterhuber, R.A. Leitgeb, and W. Drexler, *Endoscope-tip interferometer for ultrahigh resolution frequency domain optical coherence tomography in mouse colon.* Optics Express, 2006. **14**(5): p. 1878.

81. Sharma, U., N.M. Fried, and J.U. Kang, *All-fiber common-path optical coherence tomography: Sensitivity optimization and system analysis.* Ieee Journal Of Selected Topics In Quantum Electronics, 2005. **11**(4): p. 799.

82. Chen, Z.P., T.E. Milner, D. Dave, and J.S. Nelson, *Optical Doppler tomographic imaging of fluid flow velocity in highly scattering media.* Optics Letters, 1997. **22**(1): p. 64.

83. Izatt, J.A., M.D. Kulkami, S. Yazdanfar, J.K. Barton, and A.J. Welch, *In vivo bidirectional color Doppler flow imaging of picoliter blood volumes using optical coherence tomograghy.* Optics Letters, 1997. **22**(18): p. 1439.

84. Fercher, A.F., W. Drexler, C.K. Hitzenberger, and T. Lasser, *Optical coherence tomography - principles and applications.* Reports On Progress In Physics, 2003. **66**(2): p. 239.

85. Steinberg, G.D. *Bladder Cancer*. 2005 August 08, 2007 [cited; Available from: http://www.emedicine.com/med/topic2344.htm.